Laser-Matter Interactions at Extreme Irradiance: X-ray Generation and Relativistic Channelling

Sjögren, Anders

2002

Laser-Matter Interactions at Extreme Irradiance

X-ray Generation and Relativistic Channelling

2002

Lund Institute of Technology
Lund University

Cover: A split light channel caused by relativistic channelling, imaged by collecting Thomson-scattered light.

Doctoral Thesis
Atomic Physics Division
Department of Physics
Lund Institute of Technology
P.O. Box 118
SE–221 00 Lund
Sweden

Lund Reports on Atomic Physics, ISSN 0281–2162
LRAP–288

ISBN 91-628-5449-6
Printed by KFS i Lund AB

To my wife, Helen,
and our Star from Heaven

Abstract

This thesis summarizes experimental work in which the powerful Ti:sapphire lasers at the High Power Laser Facility at the Lund Laser Centre have been employed to investigate laser-produced X-rays and relativistic channelling. These lasers produce short pulses, of the order of 50 fs, with energies ranging from 1 mJ to 1 J. Thus, the peak powers reach several terawatts and with the most powerful laser system the peak irradiance exceeds 10^{19} W/cm^2. Furthermore, X-rays generated at a synchrotron radiation facility have been used in conjunction with a short-pulse laser to study temporal oscillations on a picosecond timescale in a crystalline material.

In the continuation of a research project, pursued at the High Power Laser Facility since 1992, X-ray generation up to several hundred keV has been investigated by focusing the laser pulses onto solid metal targets. One of the motivations for these experiments is the potential use of laser-produced X-rays in medical radiography.

In another experiment the temporal features of X-rays of a few keV was investigated. In this case, the X-rays were generated by focusing laser pulses into clustered argon gas jets.

Various detection techniques have been used to measure the X-ray spectrum in the different experiments, including energy-resolved photon counting with a charge-coupled device (CCD) and X-ray diffraction on crystals in combination with a CCD. Germanium detectors have also been employed in order to investigate the X-ray spectrum above a few keV more accurately.

The laser-produced X-rays show extraordinary properties compared for example with those generated by the common X-ray tube. Very short pulse duration and a small source size are two important factors that differentiate the laser-based X-ray source from others. In particular, when focusing onto solid targets, a compact, high-repetition-rate laser system has been employed to evaluate the use of laser-produced X-rays (above 10 keV) in diagnostic medicine by recording radiographs using image plates.

Since 1999, a research project at the High Power Laser Facility concentrates on a new field of research: Relativistic channelling.

This involves meticulous control over the laser system that has been constructed to this end and also, comparing with other laser systems in Northern Europe, unprecedented levels of laser irradiance. For the first time in this part of Europe, relativistic channelling has been achieved by focusing laser pulses in a gas jet. The plasmas generated by the laser pulses have been diagnosed through Raman- and Thomson-scattering of the laser pulse. The extension of the generated relativistic channels has been measured and their dependence on laser pulse parameters and plasma density has been investigated. A typical channel length is 0.5 mm, and in such a channel, electrons are accelerated to several MeV, implying extreme accelerating electric fields, thousand times stronger than the maximum field strengths achieved in today's conventional accelerators. The number and energy of the electrons that are accelerated in the relativistic channels have been measured.

This thesis presents more than the experimental work described above. The various laser-matter interactions encountered in the experiments are also discussed from a theoretical point of view. In particular, theory on laser-plasma interactions is introduced to allow better understanding of the experimental work.

Contents

List of Papers

Paper I: **Evaluation of Laser-Irradiated Ar Clusters as a Source for Time-Resolved X-Ray Studies**.
J. Larsson and A. Sjögren.
Rev. Sci. Instrum. **70**, pp. 2253-2256, 1999

Paper II: **Coronary Angiography Using Laser Plasma Sources: X-Ray Source Efficiency and Optimization of a Bent Crystal Monochromator**.
E. Andersson, G. Hölzer, E. Förster, M. Grätz, L. Kiernan, A. Sjögren and S. Svanberg.
J. Appl. Phys. **90**, pp. 3048-3056, 2001.

Paper III: **Influence of Laser Pulse Duration on Relativistic Channels**.
C. Delfin, V. Lokhnygin, J. Mauritsson, A. Sjögren, C.-G. Wahlström, A. Pukhov and G. D. Tsakiris.
Phys. Plasmas **9**, pp. 937-940, 2001.

Paper IV: **Relativistic Channel Formation for Different Laser Pulse Durations**.
A. Sjögren, J. Mauritsson, C. Delfin, V. Lokhnygin, C.-G. Wahlström, A. Pukhov and G. D. Tsakiris.
Second International Conference on Superstrong fields in plasmas. American Institute of Physics Conference Proceedings **611**, pp. 119-125, 2002.

Paper V: **High-Repetition-Rate, Hard X-Ray Radiation from a Laser-Produced Plasma: Photon Yield and Application Considerations**.
A. Sjögren, M. Harbst, C.-G. Wahlström, S. Svanberg and C. Olsson.
Submitted to *Rev. Sci. Instrum.* October, 2002.

Paper VI: **Picosecond X-Ray Diffraction Studies of Laser-Excited Acoustic Phonons in InSb**.
J. Larsson, A. Allen, P. H. Bucksbaum, R. W. Falcone, A. Lindenberg, G. Naylor, T. Missala, D. A. Reis, K. Scheidt, A. Sjögren, P. Sondhauss, M. Wulff and J. S. Wark.
Appl. Phys. A **75**, pp. 467-478, 2002.

Part I

Chapter 1

Introduction

This thesis is centred around the physics that can be investigated using high-power lasers that produce very short pulses ($\lesssim$ 100 fs) in the terawatt regime. In the first part of this thesis these lasers and their use as a tool to manipulate the matter in which the light is propagated are presented. The fundamental physics of light propagation and interaction with matter are also introduced. This physics forms the basis of the second part of the thesis, which deals with experimental research performed at the High Power Laser Facility at the Lund Laser Centre. The lasers that have been employed in this work are presented, as they are of central significance to the thesis. In order to put the lasers at the Lund High Power Laser Facility into a perspective, a short view of the present status of high power lasers in general is given.

Please note that throughout this thesis the International System of Units (SI) is used, unless otherwise is explicitly stated.

The chapter on X-ray generation deals with the part of the research that has dealt with X-ray generation with lasers and X-ray applications; for example, structural changes in matter that occur on the picosecond timescale have been measured. Considering the amount of energy necessary to create an X-ray photon in relation to the photon energy of a laser, it is easy to imagine the complexity of the process. The X-rays are generally produced as a secondary effect in the interaction of light with matter; the primary being that electrons are ripped from their equilibrium states in atoms or molecules and accelerated in the laser fields. These fast electrons subsequently decelerate and X-rays are emitted, i.e. Bremsstrahlung.

The direct interaction between electrons and light forms the basis of the next type of experiment described in this thesis, i.e. the investigation of relativistic self-focusing and channelling of laser light. When the light interacts with ionized matter, the physics approaches plasma physics. A major part of this research has been concerned with reconsidering and transferring existing knowledge from the plasma physics community to the laser physics commu-

nity. Much of the plasma physics known today is related to plasmas in equilibrium; far removed from the almost instantaneous interactions that we encounter when subjecting matter to the extreme irradiance produced by very short laser pulses.

1.1 Background

The interaction between light and matter has been the subject of study for centuries. In the nineteenth century, spectroscopic studies of the emission and absorption of light led to many important discoveries and brought science rapidly forward. However, at that time scientists were not manipulating matter with light; rather, investigating matter, probing it with light and observing the change in the light, or observing the light emitted from different materials. The scientists of that period did not have light sources of the magnitude of a laser, but they had the cunning of fine mechanics and could, for example, construct fine gratings. In 1895 K. Röntgen discovered X-ray radiation and used it to record radiographs, but he neither understood the danger of exposing living organisms to the radiation nor that X-ray radiation is of the same kind of radiation as the light from the sun; *electromagnetic radiation*. During the first decades of the twentieth century, the dual nature of electromagnetic radiation, was established (Fig. 1.1).

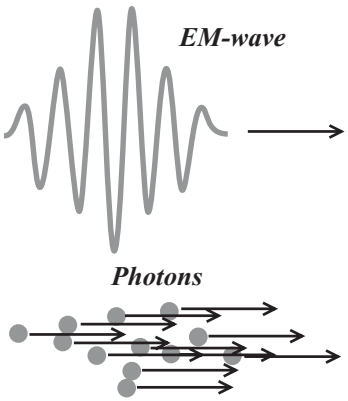

Figure 1.1. *Particle-wave dualism; a light wave can also be modelled as a group of photons.*

When the laser was invented in 1960 with the help of Einstein's theory of stimulated emission, it facilitated new fields of research and was quickly applied in all kinds of existing research. The new light source was powerful beyond what had only recently been considered possible, because the "strength" of a laser is measured neither by its use of electrical power nor by the amount of light it emits. Rather, it is the quality of the laser light that differs from that emitted from any other ordinary light source, such as a candle or a light bulb. Laser light is *coherent* making, for example, 1 W of laser light appear much brighter to the eye than 1 W from a light bulb. Coherent light can be focused to a very small spot by means of a lens or a curved mirror. The theoretical limit is of the order of the wavelength of the light, in contrast to incoherent sources the focus of which is limited by the light-emitting area. Furthermore, a laser normally emits monochromatic or nearly monochromatic light and the wavelengths originate from one or several optical transitions in an atom, ion or molecule structure.

1.1.1 Pulsed Lasers

Rather than distributing the energy continuously over time as a continuous wave (CW) laser does, the energy can be contained in short pulses. This increases the pulse peak power and peak irradiance, i.e. the magnitude of the electric and magnetic fields

increases. A use of pulses is to freeze events. Similar to the way in which a a stroboscope "freezes" motion, the laser pulse can "flash" an object and probe the conditions at that instant. With the higher peak irradiances provided by pulsed lasers it also becomes possible to ionize atoms and molecules through multiphoton processes and to observe nonlinear behaviour of laser-matter interactions. Examples of nonlinearities are self-phase modulation (SPM), sum-frequency generation and low-order harmonic generation. These nonlinearities are observed in the interaction between non-ionized matter and light with an irradiance in the range from 10^9 W/cm^2 to 10^{12} W/cm^2.

In the development of pulsed lasers, not only *shorter* pulses have been achieved, but schemes have also been devised to *amplify* the pulse energy. A series of inventions enabled tremendous development towards shorter pulses and higher peak power. The most important advances are shown in Figure 1.2. As the peak power

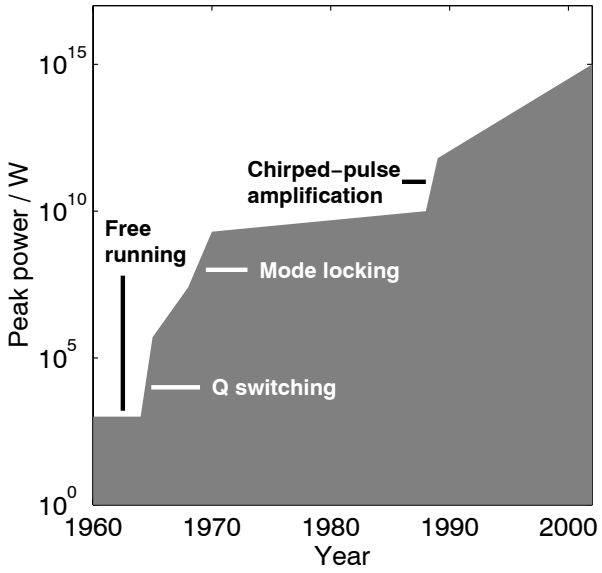

Figure 1.2. *The peak power of pulsed lasers has increased by 12 orders of magnitude over the last 40 years. Several new techniques have been successively introduced, making this rapid development possible.*

approached gigawatt magnitude, the main technical problem was damage to laser optics by the very intense radiation. The solution first employed was to enlarge the diameter of the laser beam, thus reducing the peak irradiance. This had the drawback that laser systems quickly became huge in size. An example of this was the Nova laser at Lawrence Livermore National Laboratories (LLNL), USA. It was inaugurated in 1984, produced tens of kilojoules in total in as many as ten beams each with a 74 cm diameter and

Figure 1.3. *The Nova laser in the USA was the largest laser system in the world before it was dismantled in 1999.*

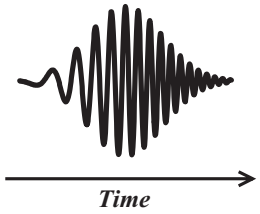

Figure 1.4. *A chirped laser pulse.*

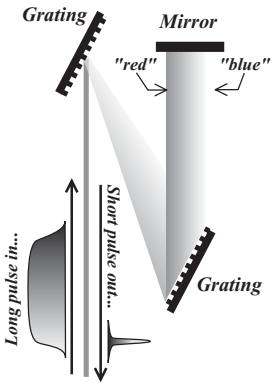

Figure 1.5. *Illustration of a typical laser pulse "compressor" that compresses the pulses in CPA laser systems.*

a total beam cross-section of over one metre (Fig. 1.3). Only a few laser pulses could be produced per day. Such a laser was very costly and could only be used by a few scientists. The design of more compact laser systems was thus of top priority, as a growing scientific community needed intense laser pulses in their research; thus new techniques were needed.

1.1.2 The Chirped-Pulse Amplification (CPA) Technique

The problem was solved by the chirped-pulse amplification (CPA) technique, which most high-power laser systems are based on today. The CPA technique exploits the fact that short pulses necessarily have a relatively broad spectrum; a fact as fundamental as Heisenberg's uncertainty relation. The mathematical approach to describing the relation between the spectrum and the pulse duration is the Fourier transform; when a set of waves with different wavelengths and phases, forming a finitely broad spectrum, are superimposed they may form a pulse (Table 1.1). This stands

Table 1.1. *The minimum spectral width for a few different laser pulse durations. The laser pulse central wavelength is 0.8 μm.*

Pulse duration	Spectral width
1 ps	$\sim$ 1 nm
100 fs	$\sim$ 10 nm
50 fs	$\sim$ 20 nm

in contrast to a perfectly monochromatic wave which can never become anything else but infinite in time. One way decreasing the irradiance inside the laser system is to prolong the pulse before amplifying it and to compress it afterwards. This is exactly what the CPA technique does. The laser pulse is *chirped*, typically in a grating *stretcher*, amplified and then compressed in a grating *compressor*. Chirp is the term used to describe birdsong with varying pitch, and chirping a laser pulse means that the frequencies are placed in a row after each other, i.e. "pitching" the light, as illustrated in Figure. 1.4. The key element is the grating (although other devices can be used) on which the laser pulse diffracts. Using mirrors, and often a second grating, as illustrated in Figure 1.5, different frequency components of the pulse travel different distances, changing their relative phase (delay). Loosely speaking, the colours of the laser pulse are distributed in time, making red come before blue during the amplification of the light. Apart from the induced chirp described, many other processes may influence the chirp of a laser pulse. Simply propagating an ultrashort pulse in air will, in almost all cases, chirp the pulse and therefore prolong it, because air, as all other materials, exhibits a

wavelength-dependent refractive index. Such effects are discussed in Section 2. After amplification the beam is expanded in diameter and re-compressed in a compressor, i.e., exactly the opposite of the stretcher. Figure 1.6 illustrates a typical CPA scheme.

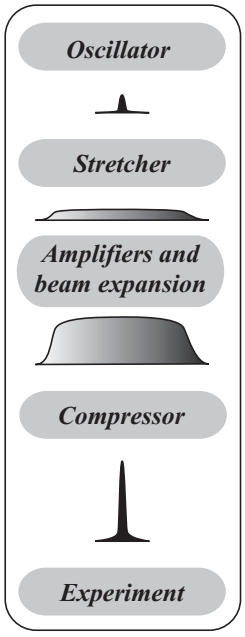

Figure 1.6. *Schematic representation of the CPA technique.*

1.1.3 Ti:sapphire Crystals

The effort to make shorter pulses also involves developing new materials that have wide fluorescence spectra which can be used to amplify the broad spectrum which is characteristic of short pulses. Today, most laser materials for high-power lasers consist of doped crystals; a kind of material that generally features very broad fluorescence spectra because the dopant atoms exhibit different electron energy levels depending on their position in the crystal lattice and thus emit light (fluoresce) at different wavelengths. The most common crystals are titanium-doped sapphire (Ti:sapphire), LiCAF, LiSAF and alexandrite, among others.[1,2] By far the most commonly used crystal is Ti:sapphire; the material on which many of today's state-of-the art lasers are based. The Ti:sapphire crystal absorbs effectively around 0.5 μm and the fluorescence is peaked at 0.8 μm, but it stretches from roughly 0.6 μm to 1 μm, supporting pulses as short as a few femtoseconds. Ti:sapphire lasers are typically used in combination with the CPA technique because of their very short pulse duration. The first commercial high-power Ti:sapphire laser with a ten-hertz repetition rate and $\sim$ 100 fs pulse duration was installed in Lund at the High Power Laser Facility in 1992. Today, the facility has two Ti:sapphire-based laser systems using the CPA technique. These are described in the next part of this chapter.

1.1.4 A Ti:sapphire-based Laser System using CPA

The High Power Facility at the Lund Laser Centre operates a ten-hertz repetition rate multi-terawatt Ti:sapphire laser incorporating a number of units. The first unit is the Ti:sapphire *oscillator*, which generates short and spectrally broad pulses with only a few nanojoules of energy per pulse. These are stretched in time and amplified in a series of Ti:sapphire amplifiers. The crystal *amplifiers* are pumped with light that they can effectively absorb using special, green *pump lasers* (frequency-doubled Nd:YAG lasers). Directly after the pump pulses come the stretched laser pulses, which are amplified in the crystal through stimulated emission. The beam diameter is expanded several times through the laser system, to keep the irradiance below the damage threshold for the optics. The final pulses, 5 cm in diameter, are compressed in time making them very intense and by focusing the pulses to a few micrometres in diameter, extraordinarily high irradiance is achieved.

Extreme Irradiance

The amazing irradiance that can be produced is well over 10^{19} W/cm^2. The peak electric field of such a laser pulse is twenty times stronger than the strong field binding the electron to the nucleus in the ground state of hydrogen (but still less than a thousandth of the field binding the K-shell electrons in tantalum). The physics available for investigations at these high levels of irradiance extends earlier research in spectroscopy, in which matter was subjected to irradiance levels much lower than the corresponding binding energies of the electrons. With this laser, it is easy to observe extreme nonlinear behaviour in light-matter interactions and, moreover, it is easy to ionize the matter and generate a plasma. Furthermore, ionized electrons in very strong laser fields ($> 10^{18}$ W/cm^2) move according to the theory of special relativity, i.e., the effective mass of the electrons increases. Irradiance levels above 10^{18} W/cm^2 causing relativistic electron motion are referred to as *relativistic irradiances* (or *relativistic intensities*). Physics with relativistic irradiances is generally more complicated and often shows new aspects of light-matter interactions successfully described at lower irradiance levels. See Section 2.2 and Chapter 4.

The word intensity is still widely used rather than the more correct term irradiance; both representing the quantity of light power per unit area.

An Unwanted Characteristic Feature

With the extreme irradiance levels that are available with the Lund lasers it becomes important to ensure good *laser pulse contrast*, meaning that unwanted emission of laser light before, and less importantly after, the pulse is minimized. The amplifier crystals emit some light through spontaneous emission before the energy is extracted by the seed laser pulse, i.e. the laser pulse to be amplified. This emission can be amplified and cause high levels of *amplified spontaneous emission* (ASE). The ASE radiation can reach energy levels as high as the laser pulse itself, although of much longer duration, and, since it comes before the main pulse, it can negatively affect the experiment; pre-ionization of the material into which the laser pulse is focused is not uncommon. Similarly, so called *pre-pulses* can be emitted by the laser before the main pulse. These usually originate from a regenerative-type amplifier (Section 1.2). Due to the design of this amplifier the pre-pulses are emitted with about 10 ns temporal spacing. Since the unwanted radiation passes through all subsequent amplifiers before the main pulse, the amplification is great and the radiation can easily affect the experiment (Fig. 1.7). The contrast measured as the energy level of the pre-pulses and the ASE relative to the main laser pulse is usually at least 10^3, but considering that ionization can take place at an irradiance as low as 10^{12} W/cm^2, it is easy to imagine the magnitude of the problem when the laser pulse is focused to $> 10^{19}$ W/cm^2. The problem of reducing the energy in the pre-

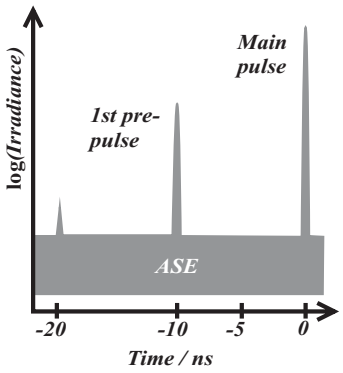

Figure 1.7. *Illustration of the typical output from a Ti:sapphire laser with a regenerative amplifier.*

pulses and ASE is of major concern to the laser physics community now that laser irradiance can reach unprecedented levels.

Laser Diagnostics

As the research situation stands today, the Ti:sapphire lasers at the Lund High Power Facility are becoming increasingly user friendly, enabling complex experiments that require extensive control over the laser system. Knowledge of the pulse shape, temporally and spatially, the spectral shape and the chirp as well as of the status of pre-pulses and ASE is useful if not crucial in many experiments today. However, performing the measurements necessary to gain this knowledge is an art in itself. Temporal pulse-shape measurement tools have been developed from the autocorrelator, through FROG:s (frequency-resolved optical gating) and the XPM (cross-phase modulation) method. Presently, the SPIDER (spectral interferometry for direct electric-field reconstruction) tool is being used at most high-power laser facilities. The latter three measure the temporal and spectral shape as well as the chirp through clever interferometry and the use of nonlinear phenomena. Efforts are currently being made by the European Research Network SHARP to enhance the laser pulse contrast. This, however, requires the development of autocorrelators and spectrometers with very high dynamic range. Such spectrometers are required as the outer edges of the spectrum determine, to some extent, the pulse contrast on a femtosecond timescale. Even with a perfectly shaped focusing mirror, the focus size can deviate from the diffraction limit because of imperfect phase and irradiance distributions over the pulse cross-section. These imperfections arise in the amplifying crystals and in the stretcher/compressor arrangement in CPA lasers and require careful attention.

1.2 The Lund High Power Laser Facility

The work presented in this thesis was with one exception, performed at the High Power Laser Facility at the Lund Laser Centre. The exception, presented in Section 3.4, is the experimental investigation, described in Paper VI, of phonon excitation in indium antimonide (InSb) crystals, which was carried out in Grenoble, France at the European Synchrotron Radiation Facility (ESRF). The Lund High Power Laser Facility incorporates two Ti:sapphire terawatt lasers, a ten-hertz and a kilohertz repetition rate system, which have been continuously upgraded and improved since their respective inaugurations. The progress in terms of peak power is shown in Figure 1.8. The ten-hertz laser produces pulses simultaneously in two "arms". The original arm produces 2 TW and the relatively new multi-terawatt arm presently produces as much as 40 TW, placing it among the top peak-performance ten-hertz

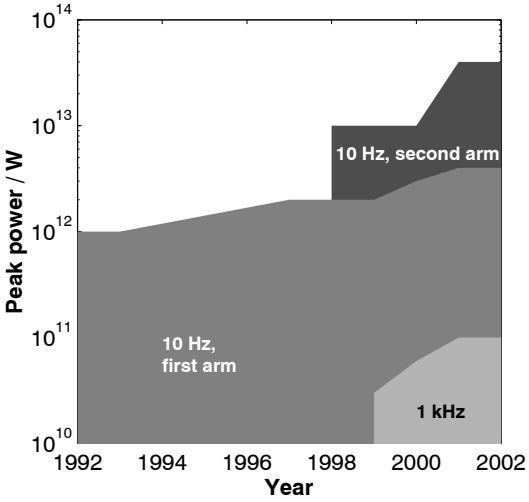

Figure 1.8. *A peak power roadmap of the Lund laser systems, from their respective inaugurations up till now. In 1998, the 10 Hz laser was redesigned to support an additional multi-terawatt "arm" for extra-demanding experiments.*

lasers in the world. This new multi-terawatt arm was used in two of the three X-ray experiments described in this thesis in Section 3.2 (Paper II) and Section 3.3 (Paper I), and in the experiments on relativistic self-focusing, discussed in Chapter 4 (Papers III and IV). The kilohertz laser was used in the final X-ray generation experiment described in Section 3.2 (Paper V).

Today's state-of-the art laser systems worldwide, including the multi-terawatt laser at the High Power Laser Facility in Lund, are listed in an OECD report from 2001,[3] which includes many different kinds of lasers (Table 1.2). The Ti:sapphire laser with its

Table 1.2. *A few of the state-of-the art laser systems in the world today. The information was taken from an OECD report on compact, high-intensity short-pulse lasers from 2001.*[3]

Facility	Location	Material	Peak Power / TW	Pulse Duration / fs	Repetition Rate / Hz
LLNL	USA	Ti:sap.	200	75	~ 0.0017
MBI	Germany	Ti:sap.	100	50	~ 0.0017
LULI	France	Nd:glass	100	300	~ 0.0008
JAERI	Japan	Ti:sap.	100	20	10
LOA	France	Ti:sap.	100	25	10
LLC/Lund	Sweden	Ti:sap.	20	35	10
RAL	UK	Ti:sap.	10	50	10
MPQ	Germany	Ti:sap.	8	130	10
Celia	France	Ti:sap.	1	20	1000

ability to produce short pulses at a high repetition rate is the best in all respects except for pulse energy. Glass laser systems produce longer pulses but with similar peak powers to their Ti:sapphire

Table 1.3. *Technical data for the first arm of the ten-hertz laser which, apart from serving its own experiments also produces the seeding pulses for the multi-terawatt arm. The Dazzler^{TM}is a phase-modulating device used to add chirp in a controlled way. It is discussed briefly in Section 4.4.*

Oscillator output	4 nJ at 80 MHz
Dazzler throughput	$\sim 50\%$
Stretcher throughput	10%
Regen output	~ 5 mJ at 10 Hz
Butterfly output	0.25 J
Seed split-off	0.05 J
Compressor throughput	65%
Final pulse energy	0.1 J at 10 Hz
Beam diameter	4 cm
Pulse duration	35 fs
Spectral bandwidth	~ 45 nm

siblings because of the larger amount of energy in these pulses.

1.2.1 The Ten-Hertz Laser System

This laser system was inaugurated in 1992, and had at that time a stretcher with a lens arrangement* and a single butterfly amplifier, producing 0.15 ps pulses with 0.15 J of energy, i.e. ~ 1 TW. Since then, almost all the components of the original equipment have been replaced or upgraded in order to improve the performance due to the increasing demands for high-quality laser pulses in various experiments (Fig. 1.8). Presently, the laser system produces pulses in two arms that are used simultaneously in separate experiments. The first arm, resembling the original laser system (Table 1.3) serves one experimental set-up with 2 TW pulses. A fraction of the laser pulses is split off to the second, multi-terawatt arm, which is employed in most of the experiments presented in this thesis (Table 1.4). The irradiance in the new arm is close to the damage threshold for the optics and it is therefore very important to seed the new butterfly amplifier with high-quality pulses. The quality of the pulses in the multi-terawatt arm is governed to a large extent by the quality of the original laser system, which means that it is crucial to maintain a high standard all the way from the heart of the laser, i.e. the oscillator, through all the units to the final output after the compressor. The complete laser system and its main units are illustrated in Figure 1.9.
The seed beam for the multi-terawatt arm is spatially filtered and thereafter expanded to ~ 16 mm in diameter, before entering a four-pass butterfly amplifier, Figure 1.10, which is pumped by as much as 50 W of green light from five Nd:YAG lasers. The to-

*Today, stretchers are made of reflective optics in order to minimize phase errors.

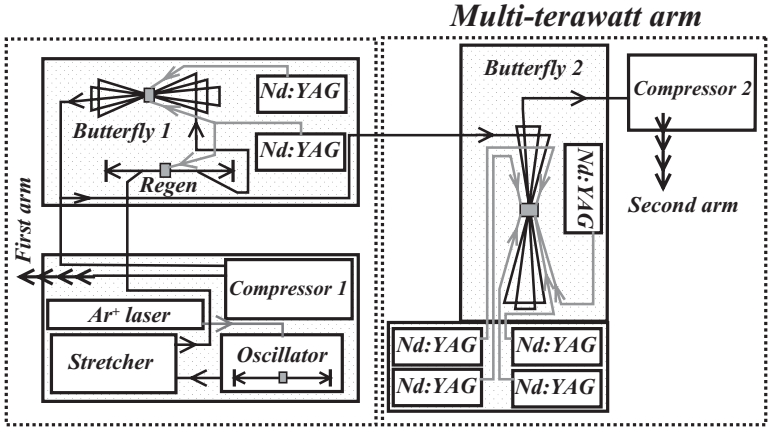

Figure 1.9. *Schematic illustration of the ten-hertz laser layout. The main units of the laser system are indicated, in particular the several Ti:sapphire crystals, which are shaded grey.*

Table 1.4. *Technical data for the multi-terawatt arm of the ten-hertz laser.*

Spatial filter throughput	$\gtrsim 90\%$
Butterfly output	2 J
Compressor throughput	70%
Final pulse energy	1 J at 10 Hz
Beam diameter	6 cm
Pulse duration	35 fs
Spectral bandwidth	~ 45 nm

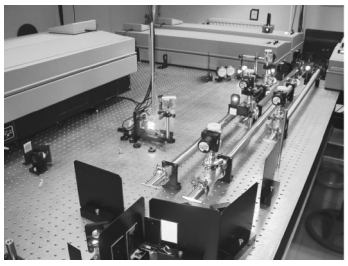

Figure 1.10. *The four-pass butterfly amplifier in the multi-terawatt arm of the ten-hertz laser system.*

tal pump fluence is 2 J/cm^2 and the seed pulse energy is roughly 50 mJ. The Ti:sapphire crystal is 20 mm thick and its dopant concentration is about $4 \cdot 10^{18}$ cm^{-3}.The Nd:YAG beams pump the crystal symmetrically, and great care has been directed in order to minimize the angle of incidence on the Ti:sapphire crystal, particularly for the seed beam. The crystal is cooled by Peltier elements to room temperature, and these in turn are cooled by circulating water from a reservoir. Cooling is regulated to prevent condensation of water vapour on the crystal. The crystal is of high quality and can amplify the seed pulse very evenly over the spatial profile of the pulse. The crystal thermal lens, also discussed in Section 1.2.2, is not as strong as in the kilohertz laser, but since the output power of the laser is changed mainly by altering the relative delay between the pump pulses and the seed pulse, the lens-effect can affect the pulse. It is therefore planned to cool the crystal to about 120 K (in vacuum) in order to increase the heat conductivity and thus remove the influence of the thermal lens. Finally, after amplification, the laser beam is expanded to about

6 cm in diameter and enters the evacuated compressor chamber, see Figure 1.11, through an antireflection-coated fused-silica window. The horizontally polarized laser pulse is compressed and the short pulse is transported to the experiment through an evacuated tubing system. When focusing the laser pulses using a focal length of 15 cm, the peak irradiance reaches well over 10^{19} W/cm^2. Such a high irradiance is essential to carry the interaction of the laser pulse and matter to the so-called relativistic regime.

Through the whole laser system, a large number of video cameras and irises serve as alignment tools. These have been found to be essential for continuous operation of the laser system. The laser beam passes through the variable irises and the light that scatters off them is monitored by the cameras. Video monitors are mounted on the walls in the laser lab, allowing instant checks of the whole laser alignment.

However, aligning the compressor is a much more difficult task and very small errors can profoundly change (deteriorate) the appearance of the laser focus, for example.[4] Inside the compressor chamber are two gratings, a retro-reflector, a wedge and an output coupler (Fig. 1.12). The wedge can be moved into the beam to reflect about one percent of the light, through a high-quality window, to a small optical table with diagnostic equipment outside the evacuated chamber. On the optical table are placed a second-order autocorrelator, a spectrometer and an 11.5 m focal length lens that focuses the pulse onto a CCD chip. Thus, the spectrum, the temporal distribution and the focus can be monitored simultaneously. Broadly speaking, the compressor is then aligned by iteratively optimizing the pulse duration and the focal spot size/appearance.

The multi-terawatt arm thus produces very powerful pulses at the rather high repetition rate of 10 Hz, which is very useful for experiments that require large quantities of data. However, one problem with the compressor is that the gold gratings gradually become "dirty". In particular, the last reflection, when the pulse is short, leaves a blackened mode-like mark on the grating. Some metallic mirrors in the experimental set-up also show similar marks. The reason is believed to be that the laser pulse ionizes hydrocarbon molecules which stick to the surface because the mean free path is rather long at these low pressures ($\sim 10^{-6}$ mbar). Since the gratings are very expensive and because replacing them requires time-consuming realignment, the problem must be solved in some way. One way of preventing the process is to fill the compressor with, for example, argon in order to shorten the mean free path without affecting the laser pulse very much. This has the drawback that the compressor chamber must be physically separated from the rest of the experimental set-up, for example by placing a window between the compressor and the experimental chamber. A different solution would be to clean the grating with the help

Figure 1.11. *The evacuated compressor chamber kept at 10^{-6} mbar. The beam goes through the compressor and through the evacuated tubing to the experiment.*

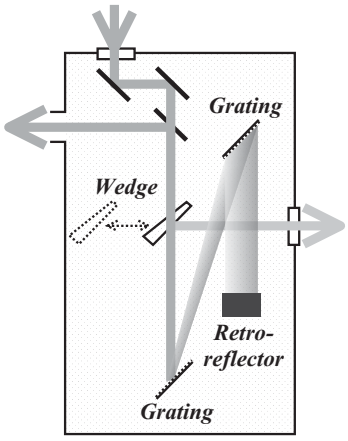

Figure 1.12. *Schematic illustration of the evacuated compressor chamber. The beam goes through the compressor to the retroreflector, which lowers the height of the beam.*

of an oxygen-plasma device.[5] This can be done without removing the gratings from their aligned positions.

The regenerative amplifier generates some pre-pulses and ASE (cf. Fig. 1.7), but because the Ti:sapphire crystal in the multi-terawatt arm is pumped by as much as 5 J, ASE becomes a serious problem even in this butterfly amplifier. When pumping the crystal that much, reflections from the crystal surfaces can be sufficient to couple light back into the crystal and initiate a strong de-excitation process before the seed pulse arrives. In order to prevent this, the seed pulse should be amplified immediately after the crystal has been excited by the pump lasers. However, the delay between the pump and seed pulses is varied as a means of changing the amplification gain, and there is then a risk that the ASE will have time to grow. Furthermore, it has been noted that the spatial mode of the amplified seed pulse changes as the delay between the pump and seed pulses is varied (on a 10 ns timescale). The reason may be that the ASE level varies in the crystal, perhaps due to slightly varying surface reflectivities, leaving the crystal with a varying gain distribution. Four of the six crystal surfaces will therefore be coated with a special, refractive index matching substance which effectively absorbs the spontaneous emission.

1.2.2 The Kilohertz Laser System

The Lund High Power Laser Facility operates another Ti:sapphire laser, inaugurated in 1999, with a repetition rate of 1 kHz, i.e. one-hundred times higher than the other Ti:sapphire laser. The average power and the pulse duration are similar, but the laser generates pulses of a only few millijoules. The kilohertz laser is ideal for experiments that require less than 10^{17} W/cm^2, and is mostly used in high-harmonic-generation experiments. However, as discussed in Chapter 3 and in Paper V, hard X-rays have been generated by focusing the pulses from this laser system onto a solid target.

The spectrum of the laser oscillator is extraordinarily wide and can support very short laser pulses. The laser system also includes a stretcher, a regenerative (regen) amplifier and two butterfly amplifiers, see Figure 1.13. After beam expansion, the pulses are compressed in a grating compressor (Table 1.5). The pump lasers for the amplifiers are two 20 W frequency-doubled Nd:YLF lasers. The light from one of them is split into two beams; one going to the regenerative amplifier and the other to the first butterfly amplifier. The second Nd:YLF pumps the second butterfly amplifier. This second, home-built butterfly amplifier was added after installation and the laser system now produces up to 3 mJ per pulse.

The kilohertz laser emits some unwanted ASE from the amplifiers and some pre-pulses from the regenerative amplifier (cf. Fig. 1.7). Most of the kilohertz laser's ASE radiation originates

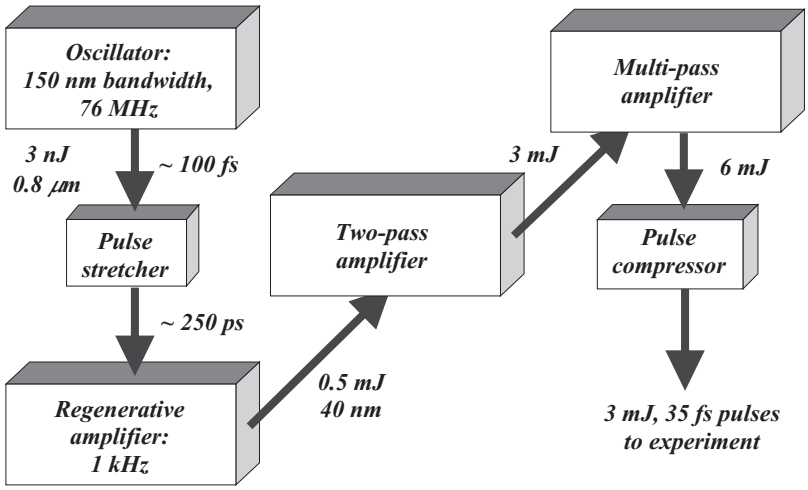

Figure 1.13. *Schematic illustration of the kilohertz repetition rate laser system at the High Power Laser Facility in Lund.*

Table 1.5. *The kilohertz laser in Lund in technical terms.*

Oscillator output	3 nJ at 76 MHz
Stretcher throughput	20%
Regen output	0.4 mJ at 1 kHz
First two-pass amplifier output	2 mJ
Second two-pass amplifier output	6 mJ
Compressor throughput	50%
Final pulse energy	3 mJ at 1 kHz
Beam diameter	2 cm
Pulse duration	30 fs
Spectral bandwidth	50 nm

from the regenerative amplifier because the gain is high and the cavity enhances the self-amplification. The timing of the the Nd:-YLF pump pulses and the drivers for the Pockel's cells are very important because they largely control the strength of the ASE and the pre-pulses.

The laser is equipped with diagnostic devices that monitor the various parameters. The regenerative amplifier is monitored with a photodiode and a fast oscilloscope that shows the growth of the pulses being amplified. A spectrometer measures the pulse spectrum at any desired position in the laser system; usually before the last butterfly amplifier. The remaining diagnostic equipment is available after the compressor; a second-order autocorrelator, another spectrometer and a device that measures the pre-pulse contrast. Two fast photodiodes provide a temporal resolution that allows estimation of the contrast at least 3 ns before the main pulse. One of the diodes monitors the main pulse and controls the trig-

ger of the oscilloscope, and the other one measures the pre-pulse level. The use of two photodiodes increases the available dynamic range, therefore allowing more accurate contrast measurements. The spatial mode of the laser is very sensitive to the conditions in the last amplifier; the volume in the crystal that is pumped works as an aperture that generates an Airy-like mode after amplification. However, a magnifying telescope is mounted directly after the amplifier and before the compressor which effectively images this pump aperture far away. As a result of this the Airy mode does not grow in diameter as would otherwise be expected. The spatial mode quality is assessed via visual inspection on fluorescent paper and on Kodak Linagraph direct-print paper which produces a burn mark of the mode. A mobile CCD camera is sometimes used for detailed quantitative mode analysis by focusing the pulses onto the CCD, through a series of neutral-density filters.

Chapter 2

Interaction of High-Power Laser-Pulses with Matter

In this chapter the theory that forms the foundation for Chapters 3 and 4 is presented. Starting with the propagation of laser pulses, basic concepts such as phase velocity and group velocity are introduced and focusing and scattering of laser light are briefly discussed. Although basic, this material is of central importance to later parts of this thesis. The second part of this chapter introduces the fundamental physics of the subjects of this thesis, namely interactions between a laser pulse and a plasma.

2.1 The Physics of Pulse Propagation

Propagation of a Monochromatic Wave

Consider a monochromatic light wave traversing a material. It is very convenient to use the *refractive index* as a measure of how fast the wave travels. This is defined as the ratio of the speed of light in vacuum, c, and in the material, v_p,

$$v_p = \frac{c}{n}. \tag{2.1}$$

The *phase velocity*, v_p, can alternatively be expressed as,

$$v_p = \frac{\omega}{k}, \tag{2.2}$$

where $\omega = 2\pi f$ is the light *angular frequency*, $k = \frac{2\pi}{\lambda}$ the *wave number* or *propagation constant* and $\lambda = \lambda_0/n$ is the wavelength in the material, normally shorter than the wavelength in vacuum, λ_0. The phase velocity is the velocity of a particular point, or *phase*, of the wave.

The reasoning that explains why a light wave slows down in most materials helps to explain some of the physics in this thesis. Every material exhibits some sort of resonance at specific light frequencies. If subject to light, the electrons in the material will want to oscillate with the light wave, but generally the oscillation will lag behind or forestall the the light wave. In order to understand this, recollect that the phase of a forced oscillation, relative to the driving force, depends on the difference in frequency of the driving oscillation and the material resonance frequency, i.e. $\Delta f = f_{resonance} - f_{driving}$. Consider a light wave that traverses a material, one thin slice at a time, and...

1. ...forces the electrons in the material to oscillate together with the wave...
2. ...the moving charges emit light at the same frequency as the driving light wave...
3. ...the induced light is not perfectly in phase with the driving wave...
4. ...superposition of the induced and the driving light produces a phase-shifted wave...
5. ...the resulting wave enters the next slice of material, now becoming the driving light wave, and the reasoning starts again from 1...

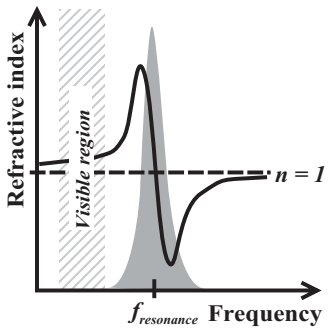

Figure 2.1. *The refractive index as a function of the driving frequency in a typical material such as air or glass where the important resonance frequencies lie in the ultraviolet part of the spectrum. Only one resonance frequency is shown. The material absorption, indicated by the grey peak, is large close to the resonance frequency.*

The resulting wave will therefore propagate with a phase velocity, v_p, different from the vacuum velocity, c. The refractive index is directly coupled to the phase difference, which in turn depends on Δf, and it can be concluded that the refractive index is a function of the driving frequency. Figure 2.1 illustrates the refractive index behaviour in a typical material such as air or glass. Close to its resonance frequency, the material starts to absorb, indicated by the grey peak in the figure.

Propagation of a Laser Pulse

The temporal envelope of an electromagnetic pulse can take many forms, but in theory it is often modelled as a gaussian shape. The mathematical expression describing the electric field of a chirped laser pulse, gaussian-shaped in time and space assuming cylindrical

symmetry can be written as:

$$E(t,r) = E_0 \underbrace{\exp\left[-2\ln 2\left(\frac{t}{\tau}\right)^2\right]}_{\text{the temporal shape...}} \cdot \underbrace{\exp\left[-\left(\frac{r}{R}\right)^2\right]}_{\text{...the beam cross-section...}} \cdot \underbrace{\exp\left(i\omega t + i\Psi(t)\right) + \text{c.c.}}_{\text{...the carrier wave and its chirp.}} \cdot \tag{2.3}$$

The introduced parameters are the full-width at half maximum (FWHM) pulse duration, τ, and the $(1/e^2)$ cross-section radius, R in the expression for irradiance, $I(t,r) = \frac{1}{2}c\varepsilon_0|E(t,r)|^2$. The time-dependent phase, i.e. the chirp, is expressed by $\Psi(t)$.

The radius of the cross-section of a beam is often denoted by ω in the literature, but this can lead to confusion since ω is also used to denote angular frequency.

A light pulse propagates with a *group velocity*,[6]

$$v_g = \frac{d\omega}{dk} = \left(\frac{n}{c} + \frac{2\pi}{\lambda_0}\frac{dn}{d\omega}\right)^{-1}, \tag{2.4}$$

which is the velocity in a material of the *envelope* of the laser pulse. This group velocity is different from the phase velocity derived above and depends on the *slope* of the refractive index, $dn/d\omega$.

What does it mean that the group and phase velocity differ? Consider a laser pulse with wavelength 0.8 μm propagating through air. The electric and magnetic fields, which oscillate beneath the pulse profile move faster than the pulse, as illustrated in Figure 2.2.

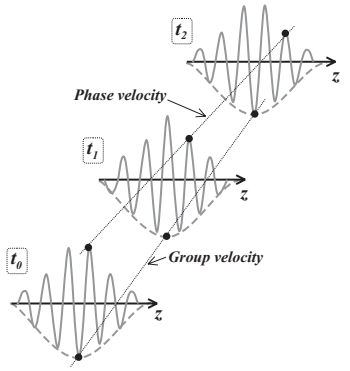

Figure 2.2. *A laser pulse propagating along z at times t_0, t_1 and t_2, illustrating a case where the phase velocity is greater than the group velocity.*

Most materials also exhibit a *group velocity dispersion* (GVD), causing a laser pulse to change its pulse shape and chirp while propagating. Normally, this effect is unwanted because it distorts the pulse. However, GVD can also be used to compress already chirped pulses.

A central interaction phenomenon which, unlike dispersion, depends on the irradiance is *self phase modulation* (SPM).[6] Whereas the dispersion merely changes the phases of the different frequencies in the spectrum, SPM modifies the spectrum completely, generating new frequencies and attenuating some of the frequencies present. The underlying reason for SPM is that the refractive index changes with irradiance which, in turn, depends on the spatial and temporal coordinate, $I(x,y,z,t)$ (cf. (2.3)):

$$n(I) = n_0 + n_I\, I. \tag{2.5}$$

A pulse subjected to SPM acquires a temporal phase, or delay, at every point that depends on the local irradiance. This reshapes

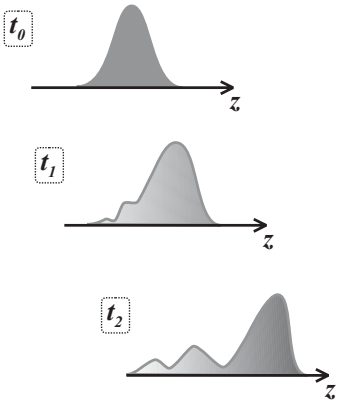

Figure 2.3. *A laser pulse propagating along z at times t_0, t_1 and t_2, illustrating an example of SPM and GVD acting together.*

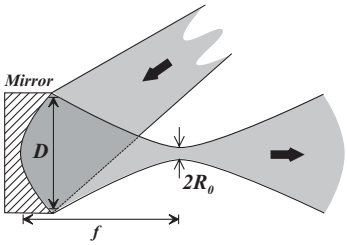

Figure 2.4. *A mirror with a focal length f focuses a beam with diameter $D = \pi R$ (99% energy) to a focal spot with radius r_0 $(1/e^2)$.*

the pulse and changes the spectrum, and together with GVD, may force the pulse to break up or it may broaden the spectrum while enhancing the chirp. An example of SPM and GVD working together to change the pulse shape is shown in Figure 2.3.

2.1.1 Focusing of Laser Light

In almost all experiments the laser pulse is focused in order to increase the irradiance. When dealing with short laser pulses, curved mirrors are preferred to lenses, because the latter may affect the pulse through several nonlinear processes and dispersion. The mirrors used in the course of the work described in this thesis are off-axis parabolic mirrors. These are much more difficult to align than lenses. In general, using focusing optics with a focal length f with an initial, unfocused beam radius of R $(1/e^2)$ (cf. (2.3)), the smallest focus radius is,[6]

$$R_0 \simeq \frac{f}{\pi R}\lambda, \tag{2.6}$$

where λ is the laser wavelength and πR is the diameter of the beam containing 99% of the energy (Fig. 2.4). The confocal parameter represents the extension of the laser focus along the axis of propagation, measured as the distance between the two points where the beam cross sectional area is twice the minimum,[6]

$$\text{confocal parameter} \simeq 2\pi\frac{R_0^2}{\lambda} = 2\pi\left(\frac{f}{\pi R}\right)^2\lambda. \tag{2.7}$$

For example, taking the parameters used in the relativistic channelling experiment (Chapter 4) the diameter of the laser beam, as measured using a sheet of fluorescent paper inserted in the beam, is $\pi R \sim 6$ cm and the focal length of the focusing mirror is 15 cm giving a smallest diameter of only 4 μm and a corresponding confocal parameter of ~ 30 μm. In the X-ray generation experiments (Chapter 3) much shorter focal lengths are used, corresponding to $f/\pi R = 1$. In these experiments the optimal focus diameter approaches the diffraction limit at ~ 1 μm and the confocal parameter is only ~ 5 μm.

2.1.2 Scattering of Laser Light

Throughout this thesis, numerous laser light scattering phenomena are discussed. Therefore, a short general introduction to the scattering of *coherent* light will be given here. Light with a large degree of *incoherence* scatters differently from coherent light because for such light the interference of scattered wavelets can never be coherent.

As soon as laser light propagates through a material, be it a gas or solid consisting of atoms or molecules, or a plasma of free electrons and ions, light is scattered. The discussion on the refractive index above, is an example of light scattering where the scattered light interferes constructively, i.e. coherently, in the same direction of travel as the beam. However, the laser beam is also scattered sideways through the same process, which is called *Rayleigh scattering*. The coherent, driving light induces small shifts between positive and negative charge centres, i.e. a dipole, leading to an oscillatory motion, and the acceleration of the charges causes light to scatter; coherently in the forward direction and incoherently sideways. Rayleigh scattering always occurs when the light propagates in a medium of scattering centres, i.e. molecules or atoms, which are much smaller than the wavelength of the light. For example, this kind of scattering causes the sky to be blue, because the efficiency of the process is proportional to $1/\lambda^4$, i.e. the blue sunlight (incoherent) scatters more than the red. A particular example of Rayleigh scattering can be found in Paper I, where scattering occurs in a clustered argon gas and the size of the clusters can be deduced through measurements of the irradiance of the scattered light. Most materials can be pictured as small scattering centres with resonance frequencies in the ultraviolet region of the spectrum. Thus, the driving frequency of a Ti:sapphire laser is much lower than the resonance frequency, and the dipoles therefore oscillate almost *in phase* with the driving frequency. In a typical low-density plasma, the opposite is true. The driving frequency of the Ti:sapphire laser is much higher than the resonance frequency and the laser causes the *free* electrons to oscillate (and the ions, but with a much smaller amplitude) *out of phase*.

If the material shows some kind of symmetry, e.g. a transmission grating, side-scattered light can also be coherent.

In a plasma, light is also scattered from free charged particles according to the *Thomson scattering* theory. Comparing Thomson scattering with Rayleigh scattering and the discussion on refractive index, it is obvious that the Thomson-scattered light that propagates in the forward direction is out of phase with the driving light, thus attenuating it. Incoherent, side-scattered Thomson light has been used to image light channels of very small radii, of the order of a few micrometres (Papers III and IV, and Chapter 4).

2.2 Physics At High Irradiance

The previous section dealt with the propagation of a laser pulse in a macroscopic material when the irradiance was not too high. In this section, some interactions at higher irradiances are discussed.

Consider an intense laser pulse traversing a material. On its way it forces charged particles to oscillate by the Lorentz force,

$$\mathbf{F} = Zq\mathbf{E} + Zq\mathbf{v} \times \mathbf{B}, \tag{2.8}$$

where $\mathbf{v}$ and Z are the speed and charge state of the particle, $q = \pm e$ the (positive or negative) elementary charge, and $\mathbf{E}$ and $\mathbf{B}$ the electric and magnetic field strengths of the laser pulse. The contribution to the force from the magnetic field consequently depends on the particle speed. The charged particle follows the electric field at low field strengths, but for higher field strengths corresponding to irradiances exceeding $\sim 10^{17}$ W/cm^2 when $\lambda \sim 0.8$ μm, the magnetic field force becomes equally strong and the particle motion becomes more complicated. For longer wavelengths of the laser, the particles have more time to accelerate in the field, causing the magnetic field to have an effect at lower irradiances.

This section deals with the interactions between a laser pulse and matter, from ionization leading to the generation of a plasma of free electrons and ions, to the interactions in the plasma, leading ultimately to particle acceleration, X-ray generation and relativistic channelling.

2.2.1 Ionization

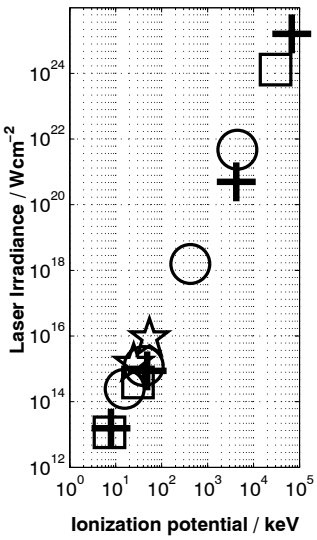

Figure 2.5. *The laser irradiance required to ionize to a certain ion charge state for: He^+ and He^{2+} ($\star$), Ar^+, Ar^{3+}, Ar^{9+} and Ar^{18+} ($\circ$), Sn^+, Sn^{3+} and Sn^{50+} ($\square$), Ta^+, Ta^{5+}, Ta^{50+} and Ta^{73+} (+).*

Focusing a laser pulse to sufficient irradiance onto a material will, to some extent, rip the material apart, even if the energy of a *single* photon is far from enough to significantly affect the atoms or molecules. No matter what the kind of material; gas, solid or liquid, multiple-photon ionization will occur. There are several theoretical models that describe ionization in different intervals of irradiance, but throughout the work in this thesis the *over the barrier* (OTB) ionization model can be used.[7]

Ionization occurs when the laser fields interact strongly with the outer atomic electrons. If the light force overcomes the force binding the electron to the nucleus, the electron leaves the atom, ionizing it. An extended "stay" in such strong fields will remove atomic electrons one after the other, up to a limit determined by the irradiance. The materials used in the present research were mainly helium, argon, tin and tantalum. Figure 2.5 shows the irradiance needed to ionize free atoms of these elements to a certain degree, according to the OTB theory. The timescale for ionization to occur once this irradiance limit has been reached is only a few femtoseconds.[8] The phase of the laser field at the time of the electron release determines the subsequent movement of the released electron to some extent. At the irradiances used in this work ($\gtrsim 10^{16}$ W/cm^2) the electron moves away from the atom in the manner described in the next section.

2.2.2 Individual Particle Motion

The motions of the ionized electrons are of central importance in both X-ray generation, which requires energetic electrons, and relativistic channelling experiments, where the relativistic motion

of the electrons changes the properties of the refractive index in a plasma. Ions are also dragged by the laser fields, but due to their much larger mass, their motion is slower and can often be neglected.

A laser pulse exerts a force on an electron, F_{Lorentz}, given by (2.8), and depending on the velocity that the electron acquires, its motion can be described non-relativistically:

$$m_e \frac{d^2\mathbf{r}}{dt^2} = \mathbf{F}_{\text{Lorentz}}, \tag{2.9}$$

where $\mathbf{r}$ is the position of the electron with mass m_e, or relativistically:

$$\frac{d\mathbf{p}}{dt} = \mathbf{F}_{\text{Lorentz}}, \tag{2.10}$$

where $\mathbf{p} = m_e \gamma \frac{d\mathbf{r}}{dt}$ is the electron momentum, including the Lorentz factor:

$$\gamma^{-1} = \sqrt{1 - \left(\left| \frac{d\mathbf{r}}{dt} \right| \Big/ c \right)^2}. \tag{2.11}$$

The kinetic energy of the electron is expressed by:

$$W_{\text{kinetic}} = m_e c^2 (\gamma - 1) \overset{|\mathbf{v}| \ll c}{\approx} \frac{m_e |\mathbf{v}|^2}{2} \tag{2.12}$$

The relativistic equation of motion (2.10) is solved in Appendix A for a simple case of a linearly polarized, plane electromagnetic-wave in vacuum (defined in Fig. 2.6) interacting with a single electron. This yields a two-dimensional movement along the x and z axes.

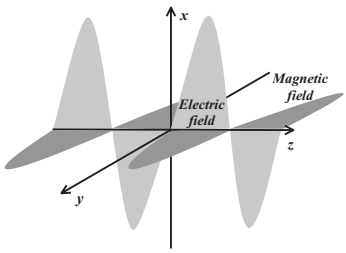

Figure 2.6. *Orientation of electric and magnetic fields in a a plane electromagnetic wave.*

In mathematical terms, using the coordinate system in Figure 2.6, the electric and magnetic fields of a linearly polarized, plane wave can be written as $\mathbf{E}(z,t) = \hat{\mathbf{x}} E_0 \cos(\omega t - kz)$ and $\mathbf{B}(z,t) = \hat{\mathbf{y}} \frac{E_0}{c} \cos(\omega t - kz)$. Generally speaking, an electron in a linearly polarized laser field oscillates along the polarization direction x, driven by the electric field, and moves forward along the light propagation direction z by the magnetic field term in the Lorentz force. The motion in the propagation direction grows faster than the polarization-directed movement for high irradiance, as can be seen in Figure 2.7, which show simulations of a laser *pulse*, 35 fs long, overtaking an electron for two different peak irradiances, 10^{17} W/cm^2 and 10^{19} W/cm^2. The relativistic equation of motion (2.10) is employed in the calculations in which a laser pulse of infinite extent in x and y direction passes by an electron initially at rest. When the pulse has high irradiance (10^{19} W/cm^2) the electron motion becomes "relativistic" in that $\gamma \gg 1$ at the peak of the pulse. This expresses itself as an almost constant oscillation amplitude at the peak of the pulse, where the velocity of the electron is very close to c. With the higher irradiance, the electron is carried quite some distance from its initial

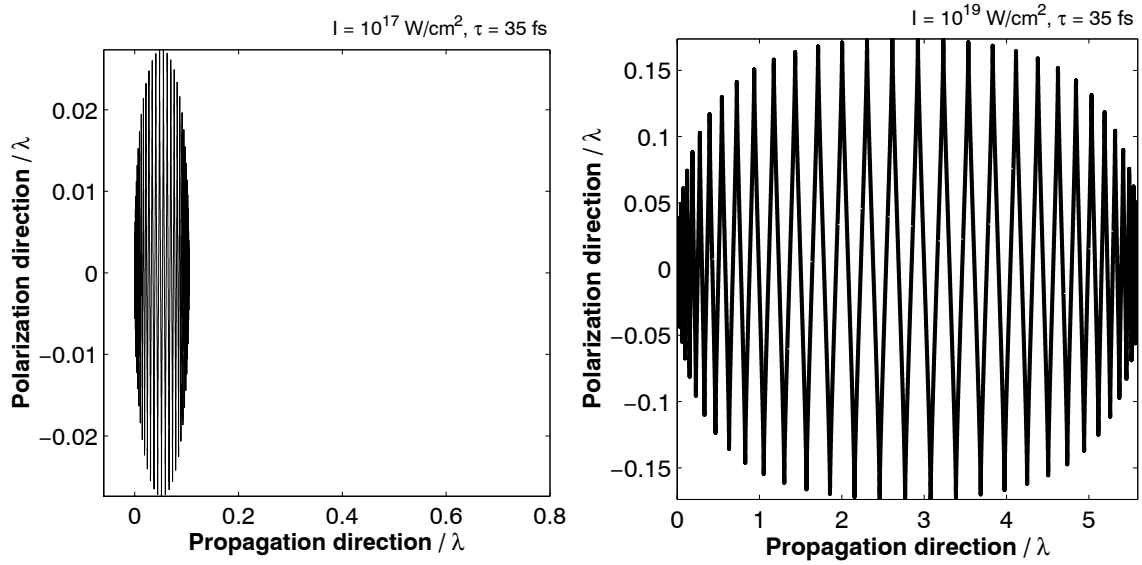

Figure 2.7. ***Left:*** *Trajectory of an electron that is overtaken by a 35 fs Ti:sapphire laser pulse with a wavelength of 0.8 μm, polarized along the ordinate and propagating along the abscissa in the positive direction. The pulse peak irradiance is* 10^{17} *W/cm*^{2}*.* ***Right:*** *Same as left but with a peak irradiance* 10^{19} *W/cm*^{2}*, causing much greater movement along the laser pulse's direction of propagation (the scaling factors between the ordinate and the abscissa are the same in both figures).*

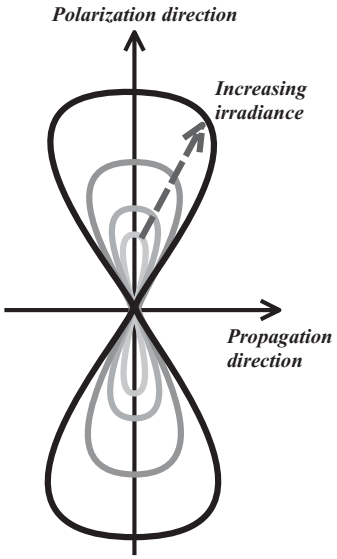

Figure 2.8. *"Figure-of-eight" motion of an electron in its own drift frame.*

position at rest, because its movement in the propagation direction of the pulse is close to c. The "figure-of-eight" motion of the electrons, as illustrated in Figure 2.8, is often referred to in this situation. This movement can be observed in a coordinate system moving along with the electron at its average velocity in the forward direction.

Turning back to the simplified condition of a plane wave in vacuum (Appendix A), the electron's average oscillation energy over one oscillation period can be expressed as a function of the irradiance, $I = \frac{1}{2}\varepsilon_0 c E_0^2$:

$$\langle W_{\mathrm{osc}} \rangle \, [\mathrm{keV}] \simeq 93 \, I_{18} \, \lambda_{\mu m}^2, \tag{2.13}$$

where the irradiance, I_{18}, is in units of 10^{18} W/cm^2 and the laser wavelength, $\lambda_{\mu m}$, in units of μm. Eq. (2.13) can be used to calculate the average Lorentz factor,

$$\langle \gamma \rangle - 1 \simeq 0.18 \, I_{18} \, \lambda_{\mu m}^2, \tag{2.14}$$

where the notation is similar as for (2.13). Table 2.1 lists average energies, Lorentz factors and electron velocities for a few different laser irradiances. At this point it is important to stress that in a plasma with many electrons and ions, the movement of any

single electron is quite different from laws of motion derived in Appendix A. In a dense plasma, simulations show that the average energy is instead proportional to $\sqrt{I\,\lambda^2}$ (Section 4.3 and Paper III).[9,10]

Table 2.1. *The average electron oscillation velocity and energy and the corresponding Lorentz factor for a few irradiance levels, using* $\lambda = 0.8\ \mu m$.

Irradiance / Wcm^{-2}	$\langle\gamma\rangle$	$\langle W_k\rangle$ / MeV	$\langle v_e\rangle/c$
10^{18}	1.1	0.06	0.25
10^{19}	2.2	0.6	0.80
10^{20}	13	6	0.994
10^{21}	116	60	0.99993

The oscillation amplitude depends on the irradiance, which varies over the pulse envelope. Electrons experience this variation in irradiance and as the laser pulse passes by they change their oscillation amplitude accordingly. The corresponding change in oscillatory energy effectively generates a *ponderomotive force*, defined as the gradient of the oscillatory energy:

$$\langle F_p\rangle = -\nabla\langle W_{osc}\rangle. \tag{2.15}$$

A focused laser pulse has an irradiance gradient that forms a *ponderomotive pressure* which pushes the electrons away from regions of high irradiance; parallel and perpendicularly to the laser pulse propagation direction.[11] The ponderomotive force can be understood by picturing the movement of the electron. For example, in the direction that the laser pulse propagates the force is manifested by the $\mathbf{v}\times\mathbf{B}$-force. In a frame moving with the average electron forward velocity, the electron performs a "figure-of-eight" motion. On the leading edge of the pulse irradiance envelope, the electrons moves forward, driven by a somewhat higher irradiance as compared to when it turns back at a position where the irradiance is slightly lower. In this way, because of the structure of the irradiance envelope the electron gains additional energy in the forward direction. The same thing occurs radially, effectively moving electrons from regions of high irradiance.

Because of the spatial irradiance gradients (cf. (2.15)), electrons that are accelerated ponderomotively do not generally copropagate with the laser pulse. The oscillatory motion of the electrons is through the ponderomotive force irreversibly converted into translation motion. The extent to which this occurs is dependent on the shape of the laser pulse envelope, its peak irradiance and its duration. The maximum electron kinetic energy can reach several MeV with existing lasers but, as will be seen in the following, this is a comparatively small energy compared with what can be achieved through other acceleration mechanisms, discussed in Chapter 3 and 4.[12]

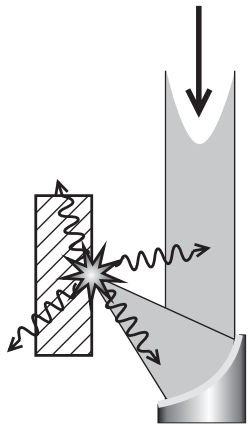

Figure 2.9. *The Ti:sapphire laser pulse is focused by an off-axis parabolic mirror and irradiates a small spot on the solid target.*

Table 2.2. *The plasma frequency, ω_{p0}, for different electron densities.*

n_e / cm^{-3}	ω_{p0} / rads^{-1}
10^{17}	$18 \cdot 10^{12}$
10^{18}	$56 \cdot 10^{12}$
10^{19}	$0.18 \cdot 10^{15}$
10^{20}	$0.56 \cdot 10^{15}$
10^{21}	$1.8 \cdot 10^{15}$

If the electron density is too high for the laser pulse to propagate, the plasma is termed overdense.

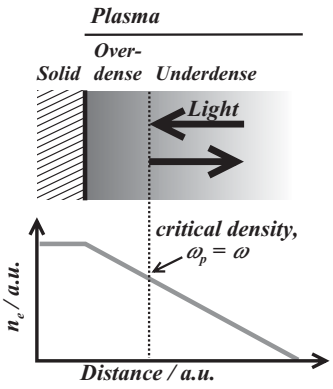

Figure 2.10. *Light with a frequency ω reflects at the location of the plasma's critical density.*

2.2.3 Interactions with a Gradient Density Plasma

Obliquely focusing a p-polarized* femtosecond Ti:sapphire laser pulse onto a solid (or liquid) target reveals many interesting interaction mechanisms; some of them are discussed here (Fig. 2.9) and in Chapter 3. The pulse ionizes the target material and subsequently reflects off the ionized material, i.e. the *laser-produced plasma*, because the plasma constitutes a mirror strong enough to withstand the irradiance. It has been found with the aid of a calorimeter that as much as 40% to 90% of the pulse energy is specularly reflected.[13,14] Utilizing an ion-chamber detector it can be found that the plasma, or something in its close vicinity, radiates X-rays. Knowing that the ponderomotive force can accelerate electrons, it is tempting to guess that the X-rays are generated when ponderomotively accelerated electrons are fired into the solid target behind the plasma and radiate through the Bremsstrahlung mechanism.

However, with more sophisticated, single-photon counting detectors, such as germanium (Ge) detectors (Section 3.2.4), it can be found that the X-ray energy distribution, indeed a Bremsstrahlung spectrum, reaches above 1 MeV already at an irradiance of 10^{17} W/cm^2.[15] This must mean that other processes are responsible for the electron acceleration.

The plasma that is formed by the pulse has an *electron density*, n_e, with the electrons flowing like a volatile fluid around the heavier ions; the sum of the charges being zero. The electrons can easily disrupt the charge equilibrium and, due to their inertia, start to oscillate at the resonance plasma frequency,[16,17]

$$\omega_p^2 \equiv \frac{\omega_{p0}^2}{\langle\gamma\rangle} = \frac{e^2 n_e}{\langle\gamma\rangle m_e \varepsilon_0}, \tag{2.16}$$

here given with a correction for the relativistic electron motion, $\langle\gamma\rangle$ (time average). Table 2.2 lists the plasma frequency for different electron densities. The electrons react much swifter to the action of the laser field and can easily disrupt the charge equilibrium, explaining why often only the electron density is considered and not the ion, or the neutral-plasma density. Moreover, as the plasma expands from the solid surface in a more or less free expansion, the electron density varies from the solid material electron density to the ambient zero level. Just as radio waves are reflected by the ionosphere (a low-density plasma), a laser pulse can penetrate into the plasma only until it reaches a point of reflection where the plasma and laser frequencies are equal (Fig. 2.10). The depth to which the pulse penetrates the plasma depends therefore on the

*When the electric field of the laser pulse is in the plane spanned by the target surface normal and the beam wavevector, the pulse is termed p-polarized. The opposite, s-polarized, occurs when the electric field is perpendicular to the plane.

laser frequency and on the electron density distribution. For example, if light with frequency ω is normally incident on a plasma with increasing electron density, the light will be reflected at the point where the plasma density reaches the *critical density*, denoted n_c. The *critical surface* refers to the surface which encapsulates the overdense region of the plasma (Fig. 2.10), i.e. the region where the plasma density is too high for light of a specific frequency to propagate. However, if the light is incident at an angle θ it will be refracted away from the high-density region. In the special case of a linearly increasing electron density the pulse reaches only to a density equal to $n_c \cos^2\theta$ (Fig. 2.11).[18] Therefore, only a normally incident pulse will penetrate all the way to the *critical surface*.

The refractive index of the plasma can be deduced from the plasma resonance frequency,[16,17]

$$n^2 \simeq 1 - \frac{\omega_p^2}{\omega^2 - \omega_p^2} \quad \Rightarrow$$
$$n \simeq 1 - \frac{1}{2}\left(\frac{\omega_p}{\omega}\right)^2, \quad \omega \gg \omega_p, \tag{2.17}$$

and this relation can be visualized in a dispersion diagram, as shown in Figure 2.12. The interpretation of the diagram is that any electromagnetic wave propagating in the plasma must exhibit a frequency and wave-number combination that puts it on the parabolic trace. At the point of reflection, the incoming and outgoing waves superimpose and *if* the laser is p-polarized, the light forms an evanescent, longitudinal electrical field, i.e. a *skin effect*, at the critical surface and drives the plasma resonantly (Section 3.2.2). The part of the pulse remaining after absorption is reflected. The skin depth, i.e. how far into the overdense plasma the evanescent light wave penetrates, is determined by the distance at which the electric field has decreased to $1/e$: $\sim \lambda/2\pi$.[17,19] Normally incident light lacks the electric field component that is perpendicular to the critical surface and cannot resonantly excite an electrostatic wave. On the other hand, obliquely incident light is reflected before it reaches the critical density. There is therefore clearly an optimum angle of incidence that gives the largest field amplitude at the critical surface, and this is given by,[18,20,21]

$$\theta = \arcsin\left[0.8(c/\omega L)^{1/3}\right], \tag{2.18}$$

where L is the scale length of the plasma.

Thus, the optimum angle depends on the *scale length*, defined as $L^{-1} = d(\ln n_e)/dz|_{n_e=n_c}$, which is a measure of how steep the density gradient is at n_c, as illustrated in Figure 2.13, and is often of the order of the laser wavelength. The size of the scale length largely governs which electron heating processes can occur in the plasma. Apart from the resonantly excited plasma wave, there are

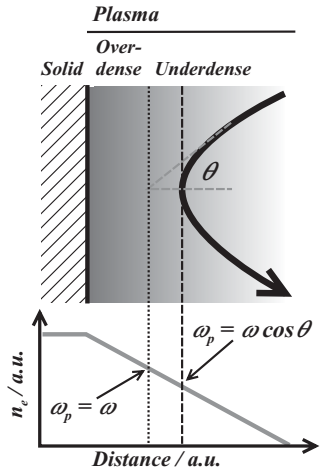

Figure 2.11. *The obliquely incident light is refracted away at the critical surface.*

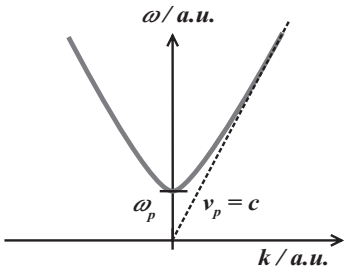

Figure 2.12. *Dispersion diagram for an electromagnetic wave in a plasma with plasma frequency ω_p.*

The critical plasma density for a Ti:sapphire pulse equals $1.8 \cdot 10^{21}$ cm^{-3}.

The skin depth is roughly 0.1 μm at the critical surface for a Ti:sapphire pulse.

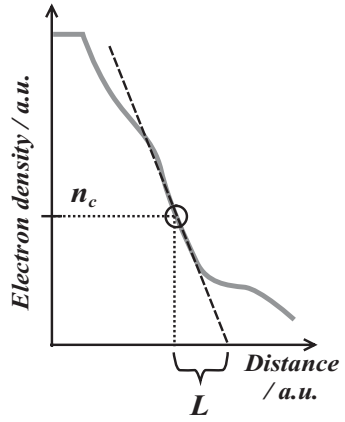

Figure 2.13. *The plasma scale length is a measure of the slope of the density gradient at n_c.*

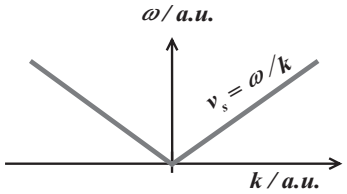

Figure 2.14. *The dispersion relation for ion acoustic plasma waves. The phase and group velocities are equal.*

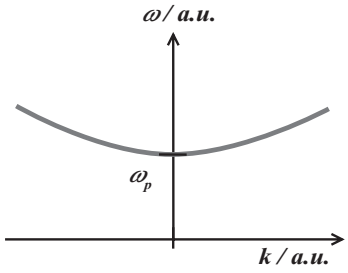

Figure 2.15. *The dispersion relation for electrostatic electron plasma waves. The group velocity, $d\omega/dk$, is much smaller than the phase velocity.*

numerous other processes, including collisions, that can heat the plasma.[18,22] Heating of the plasma is further discussed in Section 3.2.2.

Already in this introductory chapter, it is worth discussing briefly the various types of plasma waves that can occur. The simplest kinds are the electrostatic wave, i.e. longitudinal electron oscillations, and the ion acoustic wave, i.e. longitudinal ion oscillations.

The movements of the ions, which have relatively large inertia, are intimately followed by the electrons, which shield the ions and prevent the generation of large electric fields. This shielding is imperfect, however, because the electrons move also thermally. Because of this, the ion waves propagate with a velocity that is proportional to the electron temperature, T_e. In addition to this, the thermal motion of the ions, $\propto T_i$, serves to pass the wave on. The velocity of ion acoustic waves is therefore independent of the wave frequency, similar to ordinary sound waves, and the dispersion relation for the ion waves is (Fig. 2.14),[22]

$$\omega_i = k\, v_s, \tag{2.19}$$

with the velocity,

$$v_s = \sqrt{\frac{Zk_BT_e + 3k_BT_i}{M_i}} \approx \sqrt{\frac{Zk_BT_e}{M_i}}, \tag{2.20}$$

where k_B is the Boltzmann constant. The ion wave phase and group velocities are therefore equal and depend on the electron temperature, T_e, the ion temperature, T_i (T_i is often much smaller than T_e on short timescales), and the mass and charge of the ions, M_i and Z.

On the other hand, the rapidly moving electrons are not hindered by the comparatively fixed ions. The electron plasma waves, oscillating with the fixed plasma frequency, ω_p, do not normally propagate faster than the thermal motion allows, i.e. the group velocity, $d\omega/dk$, is proportional to the average thermal velocity, v_{th}. The dispersion relation for a propagating plasma wave is (Fig. 2.15):[18,22]

$$\omega_{ek}^2 = \omega_p^2 + k^2\, v_{th}^2, \tag{2.21}$$

$$v_{th} \simeq \langle v \rangle = \sqrt{\frac{8k_BT_e}{\pi m_e}} \quad \text{(3D equilibrium plasma)}$$

The phase velocity, however, is arbitrary and is determined by the way in which the plasma wave is driven. For example, if the wave is driven by a laser pulse or an electron bunch, the phase velocity equals the velocity of the pulse or bunch. Before leaving the subject of plasma waves, it should be noted that with the addition of static electric or magnetic fields many more types of plasma waves can be generated.[22]

Returning to the focusing of the laser pulse, the light undergoes a tremendous momentum change upon reflection, supported by the plasma at the critical density. The momentum change generates a light pressure, p, which can be deduced from the instantaneous irradiance, $I(t)$;

$$p(t) \simeq \frac{I(t)\cos\theta}{v_g}, \tag{2.22}$$

where θ represents the angle of incidence (Fig. 2.9). The light pressure forces the bulk of the plasma expansion to slow down, and if the pulse is intense enough it even compresses the plasma and generate a steeper plasma density gradient (Fig. 2.16).

The interaction of lasers with a gradient density plasma is discussed in more detail in Chapter 3, where experimental work on X-ray generation is presented.

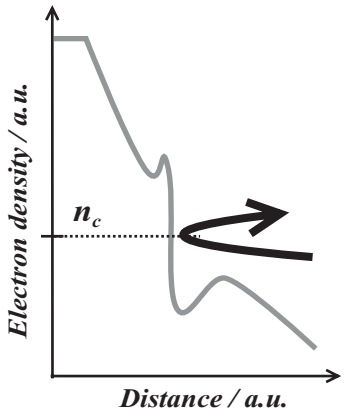

Figure 2.16. *The expanding plasma is stemmed by the reflecting laser pulse, which in this figure manages to compress the plasma, forming a very steep electron density gradient with a small scale length.*

2.2.4 Interactions with an Underdense Plasma

Turning to the interactions between an intense femtosecond laser pulse and a gas, many things correspond to the theory above. Most experiments are performed in an evacuated chamber to prevent the pulse from being distorted in air. A gas valve prepares a jet of gas at the laser focus (Fig. 2.17). The gases used in the work described in this thesis are helium (see Chapter 4) and argon (see Section 3.3). The laser pulse ionizes the gas as it travels through the jet. In the case of helium, the electron density generated is directly determined by the local gas pressure, because helium is completely ionized (cf. Fig. 2.5). Argon, however, can only be partially ionized. The valve provides for a wide range of pressures, from very low pressures up to about ten times atmospheric pressure ($n_e \sim 10^{20}$ cm^{-3}); producing penetrable, *underdense* plasmas for Ti:sapphire laser pulses.

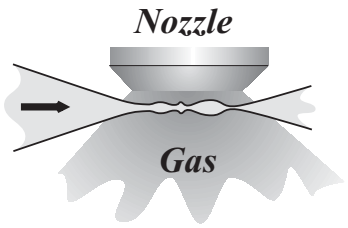

Figure 2.17. *The laser is focused into the gas, which is emitted by the orifice of a gas valve. The backing pressure on the valve is around fifty times atmospheric pressure, and the valve opens for a few milliseconds before the laser pulse arrives. The gas density can be as high as ten times atmospheric pressure in the interaction region (ten times lower than the critical density for Ti:sapphire laser pulses).*

The gas pressure is determined by the size of the nozzle orifice and by the gas pressure backing the valve. When using a very high backing pressure of several tens of atmospheres and allowing the gas to expand into vacuum, the gas cools rapidly. In the case of argon, it liquifies or freezes and forms clusters (see Paper I and Section 3.3). The laser pulse interacts quite differently with clusters than in a smooth underdense plasma, in simple terms because the clusters are overdense and because they explode due the strong repulsive Coulomb forces between the ions. Cluster plasmas can be heated to very high electron temperatures because of the sudden release of energy by the Coulomb explosion and the energetic electrons can promote nuclear reactions in the plasma. The laser energy can be efficiently absorbed in a cluster plasma. The size of the clusters depends on the orifice size and the backing pressure.

In contrast to this, the experiments presented in Chapter 4 require a smooth plasma density profile. Because of this, helium

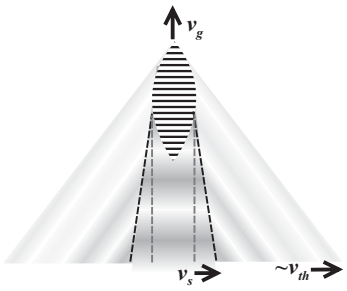

Figure 2.18. *The propagation of a laser pulse in an underdense plasma. The trailing plasma wave can be visualized as a boat (the laser pulse) travelling on the water surface, continuously pushing water aside. Behind the boat appears a wake (the plasma wave), propagating with the same speed and direction as the boat.*

is the gas chosen for these experiments. The helium plasma supports orderly propagating plasma waves which can be driven by an intense laser pulse. The early part of the pulse continuously ionizes the gas and the following part interacts with the plasma. The underdense plasma has a collective resonance frequency (the plasma frequency, ω_p), causing, for example, Raman scattering from electron plasma waves. In addition, Thomson scattering occurs to a large extent in the plasma when light scatters from free electrons. The laser focus provides a small-scale plasma laboratory that can be utilized to study various interactions between plasma and laser pulses. The light pulse moves with the group velocity, v_g, through the plasma and pushes electrons from the regions of highest irradiance by the ponderomotive force. Thus, the electrons start to oscillate at the plasma frequency and a longitudinal plasma wave with a phase velocity of v_g forms, co-propagating with the laser pulse (Fig. 2.18). The wavelength of the plasma wave is:

$$\lambda_p = \frac{2\pi v_g}{\omega_{ek}}. \tag{2.23}$$

This plasma wave is metaphorically termed a *wake*. The wavelength of the wake is listed for selected electron densities in Table 2.3.

Table 2.3. *The wavelength of a plasma wave (wake) co-propagating with a laser pulse in plasmas with different electron densities. The relativistic Lorentz factor was one (1) and the plasma temperature was zero.*

Electron Density / cm^{-3}	λ_p / μm
10^{18}	~ 30
10^{19}	~ 10
10^{20}	~ 3

The amplitude of the trailing plasma wave depends on the duration of the laser pulse; the wave is best excited with a laser pulse with a duration that is roughly half the period of the plasma wave. However, if the laser pulse duration is several times the plasma period the laser pulse is modulated by the plasma in a complex process involving Raman scattering and a varying group velocity over the pulse envelope. The outcome is that the laser pulse is bunched into a train of laser pulses, each half a plasma period long. These pulses repeatedly and resonantly excite the plasma wake. Plasma electrons can surf on the plasma wake fields and thus acquire high kinetic energies. This mechanism is called wake-field acceleration (WFA) or self-modulated wake-field acceleration (SMWFA) for longer laser pulses that are modulated by the plasma. There is a limit to the amplitude of a plasma wave, determined by the movement of the electrons. If the longitudinal electron oscillation amplitude exceeds half the plasma wavelength,

causing electrons from one wave period to enter the neighbouring periods, *wave breaking* will occur and the wave starts to collapse. For a given electron density, n_e, and a given phase velocity of the plasma wave, v_{pp}, the maximum electric field in the wave becomes,[23]

$$E_{max} \simeq \frac{m_e \omega_{p0} c}{e} \cdot \sqrt{2\,(\gamma_{pp} - 1)}, \tag{2.24}$$

where $\gamma_{pp} = 1\Big/\sqrt{1 - (v_{pp}/c)^2}$ is the Lorentz factor for the phase velocity of the plasma wave. Taking, for example, the plasma frequency for an electron density of $n_e = 10^{19}$ cm^{-3}, the maximum field is found to be 0.3 TV/m for a modest γ_{pp} of 1.5. This value should be seen in relation to, for example, the maximum field in a linear accelerator (LINAC), which is only 20 MV/m. There are other acceleration mechanisms that do not involve plasma waves, such as direct laser acceleration and ponderomotive acceleration, both discussed in Section 4.1.5.

The electrons that are propelled forward by the acceleration mechanism increase their mass, but more importantly the whole bulk of electrons in the laser field oscillates and acquires relativistic energies in this motion, as discussed above. Therefore, the bulk of electrons becomes heavier lowering the plasma frequency (cf. (2.16)). If this happens in the case of an overdense plasma, a kind of *relativistic plasma transparency* is induced by increasing the critical density of the plasma, allowing the laser pulse to penetrate to higher densities, which is useful in certain fusion schemes (Chapter 5). Furthermore, the refractive index depends on the laser irradiance, as in (2.5), and another kind of self-phase modulation can occur, namely *relativistic self-phase modulation*, discussed in Section 4.1.4.

The fact that the refractive index depends on the irradiance can be used to focus and guide the pulse with a self-generated relativistic "lens"; *relativistic self-focusing*. The irradiance in the focus decreases radially, which imposes a radially decreasing refractive index on the plasma which focuses the light. The laser pulse is confined to one or several, nearly diffraction-limited, *relativistic channels*. The length of the channels can be altered by modifying the laser pulse parameters or the plasma density, as discussed in Chapter 4, and Papers III and IV.

Chapter 3

X-ray Generation

This chapter starts with a brief introduction to how X-rays are generated and how they interact with the materials in which they propagate. The first subject is very important in the experiments generating X-rays, and the latter is important as soon as the X-rays are detected by some kind of detector, which is done in all the experiments in this chapter. The art of detecting X-rays can be very complicated as will be seen in the following. The experiments generating X-rays by focusing the laser pulses onto solid targets are presented first, in Section 3.2, with a discussion on the measurement techniques. Thereafter, in Section 3.3, the X-ray generation experiment using an argon cluster target is briefly discussed. Following this, Section 3.4 give some introductory information on the experiment carried out at the European Synchrotron Radiation Facility (ESRF), where synchrotron radiation was used to probe phonon vibrations in an indium antimonide (InSb) crystal. Finally, a summary of all the experiments is given, including future prospects for laser-generated X-rays and their applications.

3.1 Generation, Absorption and Scattering of X-rays: Theory

3.1.1 Bremsstrahlung and Characteristic Radiation

In order for X-rays to be generated, electrons must suddenly undergo some kind of acceleration or deceleration. If this happens through collisions with nuclei, accompanied by the emission of a photon, the process is called *Bremsstrahlung* (Fig. 3.1). Elastic collisions with nuclei (and with electrons, although with a much lower probability) also occur, but these are of little consequence when generating X-rays. Inelastic collisions with atomic electrons lead to ionization and the emission of characteristic radiation.

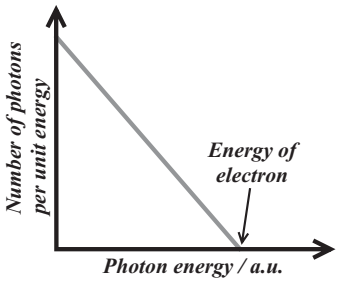

Figure 3.1. *An electron that is decelerated by colliding with atoms generates a radiation spectrum that is* similar *to the trace in this figure; i.e. a linear distribution that extends up to the electron energy.*

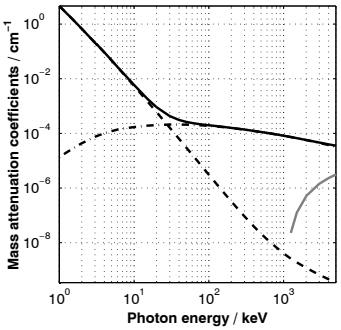

Figure 3.2. *Mass attenuation coefficients for air: μ_a (−−), μ_C (− · −), and μ_p (solid grey). The sum of all coefficients is plotted as a solid black trace. The data were taken from the NIST web site.*[25]

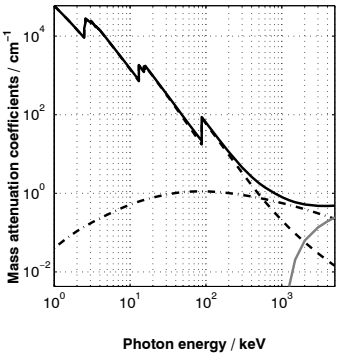

Figure 3.3. *Mass attenuation coefficients for lead: for key see Figure 3.2.*

In simple terms, the Bremsstrahlung efficiency is proportional to the atomic number of the material. In Paper V a model is used to calculate the absolute number of Bremsstrahlung photons. There are also models describing the generation of the characteristic radiation,[24] but since this radiation only constitutes a small part of the total emitted X-ray energy in most of the experiments presented in this chapter, these models are not discussed here.

3.1.2 Absorption and Scattering of X-rays

A large part of the work on X-ray generation presented in this thesis have dealt with X-ray detection. In this work, absorption and scattering of X-rays are important processes. For example, when focusing onto solid targets, hot electrons penetrate the solid target. Directly inside the target there is significant absorption of the generated X-rays, although some of the absorbed energy is re-emitted as characteristic line emission of the material. Well outside the target, the X-rays must normally pass through air and one or more windows on the way to the detection equipment. Further absorption and scattering can thus distort the measured X-ray spectrum. Photoelectric absorption is the main process up to roughly 100 keV (depending on the material), at which Compton scattering (incoherent scattering) takes over as the most important mechanism. In addition to this, X-rays with energies above $2m_ec^2$, i.e. ~ 1 MeV can create electron-positrons pairs. Figures 3.2 and 3.3 show, for air and lead, the behaviour of the various X-ray interactions with matter in the form of mass attenuation coefficients. These express the probability of the different scattering and absorption events as the ratio of the transmitted, unaffected radiation irradiance I_T to the incident irradiance I_0,

$$\frac{I_T}{I_0} = \exp\left[-(\mu_a + \mu_C + \mu_p)\,\rho\,\Delta x\right], \tag{3.1}$$

where μ_a, μ_C, and μ_p denote the mass attenuation coefficients for photoelectric absorption, incoherent scattering and pair creation in the nuclear field. The material density is ρ and Δx is the thickness of the material through which the X-rays penetrate.

In the photon energy region that is discussed in this thesis, i.e. up to 0.5 MeV, the most important interactions are photoelectric absorption and Compton scattering. These effects govern the complicated task of detecting the X-rays in various detectors, i.e. semiconductor detectors, scintillators, ion chambers and image plates. Photoelectric absorption is quite straightforward. In this process, the incident photon is completely absorbed by an atom, and an electron is ejected from the atom at a high speed. Subsequent collisions between the electron and other bound electrons lead to the deposition of the photon's energy in the material, provided that the fast electrons remain in the material/detector.

The Compton scattering process can be modelled semi-classically as the collision of a photon with an electron, as illustrated in Figure 3.4.The electron gains only part of the photon energy. The highest energy that can be transferred from a photon with energy E_p to an electron in a single Compton scattering event follows a simple rule that can be deduced from the laws of energy and momentum conservation;

$$E_e\big|_{max} = \frac{E_p}{1 + m_e c^2 / 2E_p}. \tag{3.2}$$

Thus, the maximum fraction of deposited energy increases nonlinearly with the photon energy (Fig. 3.5). The photon can Compton scatter any number of times before leaving the material and if the material has a large volume all the photon energy can be converted to fast electrons in the material through a series of Compton scattering events and finally photoelectric absorption.

The famous Klein-Nishina formulas from 1928, based on quantum mechanics, allow Compton scattering theory to be used to predict the statistical angular distribution of the scattered photons and the Compton electrons (Figs 3.6 and 3.7) and the statistical energy distribution of the electron that receive energy from the photon (Fig. 3.8).[26] The cross-sections together with the X-ray irradiance, the material electron density and the area on which the radiation is incident, allow calculation of the average number of Compton events and their outcome, per unit distance in the material.

It is clear that Compton scattering effectively increases the absorption. Not only does the photon deposit some of its energy when it scatters, but because of its reduced energy, the probability for photoelectric absorption increases (Figs 3.2 and 3.3). The mass energy absorption coefficient is a measure of the total *absorbed* energy in a material, including Compton scattering and pair creation. It should be clearly distinguished from the mass attenuation coefficient which only measures the probability of a particular interaction mechanism, not the outcome of the interactions. The mass energy-absorption coefficient, μ_{me} [cm^2/g], can be used to calculate the absorbed dose,

$$D\ [\text{Gray}] = I_x \exp\left[\mu_{me}\, \rho\, \Delta x\right] \approx I_x\, \mu_{me}, \tag{3.3}$$

where I_x denotes the X-ray irradiance.

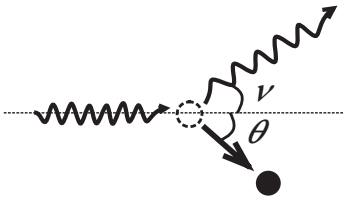

Figure 3.4. *Definition of scattering angles in a Compton scattering event.*

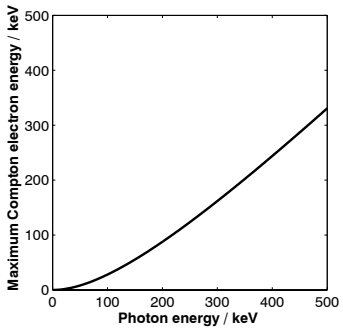

Figure 3.5. *The maximum energy that can be transferred from an X-ray photon to an electron in a single Compton scattering event.*

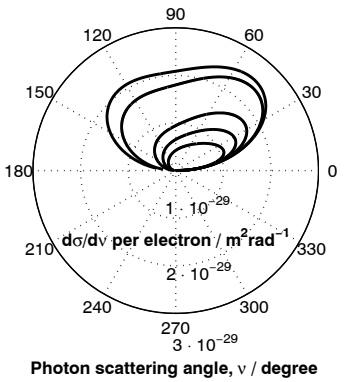

Figure 3.6. *Number-versus-angle distributions for Compton scattered photons with energies 50 keV, 0.1, 0.5, 1 and 2 MeV. The largest cross-section is for the 50 keV photon.*

3.2 X-rays from a Solid Target

This section presents X-ray generation experiments, in which the X-rays are produced by focusing laser pulses onto solid metallic targets. Both arms of the ten-hertz laser and also the kilohertz laser were used in this work. The ten-hertz laser produces several

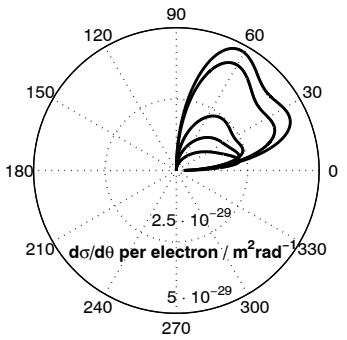

Figure 3.7. *Number-versus-angle distributions for Compton electrons generated by X-ray photons with energies 50 keV, 0.1, 0.5, 1 and 2 MeV. The largest cross-section is for the 50 keV photon.*

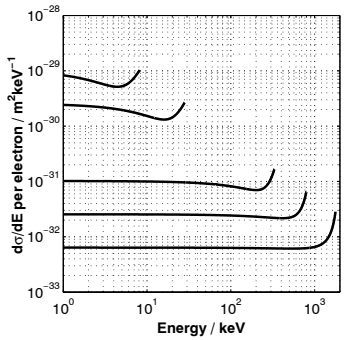

Figure 3.8. *The cross-section for the deposited energy in a single Compton scattering event show a characteristic curved shape. The traces, starting with the uppermost and proceeding downwards, are generated by photons with the energies 0.05, 0.1, 0.5, 1 and 2 MeV.*

hundred times more energy per pulse than the kilohertz laser with only a millijoule per pulse (Paper V). At first glance, it may appear that experiments with the kilohertz laser imply a step backwards, but this is not the case. The period since 1992 at the Lund High Power Laser Facility has directed the so-called X-ray generation project into the main branch: laser-produced hard X-ray generation and applications. The meaning of *hard* X-rays differs between the physics communities, but here it means photon energies above a few keV. The applications of X-rays are numerous, but perhaps the most apparent is medical diagnosis: i.e. imaging of parts of the body and diagnosing diseases. The long-standing collaboration of the Lund High Power Laser Facility with the Lund University Hospital makes comparative investigations of the laser-based X-rays and radiation from the common X-ray tube feasible. Presently, the average emitted X-ray power from an X-ray tube is 10–1000 times higher than from a laser-produced plasma.[27] The motivation for the research described in this thesis, to investigate lower laser powers, is simple: *almost all applications of X-rays require a high average flux of photons with energies below 100 keV*. Using increasing laser irradiance will not only increase the flux of photons below 100 keV, but also extend the X-ray spectrum to higher energies. This relationship between laser power and the characteristics of the X-ray spectrum has been found through research, and has spurred research at the Lund High Power Laser Facility into using a laser system with a high repetition rate, i.e. the kilohertz laser. The idea is that with very short laser pulses ($\lesssim 30$ fs) and high repetition rate, hard X-rays could be generated by a more compact source with increased average power, better suited to clinical applications. A future X-ray device based on a laser should be compact and simple to use, compared with the X-ray tube. Therefore, employing the smaller kilohertz system is one important step in the right direction.

The research at the Lund High Power Laser Facility dealing with X-ray generation by focusing laser pulses onto solid targets actually began already in 1992 with the work by C. Tillman and others, using the original ten-hertz laser system. The applicable qualities of the laser-produced X-rays were investigated early in a series of experiments which were published in both physical and medical journals.[28–30] M. Grätz continued along this path and his and Tillman's theses provide a rather sharp-sighted evaluation of the potential of laser-produced X-rays in medicine.[27,31,32] Aspects of X-ray imaging, such as magnification,[29] differential imaging,[30,33,34] and time-gated imaging and tomography,[35–38] were investigated. Tillman also evaluated the effects of exposing living cells to short, intense X-ray bursts from the laser plasma compared with exposure to the nearly constant X-ray flux from an X-ray tube.[39] The two cases were found to be statistically undistinguishable, which paves the way for future use of laser-based X-rays in

medicine. Several studies employing high-resolution spectroscopy of the characteristic X-ray emission were also performed.[40,41]

The laser-produced plasma can constitute a very useful, pulsed source of X-rays and, as shown in Paper V, medical applications in which the properties of laser-produced X-rays can be beneficial are not far away. The laser-produced X-rays exhibit properties such as short pulse duration and small source size, which can be of great importance in some applications; either where a short X-ray probe is needed or where high magnification is an issue. Additionally, X-ray imaging with maintained image contrast but a lower absorbed dose can be achieved with the short pulses used in combination with time-gated, two-dimensional detectors.[37] M. Grätz showed that the temporal resolution of the detector should be of the order of 10 ps in order to suppress scattered radiation and such detectors are now being developed. Thus, the laser-based X-ray source is not only an interesting alternative to the X-ray tube, it also exhibits important complementary features that might be used to lower the absorbed dose to the patient, lowering the risk for radiation-induced diseases.

The next part of this section presents the X-ray tube, theory, experimental set-up, measurements and results from experiments in which laser pulses were used to generate X-rays by focusing onto solid, metallic targets.

3.2.1 The X-ray Tube

Today, the most commonly used X-ray source in medicine is the X-ray tube and it is in relation to this source that the laser-based source should be judged. An X-ray tube consists of an electron-emitting wire cathode,from which the electrons are accelerated by a high voltage (28 kV to 140 kV) over a distance of a few centimetres, usually onto a rotating rhenium-tungsten alloy anode (Fig. 3.9), generating a typical Bremsstrahlung spectrum together with characteristic radiation from the cathode material.[42] The electrons are also focused because this enhances the imaging properties, especially at high magnification. The typical focus size is one to two millimetres in diameter, but only 0.1 mm for mammography tubes, i.e. in general much larger than the laser-based source. The X-ray tube is a very flexible and user-friendly instrument; the tube voltage, current and exposure time are easily set to suite the type of diagnosis and the size of the patient (Table 3.1). The voltage,

Table 3.1. *Typical X-ray tube voltages.*

	Voltage / kV
Kidney	80
Chest	140
Woman's breast	30

The X-ray tube anode metal is chosen depending on the tube voltage. In mammography for example, where X-rays below ∼ 30 keV are produced, it is common with molybdenum.

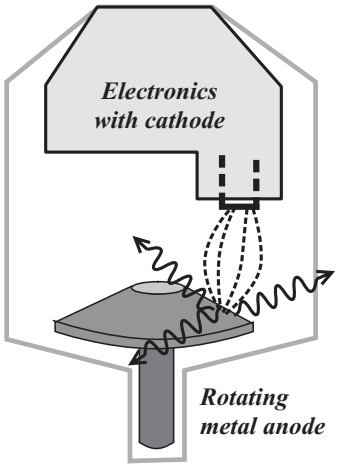

Figure 3.9. *The principle of the X-ray tube. The device is encapsulated in a evacuated glass tube. The large amount of heat produced is the main operational difficulty with the X-ray tube.*

for example, is determined by two opposing factors. The average X-ray energy should be as low as possible, in order to enhance the little contrast there is between different body organs, while the average energy should be high in order to lower the dose given to the patient. A compromise must be chosen, but in certain cases, such as lung imaging, the voltage can be high (140 keV), thin copper foils being used to remove the lower part of the spectrum, as the contrast between the lungs (mostly air) and the surrounding tissue is unusually good. The exposure time can be very short, of the order of a millisecond, for simple diagnostic imaging using *image plates* (cf. Section 3.2.4), but as long as several minutes, for example, when performing certain surgical procedures. In the latter case a real-time detector is used and the X-ray flux is relatively low, which means that the image quality is poor, revealing only crudely what the doctor wants to observe. The absorbed dose in the patient is relatively high in these long exposures, much higher than in ordinary diagnostic imaging, which normally results in a few tens of microgray.

The X-ray radiation from X-ray tubes in common medical diagnosis is a nearly constant flux in time, whereas the X-ray burst from laser-produced plasmas on solid targets are extremely short in time ($\lesssim 10$ ps).

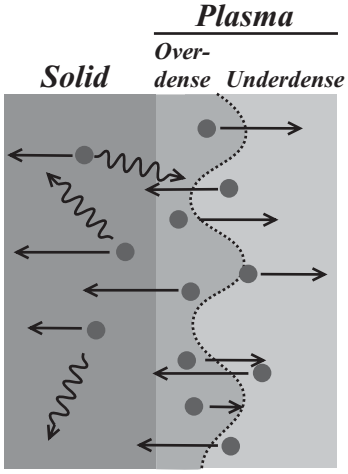

Figure 3.10. *The electrons that reach the solid generate X-rays through deceleration, i.e. Bremsstrahlung. Notice the critical surface, which is rippled (exaggerated) due to the interfering incoming and outgoing light. The ripples move like a surface wave with a velocity determined by the angle of incidence.*

3.2.2 Plasma Heating: Theory

Focusing a p-polarized laser pulse obliquely onto the surface of a solid target, transiently forms a plasma when the first part of the pulse arrives, or a pre-plasma that already exists is quickly reinforced. The plasma rapidly expands (cf. (2.20)) and the density profile decreases exponentially from the surface at a rate determined by the scale length, $L^{-1} = d(\ln n_e)/dz\big|_{n_e=n_c}$. The peak of the pulse propagates through the plasma and, unless processes such as relativistic self-focusing set in, it continues until the point of reflection, near the critical surface, where it forms an interference pattern from the interfering incoming and (the weaker) outgoing light (Fig. 3.10). The light incidence angle and polarization determine the nature of the interference wave and thus largely determine the interaction with the plasma (e.g. (2.18)). For X-ray generation it is important that some mechanism heats the electrons to high temperatures and that the electrons are subsequently propelled into the adjacent solid, where they generate Bremsstrahlung radiation (Fig. 3.10).[43,44] The generation of hot electrons required for hard X-ray generation using an obliquely focused, p-polarized laser pulse is described below.

The processes that heat the plasma, i.e. that transfer energy from the laser pulse to the plasma, ultimately determine the electron and ion kinetic energy distributions. The plasma ion or electron temperature are often referred to in the literature, the latter being a measure of the electron energy distribution. However, the original concept of temperature is as a measure of random movement at thermodynamical equilibrium, where the electrons and ions have had time to "thermalize", i.e. to distribute their en-

ergy by collisions. Contrary to this, the present overdense plasma experiments often lead to a more or less one-dimensional transient movement with an associated energy distribution that does not necessarily coincide with the equilibrium distribution (The Maxwell-Boltzmann distribution).[20,24,45–47] In spite of this fact, many experiments measure equilibrium-like electron distributions that can be described either as a single Maxwell distribution, $f(E)$, or a sum of several such distributions with different temperatures and electron numbers (Paper V):[19,20,24,43,48]

$$\frac{df(E)}{dE} = N_e \frac{(E_T)^{-\frac{1}{2}\nu} E^{\frac{1}{2}\nu-1}}{\Gamma\left(\frac{1}{2}\nu\right)} \exp\left(-E/E_T\right). \tag{3.4}$$

Here the temperature is expressed by the energy $E_T = k_B T$, where k_B is the Boltzmann constant and the number of electrons integrated over all energies, E [J], is N_e. Values of the gamma function, Γ, can be found in tables. The dimensionality, ν, can often be chosen arbitrarily, because it does not have a significant effect on the high-energy tail of the distribution (which is usually measured).[24,49] Most measurements of the electron temperature are performed indirectly by measuring the X-ray spectrum and from this reconstructing the electron distribution.[20,48–50]

The plasma ions also move because they are coupled to the laser field, as well as to the movement of the electrons, but their motion is much more difficult to assess experimentally. The velocity and the movement of the ions are also much smaller than those of the electrons and in several models of laser-produced plasmas the ions are assumed immobile. In some cases, however, such a simplification leads to inaccurate results and it has been shown that the ions can play an important role in the heating of the electrons.[46]

As soon as the electrons or ions move, due to the oscillations in the light field or due to induced plasma waves, they start colliding with neighbouring particles. The collisions effectively thermalize the plasma, i.e. local temperature differences are evened out and the temperature approaches equilibrium. The collisions also lead to a transfer of energy from the laser field to the plasma (Fig. 3.11). However, this *collisional absorption* or *inverse Bremsstrahlung* is usually inferior to other heating mechanisms at irradiances above 10^{15} W/cm^2 ($\lambda = 0.8$ μm).[19,51,52] This is because the temperature rises much quicker locally than the collisions can thermalize and the mean free path of the electrons increases as the quiver velocity increases.[53,54] Therefore, for very intense laser pulses, the collisions in the critical density region seem to confer a temperature on the overdense plasma of about 1 keV, more or less independently of the exact laser pulse parameters.

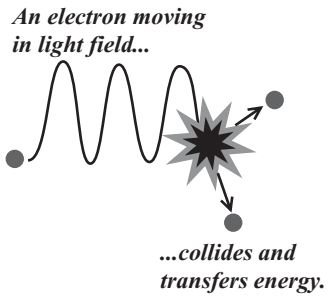

Figure 3.11. *The de-phasing of the electrons relative to the laser field heats the plasma.*

Returning to the experimental situation with a solid target subjected to a focused laser pulse, the obliquely incident laser pulse is refracted from the high-density region before it reaches the criti-

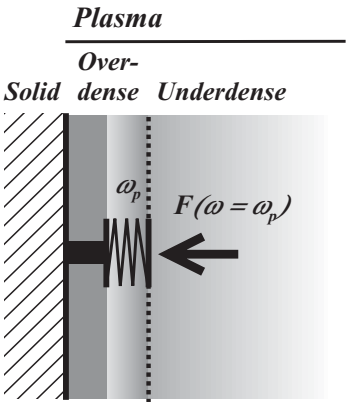

Figure 3.12. *An analogy where a force acting with a frequency ω (light), acts on a spring with resonance frequency ω_p (plasma).*

cal surface, but the laser fields tunnel to it by means of the skin effect (see Section 2.2.3). Since the electric field has a component directed perpendicularly to the critical surface, it can resonantly excite an electrostatic wave (electron plasma wave).[18,20,45,46,51,55] This is illustrated in Figure 3.12. This wave efficiently absorbs the energy in the optical field, a process called *resonance heating*, while collisions slowly transfer energy from the quickly growing wave to the plasma in an attempt to thermalize it. As the resonant plasma wave grows, it finally reaches a limit where its electric field can eject electrons in less than a single oscillation cycle, causing *wave breaking*. Furthermore, the high-amplitude static wave will decay into waves that propagate from the critical density region. The overdense part of the plasma, for example, is kept "locked in" by the solid surface on one side and the light pressure on the other. In this cavity, excited electron plasma waves can oscillate and reflect back and forth, while depositing their energy partly as an increase in the overdense plasma temperature and partly as suprathermal electrons that are heated through, for example, *Landau damping*. This process can, at least figuratively speaking, be seen as electrons surfing on the electrostatic wave and gaining energy (see also Section 4.3.2).[18,22] This additional mechanism transfers a great deal of energy from the wave to the plasma, and effectively limits the resonant growth. Resonance heating, as a whole, can generate suprathermal electron distributions with temperatures that scale with the laser irradiance as $T_{hot} \propto \left(I\,\lambda^2\right)^{0.33}$.[18–20,45,48] By using absolute scaling laws given by Gibbon and Förster[19], Forslund et al.[20], Beg et al.[48] and experimentally by Pretzler et al.[43] and assuming a laser irradiance of 10^{16} W/cm^2, i.e. similar to the conditions in the experiment presented in Paper V, it is found that resonance heating can generate suprathermal electron distributions with one or two temperatures in the region of 5 keV to 50 keV.[46]

If the laser pulse is sufficiently intense it can compress the plasma due to momentum transfer and decrease the scale length, thus changing the conditions for the various heating mechanisms (Fig. 2.16).[18,46] Among other things, the distance from the point of reflection to the critical surface decreases, which leads to enhanced resonance heating. This can also occur if the laser pulse is very clean, i.e. the level of ASE and pre-pulses is very low, and the optical field has a better chance of directly accelerating electrons into the plasma. Brunel suggested in 1987 that a *vacuum heating* mechanism could heat the plasma in such a situation.[56] In this process, electrons are "ripped out" from the high-density regions and are accelerated for less that a laser period, in near-vacuum, and subsequently propelled into the overdense region, leaving the laser field behind.[46,51,55] In one such acceleration period the electron may acquire as much as 3.2 times the quiver energy, classically $\sim 3.2 \cdot m_e\langle v_e^2\rangle/2$.[56] (It is interesting to see that this particular

Brunel heating *or* vacuum heating *can occur under similar conditions to resonance heating, but only if the plasma scale length is sufficiently short, allowing electrons to leave the high-density region, move out into the vacuum by the optical field and return with high energy to the overdense plasma.*

electron energy relation of 3.2 times the oscillation energy finds its counterpart in high harmonic generation, where an electron leaves the core of the atom and returns approximately half a cycle later.[57–60]) In most realistic experimental conditions, the plasma scale length is too long to allow pure vacuum heating, but if the scale length is reasonably short, i.e. $L \lesssim 0.5\lambda$, a complex combination of resonance and vacuum heating can occur that can heat the electrons to even higher energies than is possible with either mechanism alone.[55]

Apart from collisional and resonant heating, other heating processes occur that generate plasma waves and which require matching of wave vectors and frequencies; so-called *parametric instabilities*. A few important examples of this type of instability are the two-stream instability, the parametric decay instability and the two-plasmon decay instability.[18,22,61–64] All these phenomena require that the light field decays into one or several electron or ion waves, and that the waves grow in an unstable manner, quickly gaining amplitude; often the plasma waves grow from only small plasma density ripples and noise. The instabilities can occur in short periods during the interaction of the light with the plasma, and can, in one way or another, produce bursts of hot electrons.

It is worth mentioning that the interaction of s-polarized light or normally incident light with the plasma differs markedly from the processes discussed here, mainly because of the lack of the electric field component directed into the overdense plasma. Instead, the normal skin effect and the *anomalous skin effect* predominate as heating mechanisms for the plasma electrons.[65,66] The anomalous skin effect is similar to the normal process, except that the excursion of the oscillating electrons exceeds the skin depth, effectively carrying the light energy further into the plasma.

3.2.3 Experimental Set-up

The set-up described in this section is that used in the experiments presented in Papers II and V, and in other experiments using solid targets presented below. However, in some experiments the multiterawatt arm of the ten-hertz laser was used, and in others the smaller, kilohertz laser. The set-ups in these cases differ somewhat, because different detectors and target devices are employed. Therefore, the description here will be on a general level, where the differences are small. More detailed descriptions of the ten-hertz and kilohertz laser experiments are given in Papers II and V.

Experimental Chamber

Figure 3.13 shows the experimental chamber. The horizontally polarized laser pulse propagates through a fused silica window to enter the evacuated chamber. The pressure in the chamber is kept

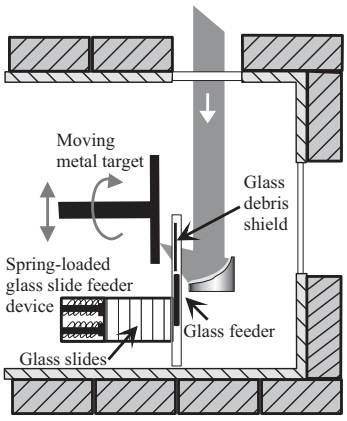

Figure 3.13. *The set-up for X-ray generation with a section of the evacuated aluminium chamber and the lead bricks surrounding it. The laser beam is 25 mm in diameter and is focused by an $f/1$ mirror, through a thin glass plate, onto the rotating and translated solid target. The cassette and feeder which permit the glass to be changed during operation are also sketched.*

at about 10^3 Pa as a compromise between the distortion of the laser pulse in air and the mean free path of the debris.[27] A low pressure is preferred to minimize laser pulse distortion, while a high pressure limits the range of the debris. The X-rays exit through a large 15 cm diameter, 180 μm thick plastic window, which is chosen to be thin and of a low-Z material in order to minimize its influence on the transmitted X-ray radiation (see the discussion on absorption and scattering in Section 3.1). The chamber is enclosed in 5 cm lead that effectively blocks the X-ray radiation up to several MeV.

Focusing Mirror and Debris Shield

The laser pulse is focused very tightly by an $f/1$, gold-coated, off-axis parabolic mirror. The angle of incidence onto the target is 30°; an angle that is close to the optimum found in other experiments.[21,45,67,68] The parabolic mirror is aligned by first removing the solid target device, and then observing the spark caused by the focused laser pulse in air. By gradually lowering the laser pulse energy while adjusting the mirror mount and maintaining a visible spark in the focus the optimum mirror alignment can be achieved. This method may seem very approximate, but inspecting the focus by imaging it with a CCD camera has shown that the optimum (smallest) focus is indeed found in this way.

The converging light passes through a 110 μm thick glass plate (optical microscopy cover slide) and is focused onto the solid target (Fig. 3.13). The glass slide shields the mirror from the debris that is produced in the interaction between the laser pulse and the target material. It appears that the debris ejected from the plasma consists primarily of heavy, molten particles that stick to the first surface they encounter. Blocking the direct paths from the focus to the mirror is therefore sufficient to keep the mirror clean during the experiment. The light transmission of the glass slide diminishes over time because of the debris but the glass plate can be changed remotely.

Target Device

The use of solid or liquid targets provides many options regarding target types. There are two important demands on a target: (1) it must present a fresh target surface for every laser pulse in order to provide identical experimental conditions and (2) it must be accurately positioned in the laser focus, with deviations that are small in relation to the beam confocal parameter. Three main groups of target devices exist: liquid jets,[69] a moving wire,[70,71] or moving solid discs.[27] In the experiments presented here, the confocal parameter is less than 5 μm and metal discs, 50 mm diameter and 2 mm thick, were used as targets. The targets are

welded onto steel bases that fit on an adjustable mount. The use of the set-up in both the ten-hertz laser and the kilohertz laser complicates the design because the target must rotate a hundred times faster in the latter system to provide a fresh surface for each laser pulse (Paper V).

Several different target materials have been used; aluminium (atomic number: Z=13), iron (Z=26), copper (Z=29), tin (Z=50), antimony (Z=51), gadolinium (Z=64), tantalum (Z=73) and lead (Z=82). The relatively high atomic numbers of the targets ensures good Bremsstrahlung efficiency. The targets are turned and carefully polished before use.

The motion of the target is controlled during the experiment and since the target wobbles slightly due to mechanical imperfections, a device constituting a position gauge and a regulated piezo-mount stabilizes it. Using this device, the target can be held in focus within ± 2 μm over a turn. The target is rotated and translated sideways simultaneously in order to position the foci on a line that starts at the edge of the target and spirals inwards to the center. Thus, every laser pulse focuses on a fresh, polished part of the target (Figs 3.14 and 3.15). The proportional integrating differentiating (PID) algorithm that controls the movement of the target allows the foci to be separated by only 30 μm without running the risk of them overlapping. With the laser operating at 1 kHz a target lasts for about 35 minutes with such a separation. The target must then be replaced or repolished. The diameter of the craters made by the kilohertz laser pulses is around 7 μm, ten times smaller than those with pulses from the more energetic ten-hertz laser.[72]

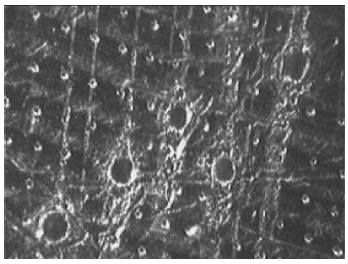

Figure 3.14. *The surface of a tin target after being exposed to laser pulses. The larger craters are the result of focusing several laser pulses onto the same spot. The distance between craters is 50 μm.*

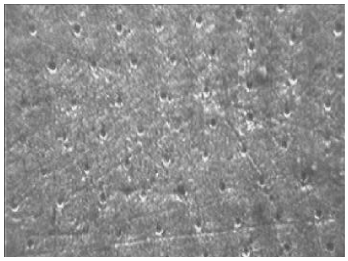

Figure 3.15. *Tantalum is harder and the craters made by the laser pulses are shallower. The higher melting temperature also reduces the amount of debris. The distance between craters is 50 μm.*

Role of Pre-pulses and ASE

Under normal circumstances with a low amount of ASE, the ASE is not measurable with the laser diagnostics employed in the experiments on solid-target focusing (presented in Paper V) for two reasons: (1) tens of nanoseconds before the main pulse the level is too low to be measured (lower than the pre-pulse level) and (2) at zero to three nanoseconds before the main pulse the level cannot be measured due to the limited temporal resolution. It is possible to measure the ASE and pre-pulse levels more accurately with, for example, a streak camera. This was done on the ten-hertz laser (Paper I) because the cluster target used in that experiment is even more sensitive to pre-ionization. The strongest pre-pulse, about ten nanoseconds before the main pulse, is approximately four orders of magnitude weaker than the main pulse. If the pulses are tightly focused as in this experiment, the pre-pulses can ionize the target and generate a pre-plasma. The initial electron density of the pre-plasma depends on the irradiance, but the plasma rapidly expands with approximately the ion sound velocity

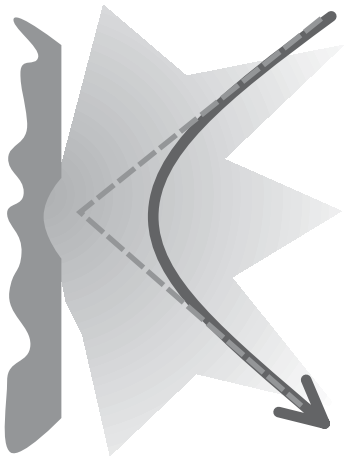

Figure 3.16. *The solid target on the left is first irradiated with a pre-pulse that generates an expanding plasma, (the grey area). The obliquely incident main pulse (black) is continuously refracted and does not reach the highest density region (See also Figure 2.11).*

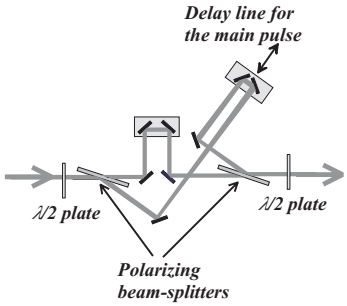

Figure 3.17. *This kind of device is used to produce a double pulse with varying delay and relative energy fractions.*

$v_s \sim 10^4$ m/s (cf. (2.20)). This leads to an exponential-like density distribution, which decreases with the distance from the surface. The exact plasma expansion velocity depends on the mass of the ions, i.e. the target material, and the initial plasma temperature, i.e. the pre-pulses.

Normally, the main laser pulse exhibits temporal "shoulders" with low irradiance that reach out to the picosecond timescale. These shoulders generate a refractive index gradient for the most intense part of the pulse (cf. (2.17)). If the pulse is obliquely incident, it is refracted away before it reaches the critical density (Figs 2.11 and 3.16). This situation is often undesirable because it suppresses some electron heating mechanisms, which require the light to penetrate to the critical density (refer to Section 3.2.2). However, in some experiments a pre-plasma is generated under controlled circumstances. For example, if the main pulse is powerful enough it can undergo relativistic self-focusing (Chapter 4) in the pre-plasma, and therefore penetrate deeper into the plasma.[73,74] In the present experiments, with the expansion speed as above and ten nanoseconds to the strongest pre-pulse, the plasma has sufficient time to expand, but since the pre-pulse irradiance reaches at most $\sim 10^{13}$ W/cm^2 the pre-plasma density is quite low. Therefore, *this* pre-plasma does not prevent the incident main pulse from reaching the high-density regions of the plasma, although the "shoulders" of the main pulse still cause refraction. Several introductory studies have therefore been performed at the Lund High Power Laser Facility with the addition of a strong pre-pulse, employing the device illustrated in Figure 3.17 which splits and recombines laser pulses with arbitrary relative energy fractions and with temporal delays from zero to ten nanoseconds. Stability measurements presented in Section 3.2.4 indicate that the X-ray fluctuation in X-ray yield decreases dramatically with the addition of a strong pre-pulse a few nanosecond before the main pulse. This could be an effect of additional pinching of the laser focus due to an initial stage of relativistic self-focusing, which is discussed in detail in Chapter 4.

Safety Issues

In experiments generating hard X-rays, it is necessary to maintain a high security standard in order to subject the personnel to a minimum of radiation. The evacuated X-ray generation chamber is enclosed in 5 cm lead with openings only for the laser beam and the X-ray paths to the various detectors. Some X-rays that exit the chamber scatter from the surrounding equipment or the detectors and generate a low level of background radiation. This level is too low to be measured due to the always present ambient background in the laboratory building.

The radiation level is monitored in real time with an ion chamber detector (Fig. 3.18) which sets off an alarm if the integrated X-ray dose exceeds a pre-set low limit. The ion chamber detector allows the X-rays to pass into a volume with a constant electric field where they ionize a gas, often air. The current induced is integrated and can be used to calculate the exposure [in Röntgen], the absorbed dose [in Gray] or the equivalent dose [in Sievert]. This detector can only be used to monitor the total yield of X-rays over a period of several seconds, because it is not fast enough to respond to single bursts.

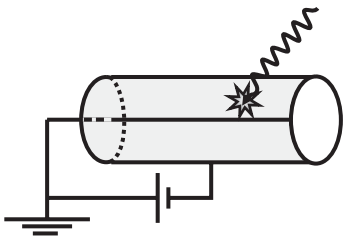

Figure 3.18. *The ion chamber integrates the current induced by ionizing radiation, i.e. X-rays.*

Everyone working in the lab during the X-ray experiments also wears thermoluminescence detectors (TLDs). These give information on the acquired dose on a monthly basis. Generally speaking, the radiation dose is low, even in the direct path of the X-rays a few metres from the chamber, because the low-energy X-rays have been absorbed in air. Closer to the chamber the low-energy photons, which are more prolific, cause the dose rate to increase considerably.

3.2.4 Measurements and Results

Focusing laser pulses onto solid targets provides many options for characterizing the interaction with the gradient density plasma; the approach employed depends on what is being sought. The plasma provides the experimentalist with electromagnetic radiation, from the IR region of the spectrum to hard X-rays and even gamma radiation. Electrons and ions are ejected from the plasma and larger chunks of target (debris) also emerge. Whatever is to be detected, all the detectors must have a "ringside seat" and they should preferably also sample the same solid angle because the emitted may not be isotropic. It is no wonder why much experimental work is concerned with detectors and detection techniques. The experiments presented here have primarily been performed in order to quantify the spectrum of the laser-generated X-rays, particularly with regard to future medical applications.

Visual inspection of the emitted visible light is easily performed by reflecting some light so that it can be seen without standing in the path of the X-rays. The behaviour of the visible light is correlated with the X-ray yield and spectrum, but the colour is different for different target materials. A tantalum plasma, for example, shines blue until the experimental conditions are optimized. With the kilohertz laser pulses the colour then changes to a very bright, fluctuating red, whereas on the ten-hertz laser, the light changes to green. The presence of green light is known from experience to coincide with the emission of energetic X-rays. It is probable that the blue light is some characteristic emission of tantalum, and the reddish, fluctuating light could be relativistically self-phase modulated laser light (cf. Section 4.1.4). The green light, with the exact

frequency $3\omega/2$, is produced by a two-plasmon decay instability in the plasma. This can only occur when the electron density is a quarter of the critical density, allowing the light wave to decay into two counterpropagating electron plasma waves with frequencies $\omega/2$, which heat the plasma.[18] The green light comes from scattering of the laser light at frequency ω from the plasma waves.

The spectrum of X-ray emission is measured in these experiments. Since at least the harder X-rays above a few keV easily propagate through a metre of air and allow for the positioning of detectors further from the plasma, this simplifies the situation a great deal. Still, a severe difficulty in measuring the X-ray spectrum is the short temporal feature of the laser-produced X-rays. In general terms, the detectors convert the energy of the X-ray photons to secondary electrons and the number of electrons produced is counted. The detectors must energy resolve each photon that reaches them in order to reproduce a true Bremsstrahlung spectrum. Even then, the spectrum only represents the small solid angle of the detector. Many groups have studied the X-ray spectrum at different angles and found that both the X-ray spectrum and the irradiance of X-rays are non-isotropic.[75] In addition to the conclusions on spectral features concerning direction, knowledge of the X-ray spectrum, i.e. the Bremsstrahlung distribution, allows conclusions to be drawn regarding the electrons in the plasma.[24,49]

Under controlled experimental conditions and with the help of theoretical simulations, measured X-ray spectra can verify or reject hypotheses, and can be used to improve our understanding of the potential use of laser-produced X-rays in various application. The remaining parts of this section concentrate on the measurements of laser-produced X-rays generated with solid targets in the work at the High Power Laser Facility in Lund.

Spectrally Integrated Measurements

In this work several different scintillation detectors were used for spectrally integrated measurements (the scintillation detector can also be used for single-photon detection). Two photomultiplier tubes (PMTs) coupled to two organic scintillators with slow decay times (several milliseconds) were used to make non-calibrated assessments of the integrated X-ray yield. They were placed close together and one of the scintillators was covered by copper foils. The copper-shielded detector was thus not sensitive to low-energy radiation ($\lesssim 30$ keV). By comparing the signals from the two detectors it was then possible to estimate the ratio of the hard X-rays to the softer ones. With the kilohertz laser system the phosphorescence does not exhibit any time decay between the X-ray bursts, which means that the average X-ray yield was actually measured. Therefore, a sodium-iodide (NaI) detector that could monitor each burst individually was added to the set-up (see Paper V).

An important task in this work was to evaluate the usefulness of the laser-produced X-rays for medical applications. For this purpose a computed radiography (CR) system available at Lund University Hospital was used. The hospital utilizes image plates which are used to directly transfer image data to digital form in a computer system. Image plates are quite different from ordinary radiographic film, because they can be erased and re-used. The active substance is a thin sheath of fragmented colour-centre crystals, which is excited by the X-rays, placing electrons in metastable states in the colour centres. Subsequent pixel-wise readout with a red, focused laser beam scanning the plate produces fluorescence light in an amount that is proportional to the local X-ray exposure. (In Paper V more information on the image plates is given.) Since the image plate response is proportional to the exposure over a wide range (at least 0.01 mR to 10 mR), the digitalized data can be calibrated to the exposure or the absorbed dose provided that the X-ray spectrum is constant. This means of calibration is further discussed in Paper V. C. Olsson at Lund University Hospital has performed a number of measurements in order to investigate whether the calibration is also valid for the laser-produced X-ray spectrum. Measurements with the spectrum of a 140 kV X-ray tube, filtered to increase the average X-ray energy, showed that the calibration underestimated the exposure by a factor of two in an extreme case. The error is not expected to be worse than this when applying the calibration to the image plates recorded with the laser-plasma X-ray spectrum, because the mass energy absorption coefficient for air and the crystals in the image plate is nearly constant from $\sim$ 100 keV to 1 MeV.[76]

In Paper V, the X-ray spectrum of the laser plasma is estimated. Using this spectrum, spectra can be calculated before and after a human body is placed 0.7 m from the plasma (Fig. 3.19). The laser-produced spectrum clearly extends much higher in energy than the spectrum of an ordinary X-ray tube. Note that the filtering before the virtual patient is much too low. A large portion of the spectrum below 20 keV is absorbed in the patient.

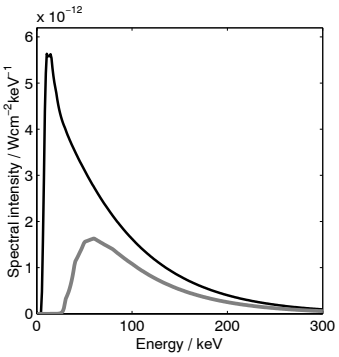

Figure 3.19. *The black trace is the calculated X-ray irradiance 0.7 m from the laser plasma. The grey trace is the previous spectrum as calculated after propagation through 15 cm of standard human soft tissue. The soft radiation should be filtered before the patient in a real situation.*

In Figure 3.20 two image plate recordings are shown with a tantalum target using the kilohertz laser (0.7 mJ per pulse). The images have show scales of the absorbed dose according to the hospital calibration.

Spectrally Resolved Measurements

In the experiments presented here, three different kinds of detectors were used to measure the X-ray spectrum: (1) a (bent) crystal in conjunction with an scintillator-coupled charge-coupled device (CCD), and two types of semiconductor detectors: (2) germanium (Ge) detectors and (3) silicon-based CCDs.

(a) A one-minute exposure of a sacrificed Wistar-Furth rat ($\sim$ 2 cm thick). The grey scale extends from 2 μGy (white) to 13 μGy (black). The image is 20 cm high.

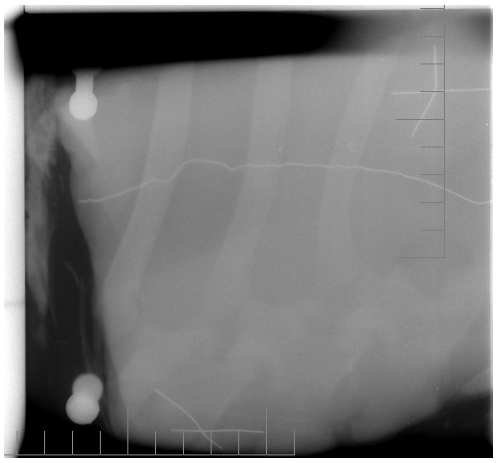

(b) A five-minute exposure of tissue ($\sim$ 7 cm thick) with a platinum wire diagonally through it. The grey scale extends from 2 μGy (white) to 15 μGy (black). The image is 20 cm high.

Figure 3.20. *Image plate recordings using the laser-produced X-rays.*

Semiconductor detectors are suitable for measuring the X-ray spectrum directly, because the X-rays can excite electrons across the well-defined energy band gap. By measuring the total charge obtained when absorbing a single photon in the crystal the photon energy can be deduced. This procedure is referred to as "energy-resolved photon counting". Due to the small band gap of the order of 1 eV, the detectors show exceptionally fine energy resolution, a hundred times better than, for example, a NaI scintillation detector. Most commonly used are silicon- and germanium-based detectors. The latter is mainly used to measure energies above 50 keV because it is about 30 times more efficient than silicon detectors due to its higher atomic number. In the experiments presented here a back-illuminated and thinned silicon-based CCD and two germanium (Ge) detectors were used. These detectors,

and detector-specific results are presented below.

The CCD simultaneously operates a matrix of pixel detectors (512x512) as illustrated in Figure 3.21, whereas a Ge detector resembles a *single* CCD pixel, but it is made from pure, undoped germanium and operates under a high voltage (a few kilovolts). One CCD pixel can typically store $3 \cdot 10^5$ electrons. The whole chip is read out, one pixel at a time, by initiating a read-out cycle with an electronic trigger. However, the active, depleted, region of the thinned* chip is only 10 μm, which means that photons of a few keV easily pass through the detector. This is the main reason why a CCD is limited to measuring X-rays below 20 keV.[77] In this energy domain, however, the CCD is a suitable and user-friendly tool, because it operates over 250 000 separate detectors simultaneously and the calibration of the detector is straightforward. The high brightness of the laser-generated X-rays can thus easily be handled by the CCD, and in most cases it is improbable that two X-rays will be absorbed in the same CCD pixel causing "pile-up", i.e. the addition of photon energies. However, the pile-up effect is a very serious problem for a Ge detector and the two kinds of detectors complement each other, as Ge detectors can measure much higher photon energies.

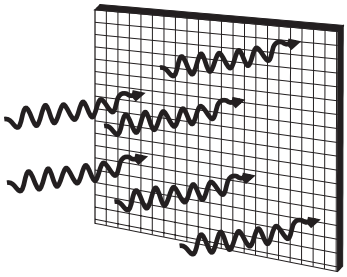

Figure 3.21. *The charge-coupled device (CCD) can detect many X-ray photons simultaneously.*

The CCD used for photon counting in the present work is equipped with analogue-to-digital (AD) converters that produce a fixed 16-bit scale that represents the accumulated charge pixel-wise. The read-out procedure for the chip may thus take as long as one second. Used with the laser-produced X-rays it can detect thousands of events in a single X-ray burst, whereas the Ge detector can detect no more than one event. The X-ray spectrum of the laser-produced X-rays extends up to several hundred keV, which means that most of the photons penetrate the CCD without being absorbed, but they can Compton scatter once or several times in one or several adjacent pixels. Furthermore, if a large portion of the energy is absorbed in the detector, the "charge cloud" will "leak" into adjacent pixels and parts of it will be lost in the parts of the chip surrounding the pixels. Evaluating the CCD involves analysing a number of CCD "images" with distributed events: some single-pixel events and some multiple-pixel events. The procedure for doing this is illustrated in Figure 3.22. There is no "best" way to perform the evaluation; one way is to only count the single-pixel events, as shown in Figures 3.23(a), 3.24(a) and 3.25(a), and another is to count all the events up to a certain size, as shown in Figures 3.23(b), 3.24(b) and 3.25(b). The first approach definitely underestimates the more energetic part of the X-ray spectrum, whereas the latter can erroneously sum adjacent pixels which represent different photons.

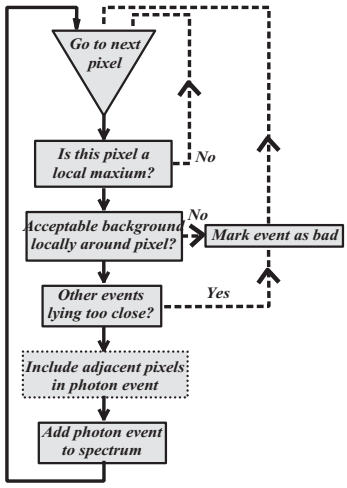

Figure 3.22. *The analysis of the CCD images requires care, especially at X-ray energies above* ~ 10 *keV.*

*The CCD employed for X-ray photon counting has been thinned by removing the section of the chip which is inactive.

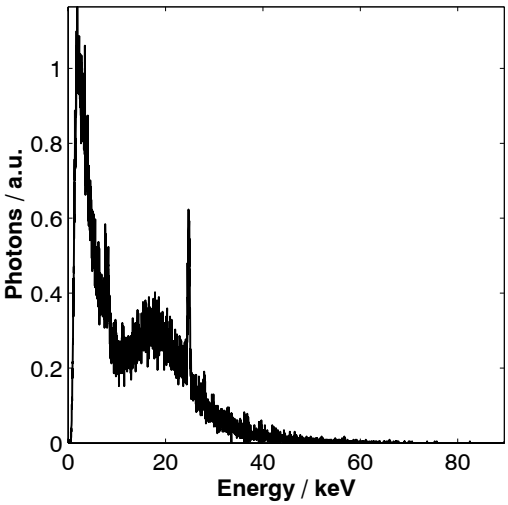

(a) Only single-pixel events.

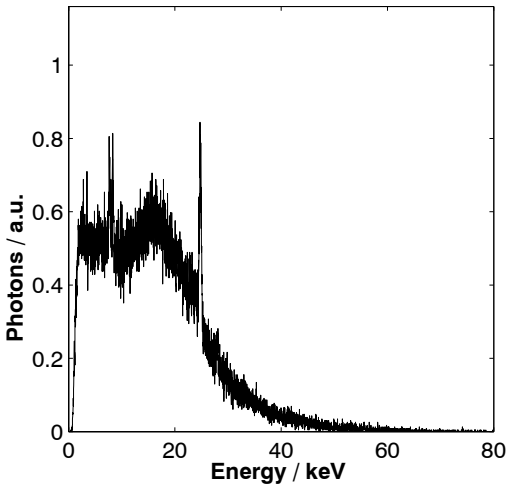

(b) All events counted, including multiple-pixel events up to a maximum of 3x3 pixels.

Figure 3.23. *Data from a back-illuminated CCD when focusing onto a solid tantalum target with the kilohertz laser; 2 mJ and 35 fs in main pulse and 0.2 mJ in a deliberate pre-pulse, 2.4 ns before the main pulse. Both graphs are the result of a set of CCD image data of 230 images, each integrating 2000 laser pulses.*

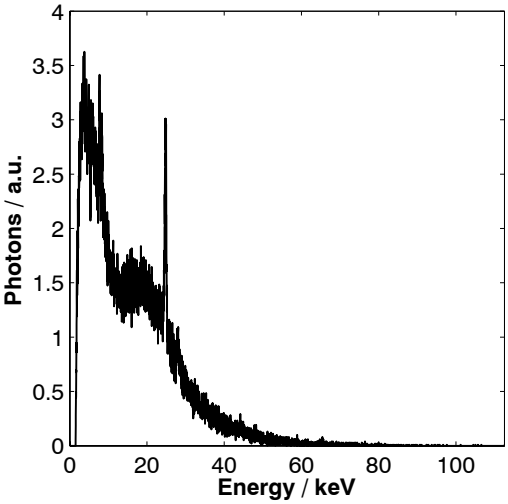

(a) Only single-pixel events.

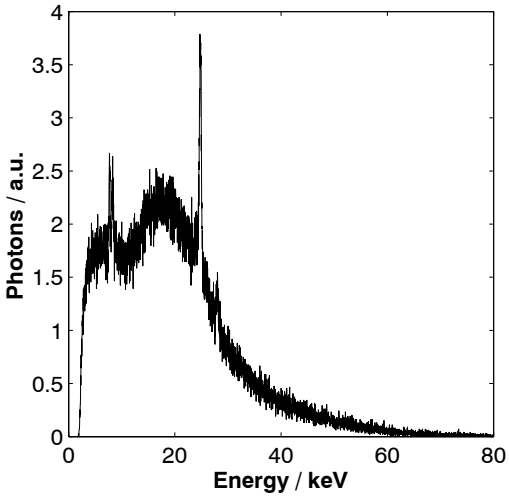

(b) All events counted, including multiple-pixel events up to a maximum of 3x3 pixels.

Figure 3.24. *Data from a back-illuminated CCD when focusing onto a solid tantalum target with the 10 Hz laser; 0.12 J and 500 fs. Both graphs are the result of a set of CCD image data of 99 images, one per laser pulse. The fact that the average X-ray energy is higher than when employing the kilohertz laser can be seen by comparing this figure with Figure 3.23.*

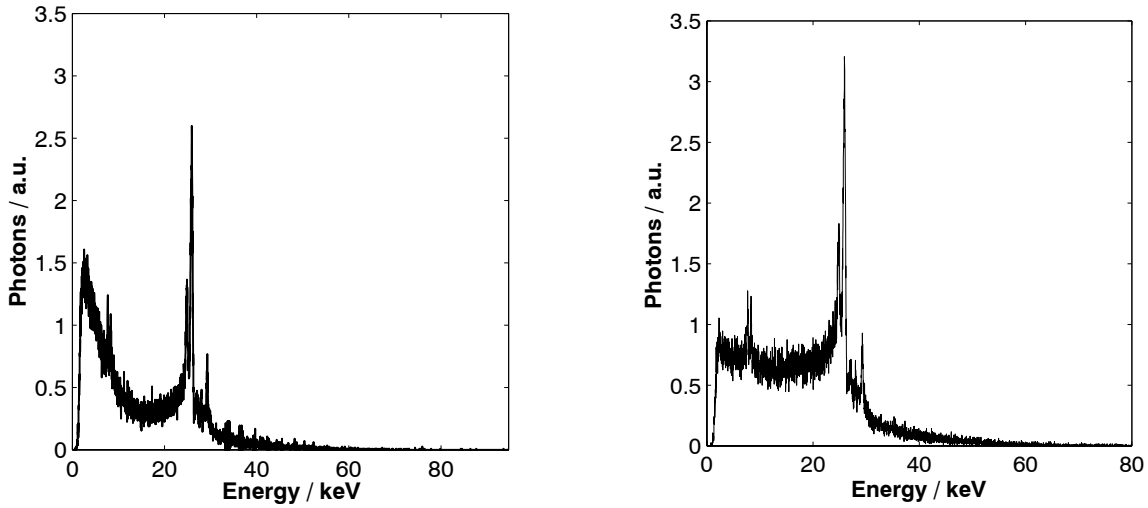

(a) Only single-pixel events.

(b) All events counted, including multiple-pixel events up to a maximum of 3x3 pixels.

Figure 3.25. *Data from a back-illuminated CCD when focusing onto a solid tin target with the 10 Hz laser; 0.12 J and 500 fs. Both graphs are the result of a set of CCD image data of 112 images, one per laser pulse.*

Photon counting with the CCD has additional uncertainties. Due to the finite thickness of the chip, hard X-rays may ionize parts of the CCD chip that are normally beyond the reach of visible light. The spectra in Figures 3.23, 3.24 and 3.25 all exhibit peaks at $\sim$ 24 keV and $\sim$ 27 keV that do not originate from either tantalum or tin (Table 3.2[78]). Figure 3.26 shows a magnified view of a part of the spectra in Figure 3.25, where the additional peaks are very obvious beside the $K\alpha$ and $K\beta$ emission from tin.

The interpretation is that the CCD chip contains indium, which has an atomic number that is one less than tin (Table 3.2). The indium is ionized by the X-rays and subsequently fluoresces with characteristic line emission that can be reabsorbed by the active region of the CCD. In addition to the peaks from indium, Fig-

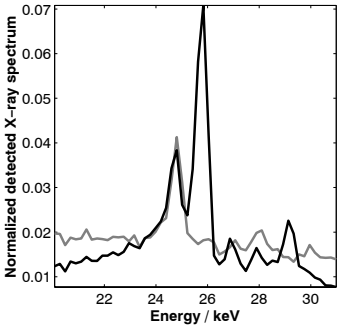

Figure 3.26. *X-ray spectra measured with a thin CCD. The grey spectrum was obtained with a tantalum target, and the black with a tin target. The peaks that are visible in both spectra are characteristic $K\alpha$ and $K\beta$ lines of indium.*

Table 3.2. *Energies of characteristic emissions for a few elements. The energies given are approximate and include several peaks separated in energy by relatively small amounts.*

Element	$K\alpha$ and $K\beta$ / keV	$L\alpha$, $L\beta$ and $L\gamma$ / keV
Ta, $Z = 73$	$\sim$ 57 and 65.2	$\sim$ 8.1, $\sim$ 9.5 and 10.9
In, $Z = 49$	$\sim$ 24 and 27.3	$\sim$ 3.3, $\sim$ 3.6 and 3.9
Sn, $Z = 50$	$\sim$ 25 and 28.5	$\sim$ 3.4, $\sim$ 3.8 and 4.1
Ni, $Z = 28$	7.5 and 8.3	all $\sim$ 0.9
Cu, $Z = 29$	8 and 8.9	all $\sim$ 0.9

ures 3.23, 3.24 and 3.25 exhibit peaks at 7.5 keV and 8 keV. The origin of these peaks is not known, but it may be other elements fluorescing in the CCD chip, such as nickel or copper (Table 3.2). Comparing Figures 3.24 and 3.25, no evidence can be found of the characteristic L radiation from tantalum, which should be found between 8 keV and 11 keV. This is not the case in the data, which means that the efficiency is very low for some reason. The peaks at 7.5 keV and 8 keV, however, are rather intense, indicating that they do not originate from the laser-produced plasma.

However, when used to assess *changes* in the X-ray spectrum with regard to average photon energy and photon number, the results are more reliable. As discussed in Section 3.2.3, a device was employed to generate controllable pre-pulses that generated a pre-plasma on the solid target. Measurements with and without a strong pre-pulse, shown in Figure 3.27, indicate that the X-ray yield and average energy (clearly correlated to each other), fluctuate less when a pre-plasma is generated. Each data point at any particular time, corresponds to a single CCD image. Taking

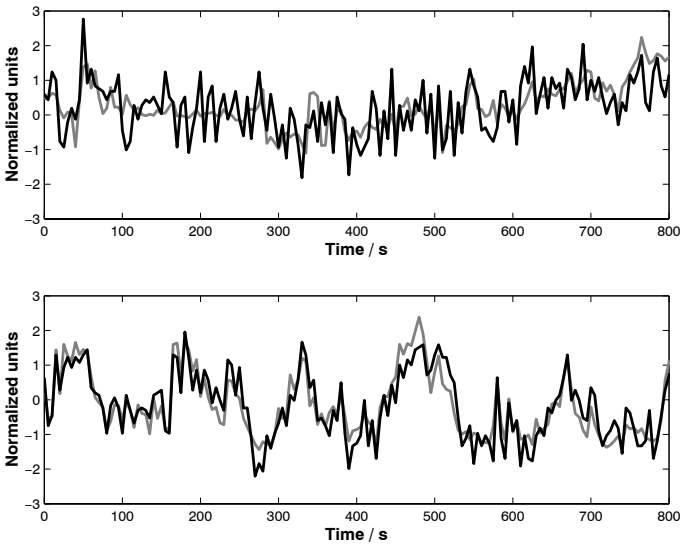

Figure 3.27. *Average photon energy (black) and yield (grey) as detected by a CCD from the kilohertz laser focused onto tantalum. The upper figure shows the fluctuations over time with a 13% pre-pulse (∼ 0.2 mJ), 2.4 ns before the main pulse. The lower figure shows the fluctuations without a deliberate pre-pulse.*

this type of analysis one step further, Figure 3.28 shows a large set of data acquired with the kilohertz laser, with and without strong pre-pulses, and with the ten-hertz laser with two different solid targets. Two conclusions can be drawn from Figure 3.28. First, the addition of a pre-pulse before main pulse of the kilohertz laser increases the average X-ray energy and second, different target materials clearly shift both the average energy and photon number

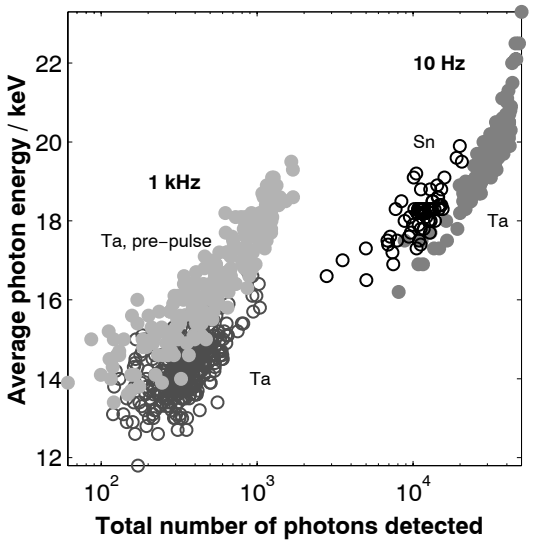

Figure 3.28. *Average photon energy and yield per laser pulse as detected by a CCD using the kilohertz and ten-hertz lasers focused onto tantalum and tin. The irradiance of the deliberate pre-pulse is 13% of the main pulse and 2.4 ns before.*

using the ten-hertz laser. In the latter case, the shift corresponds to the Bremsstrahlung dependence on the atomic number of the target material. Note that the photon number cannot be compared for the kilohertz and ten-hertz laser experiments, because different CCD geometries and image integration times have been used.

Another CCD camera was used to measure the X-ray spectrum, but in a manner completely different from photon counting (Paper II).Here, the X-rays were diffracted on silicon or germanium crystals in Bragg or Laue geometry, and the CCD chip was placed in the direction of the diffracted characteristic emission (Figs 3.29 and 3.30). The CCD camera was equipped with an array of scintillating fibres a few millimetres thick that was mounted on an image intensifier, which in turn was coupled directly to the CCD chip by another set of fibres. Most of the problems associated with CCDs were thus effectively removed, and the energy resolution of the spectrum was determined by the orientation of the diffraction crystal. Only a few spectrally sharp peaks with known energies reached the detector and the comparatively thick array of scintillating fibres converted the X-rays into light flashes while retaining the spatial resolution. The spatial resolution is thus maintained through the image intensifier and onto the chip. With this scintillator-camera device the main difficulty was in calibrating the CCD response to different X-ray photon energies. (Please refer to Paper II for more information on this particular experiment.)

A germanium detector, if used with caution, as described in Pa-

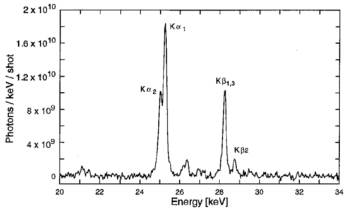

Figure 3.29. *Characteristic X-ray spectrum from tin with the diffracting crystal in Laue geometry.*

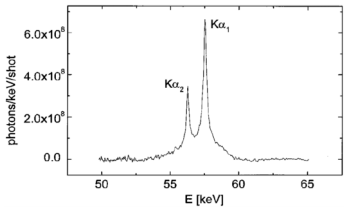

Figure 3.30. *Characteristic X-ray spectrum from tantalum with the diffracting crystal in Bragg geometry.*

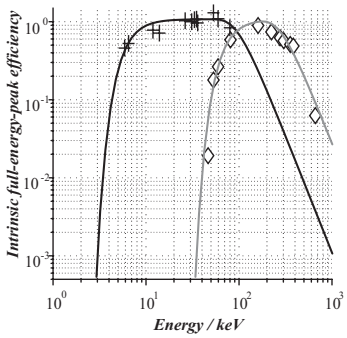

Figure 3.31. *The intrinsic full-energy-peak efficiencies of the two germanium detectors; the LEGe (black) and the HPGe (grey).*

per V, can produce much more reliable data for hard X-rays than a CCD in photon counting mode. In the experiment described in Paper V, two different kinds of Ge detectors were employed: a low-energy germanium (LEGe) detector, which has a 1 cm thick crystal, 2 cm in diameter, and a standard-electrode coaxial germanium (HPGe) detector, which has a crystal more than 5 cm thick† and 5 cm in diameter. The detector performances are listed in Table 3.3 and an efficiency calibration is show in Figure 3.31.

Owing to the different detector designs, they measure different

Table 3.3. *Germanium detector specifications.*

	HPGe	LEGe
Low-energy limit	50 keV	3 keV
High-energy limit	∼10 MeV	∼300 keV
Energy resolution at 5.9 keV	N.A.	170 eV
Energy resolution at 122 keV	∼1 keV	520 eV
Energy resolution at 1332 keV	∼4 keV	N.A.

parts of the laser plasma spectrum (Fig. 3.32). The data shown in the figures are the detector events collected from multichannel analysers (MCAs). In spite of the low-energy detection limits indicated in Table 3.3, the spectra show many detected events below these energies. The origin of these low-energy events is Compton electrons. Despite the fact that the detectors are very effective at absorbing X-ray radiation, some photons are Compton scattered and leave the detectors, producing a Compton electron background at low energies. The fraction of detected events that mirror the true energy of the photon is called the intrinsic full-energy-peak efficiency (see Fig. 3.31).

The Ge detectors should be set up in such a way that they detect, at most, one X-ray photon per X-ray burst. The highest frequency at which the detectors operate is ∼100 kHz at most, i.e. they can detect 100,000 photons per second, but the laser-produced X-rays come in a burst, a few picoseconds short, with a repetition rate determined by the laser. If two or more photons from the same X-ray burst reach the same detector at the same time, their energies will be added. This is called pile-up and its effect on the detected spectrum is analysed in detail in Paper V. One way of minimizing pile-up is to decrease the solid angle subtended by the detectors, by placing them far from the plasma (several metres) behind a small lead aperture. The lead shielding is required anyway, because the detector would otherwise detect background radiation. The effect of pile-up is that the energies of the abundant low-energy photons are added in the detector, effectively redistributing events from the low-energy end to

†The HPGe germanium crystal is U-shaped causing a position dependent thickness.

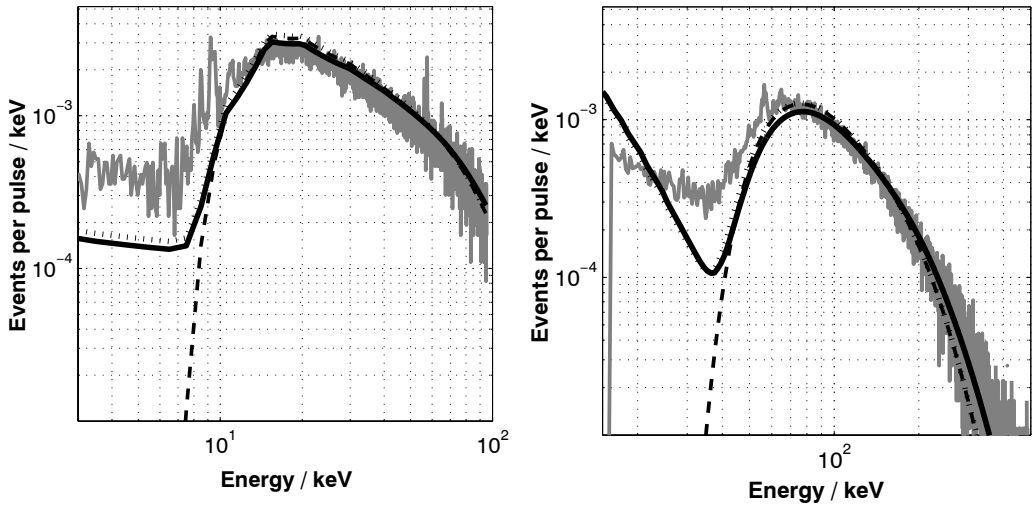

(a) LEGe detector data.

(b) HPGe detector data.

Figure 3.32. *Two experimental X-ray spectra (grey) as they appear in the multichannel analysers. The spectra were recorded simultaneously during 540,000 laser pulses. The laser energy on target was 0.7 mJ with a pulse duration of 25 fs. The other traces are simulated using the model described in Paper V. The black traces should be compared with the experimental data.*

the high-energy end of the spectrum. Even Compton electrons can pile up with photons or other Compton electrons.

In order to identify the pile-up effect experimentally, the Ge detectors were subjected to a very high flux of photons, corresponding to detection probabilities, per laser shot, of more than 50%. The acquired spectra in Figure 3.33 show clear indications of pile-up with the sharp characteristic emission peaks missing. The low-energy parts of the detector spectra are reduced and the high-energy tails are increased. This is easily explained by the piling up in the detector of several low-energy photons, which are recorded as one photon with an energy of the sum of the individual energies. Note, that due to the MCA settings many pile-up events fall outside the energy windows of the MCAs.

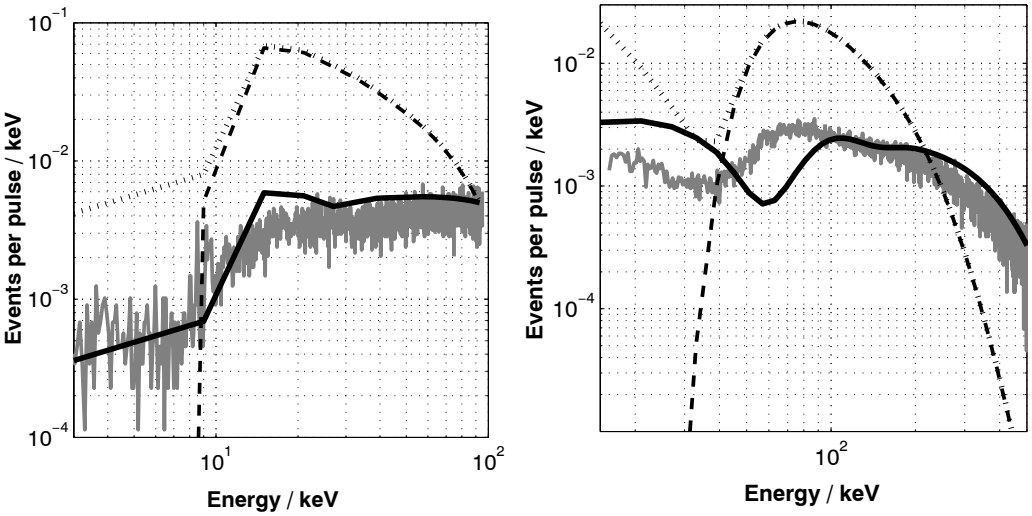

(a) LEGe detector data.

(b) HPGe detector data.

Figure 3.33. *MCA spectra (grey) under extreme conditions with a very high probability of pile-up. The detection probability is higher than 50% per laser shot. Note that the simulation described in Paper V successfully describes even this extreme case of pile-up, here including up to eight-photon pile-up. The black simulated traces should be compared with the experimental data. The other traces represent simulated traces similar to the black trace but with pile-up omitted (· · ·) and additional omission of Compton scattering (−−).*

3.3 X-rays from a Cluster Target

The experiment performed on a clustered gas target shows similarities with both the previously described X-ray generation experiments using solid targets and the gas experiments described in the coming chapter, dealing with relativistic self-focusing. The set-up used for these experiments is similar to the one in Chapter 4, but the outcome is remarkably different: the cluster target responds by emitting quite hard X-rays, up to several keV. Motivation for the cluster experiment can be found in applied X-ray science, one reason being the low quantity of debris produced by this X-ray source. Focusing onto a solid target produces a lot of debris, which prevents the use of that technique in industrial applications, which need "clean" X-ray devices that can operate continuously for long times while producing a constant X-ray flux. A field in which the cluster X-ray source would be of interest is time-resolved X-ray diffraction (an example of this, using a synchrotron X-ray source, is described in Section 3.4). This, however, requires that the duration of the X-ray pulse be sufficiently short to probe atoms in motion; i.e. a timescale of the order of a picosecond. Jörgen Larsson, who is an active researcher in Lund in the

area of time-resolved X-ray diffraction and with experience from the Advanced Light Source (ALS) synchrotron facility in Berkeley, USA,[79,80] coordinated the cluster experiment described below as there was a need to further investigate the temporal aspects of the source and to find out if it is feasible for use as a short-pulse source for X-ray diffraction.

The mechanism that heats electrons in the cluster target is quite different from those in the solid target experiments. Usually, the absorption of light in a gas is low, which speaks against efficient electron heating, but by forming solid or liquid density clusters the light absorption can be increased dramatically, to several percent. This is due to the very different interaction of the laser light with the clusters, particularly clearly demonstrated by Ditmire et al.[81]. They show that if the clusters are pre-ionized by a weak pre-pulse, the outcome of the experiment is high-order harmonics, i.e. a single-atom effect, rather than collective X-ray generation by a plasma. In a cluster experiment the laser pulse is very intense ($> 10^{16}$ W/cm^2) and can quickly ionize the atoms in the clusters. The high-density cluster plasma starts to expand slowly, but if the temperature of the electrons is high enough, they leave the clusters at an early stage, building up a large Coulomb potential that accelerates the ions radially outwards from the clusters. In the Coulomb explosion that follows, rapid collisional heating occurs of both ions and electrons and the hot electrons generate X-rays upon colliding with ions. Since the ions can be efficiently stripped of their electrons in the explosion, the characteristic emission can reach high energies (several keV).

3.3.1 Set-up and Measurement Techniques

The experiment presented here and in Paper I made use of the multi-terawatt arm of the ten-hertz laser and the experimental set-up was similar to that described in Chapter 4. However, the cluster experiment was performed before the evacuated tubing system between the laser pulse compressor and the experiment chamber was installed, and the laser pulses ($\sim$ 0.6 J and 0.1 ps) propagated through air and the windows that comprise the air-vacuum interfaces. The pulses were focused by an $f/1$ off-axis parabolic mirror into a jet of clusters. This subsonic jet was produced by a pulsed valve with a 0.5 mm orifice and a high argon gas backing pressure (80 bar). The clusters form when the gas enters the vacuum and expands, quickly cooling and forming solid argon clusters some distance below the orifice ($\sim$ 1 mm) where the laser pulse is focused.The contrast of the laser output with respect to pre-pulses and ASE was thoroughly investigated because of the sensitivity of the cluster heating; see above. The experimental set-up, shown in Figure 3.34, comprised a streak camera with a cesium-iodide (CsI) cathode for time-resolved detection of X-rays and a CCD camera

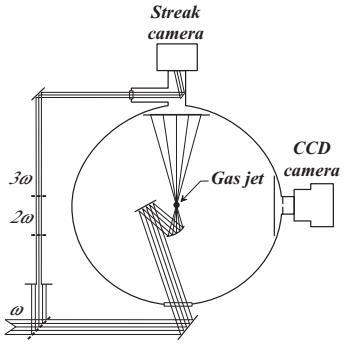

Figure 3.34. *The set-up for generating X-rays from an argon cluster target.*

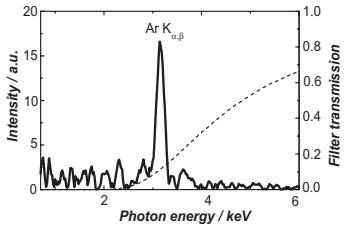

Figure 3.35. *Cluster plasma X-ray spectrum behind filters; 6 μm aluminium and 140 μm plastic. The filter transmission is indicated by the dashed trace.*

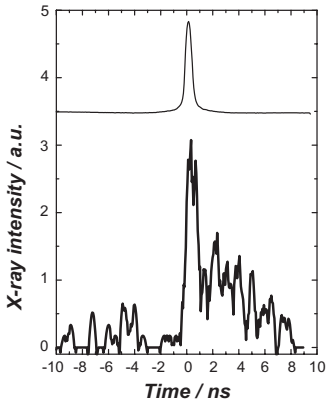

Figure 3.36. *Time-resolved X-ray emission from a cluster plasma using the same filters as in Figure 3.35. The upper trace shows the 3ω timing fiducial.*

used for estimating the cluster size and for photon counting of X-rays from the cluster plasma.

3.3.2 Results and Discussion

First, a low-power laser pulse was used to probe the clusters and Rayleigh-scattered light was detected by the CCD. With knowledge of the gas density in the jet ($\sim 10^{19}$ cm^{-3}), the amount of Rayleigh-scattered light could be used to estimate the size of the clusters, i.e. how many atoms made up a single cluster. With 80 bar backing pressure and a 0.5 mm diameter gas-nozzle orifice it was found that the clusters contained on average 10^5 argon atoms, giving a radius of 15 nm. The laser power was increased and the X-ray spectrum was evaluated by the photon counting technique using the CCD camera. Using a combination of aluminium and plastic filters, the characteristic emission from argon could be isolated (Fig. 3.35). The same filter combination was also used in streak-camera measurements, because the characteristic emission could be expected to show a relatively short temporal duration, much shorter than the general thermal background of the plasma. Figure 3.36 shows the time-resolved characteristic emission with a relatively slow sweep speed in the streak camera (700 ps/mm). The emission exhibits a decay that is of the order of a few nanoseconds. No sharper temporal features could be observed upon increasing the sweep speed to the fastest achieved in this experiment (30 ps/mm). However, since all argon ion charge states emit X-rays, it may be that the different ion species show different temporal characteristics. Thus, the result of the experiment is that the emission seems to have a decay on a nanosecond timescale, but that some highly charged ion species might exhibit a shorter temporal duration.

3.4 Ultra-fast X-ray Probing of Crystals

So far in this chapter, the generation and detection of X-rays have been the main subjects. Using crystals it has been shown that it is possible to measure X-ray spectra, as in Paper II, but in the experiment presented here, X-rays were instead used to probe the crystals, i.e. the other way around. Short, intense bursts of X-rays are generally very useful tools probing fast, microscopic changes in atomic or molecular structures.[80,82–84] In this experiment (Paper VI) acoustic phonons in an InSb crystal were detected with a temporal resolution of only a few picoseconds (cf. Thomsen et al.[85]). The lattice vibrations, i.e. phonons, were generated by a Ti:sapphire laser pulse that was very short in comparison to the inverted phonon frequency. The laser pulse was focused onto the surface of the crystal exciting electrons to the conduction

band. The energy is transferred to the lattice via electron-phonon coupling. The resulting lattice vibrations can be described by a spectrum of coherent acoustic phonons propagating perpendicularly to the crystal surface. The phonon average wavelength is roughly the penetration depth of the laser pulse, i.e. a few tens of nanometres (cf. skin depth). The phonons are said to be coherent because their relative phases are well determined at time zero when the laser pulse excites the crystal and they propagate together as a shock wave through the crystal at the speed of sound. Without the presence of vibrations, diffraction of X-rays follows the well-known Bragg condition,

$$\mathbf{k}_{\text{in}} - \mathbf{k}_{\text{out}} = \mathbf{G}_H \tag{3.5}$$

where $|\mathbf{k}_{\text{in}}| = |\mathbf{k}_{\text{out}}| = \frac{2\pi}{\lambda_0}$ is the wave vector of the X-rays and $|\mathbf{G}_H| = \frac{2\pi}{\lambda_H}$ is the reciprocal vector of the lattice spacing. Since any realistic beam of X-rays has a finite spatial divergence and energy spread, the scattering occurs at a distribution of angles, described by a *rocking curve* (Fig. 3.37). Introducing a phonon of wave vector $|\mathbf{q}| = \frac{2\pi}{\lambda_q}$ into the crystal modifies the Bragg condition and phase matching *also* occurs when

$$\mathbf{k}^*_{\text{in}} - \mathbf{k}^*_{\text{out}} = \mathbf{G}_H \pm \mathbf{q}, \tag{3.6}$$

where $|\mathbf{k}^*_{\text{in}}| = |\mathbf{k}^*_{\text{out}}| = \frac{2\pi}{\lambda^*_0}$ represents X-rays that are not reflected without the presence of the phonon. The situation for X-ray diffraction now becomes much more complicated, because both the wavelength and the amplitude of the phonon affect the rocking curve (Fig. 3.38). According to (3.6) phase matching considerations confer side-bands on the rocking curve, but the temporal oscillation of the vibration adds a temporal oscillation to the side-bands. The relative timing of the phonon initiation by the laser pulse and the X-ray probe arrival at the sample is scanned and the diffraction efficiency can thus be obtained as a function of time.

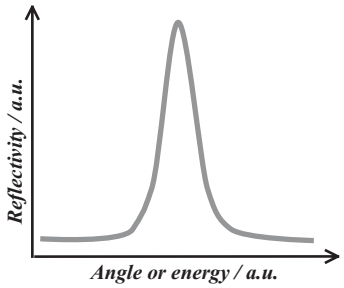

Figure 3.37. *The reflectivity of a crystal for a certain X-ray beam is described by the so-called rocking curve.*

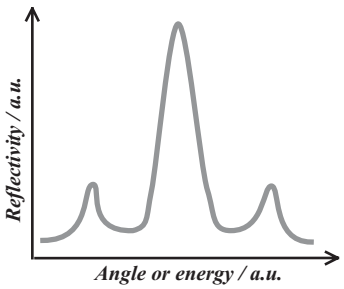

Figure 3.38. *A phonon induces side-bands on the rocking curve.*

3.4.1 Set-up at the ESRF

The experiment was performed at the European Synchrotron Radiation Facility (ESRF) in Grenoble, France, which has several experimental stations around the synchrotron ring. These stations perform differently and are dedicated to different areas of physics, chemistry and biology. The ID-9 station was used for this experiment because it has a Ti:sapphire laser synchronized to the synchrotron ring. The laser operated at about 900 Hz, producing 0.1 ps laser pulses with less than a millijoule per pulse. A single regenerative amplifier was used to amplify the oscillator pulses. The pulses were split into three in this experiment: a pulse at the fundamental frequency (ω) was focused onto the surface of the

InSb crystal, a frequency-tripled pulse (3ω) served as a time reference to the streak camera and the remaining pulse after tripling (ω) was used to trigger the streak camera through a photoconductive switch (Fig. 3.39). The shock wave was initiated at a time

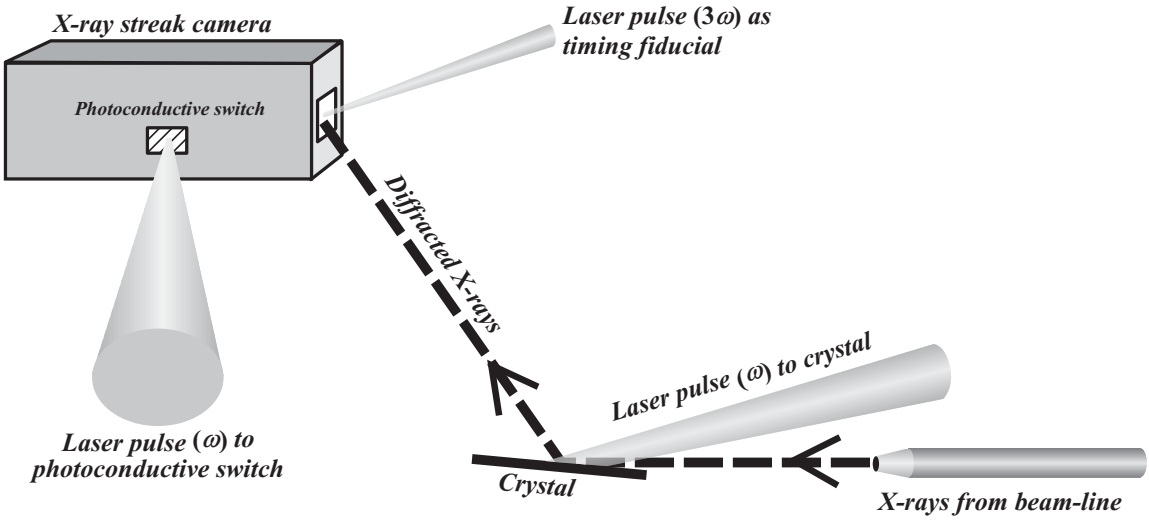

Figure 3.39. *The set-up at the ESRF syncrotron facility for detection of phonons in an InSb crystal.*

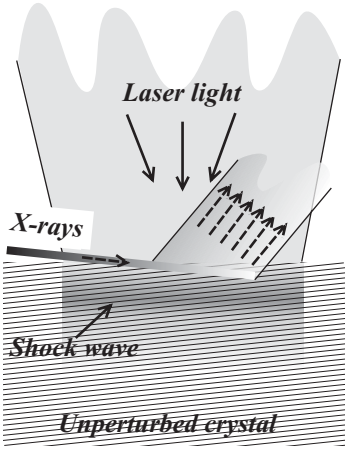

Figure 3.40. *The geometry in the experiment.*

t_0 with the laser pulse, and at a slightly later time, $t_0 + \Delta t$, the X-ray pulse was applied to the crystal in which it scattered, and was detected by the streak camera (Fig. 3.40). The streak-camera position could be considered as fixed, and rather than rotating the crystal to align the diffracted beam on its CsI cathode, the energy of the X-rays was varied. This was possible because the ID-9 station uses a crystal monochromator to select a small portion of the total bandwidth of X-rays produced by an undulator or a wiggler. Therefore, changing the energy required only a slight turning of the monochromator. The X-ray pulses were 85 ps long, and if it were not for the streak camera, the temporal resolution would be limited to this duration. The streak camera in itself, however, had a temporal resolution of less than a picosecond, and the final temporal resolution was independent of the X-ray pulse duration, but depended instead on the streak-camera resolution and the jitter in the timing between the streak camera and the laser system. The jitter was efficiently reduced during the measurements by introducing the 3ω pulse onto the cathode of the streak camera. This timing fiducial mapped out the jitter and could be used to compensate for the jitter in the data analysis. Furthermore, since the relative timing between the laser and the X-ray pulse could be varied with an accuracy much better than the duration of the

X-ray pulse, the effective duration of the X-ray pulse could be as long as desired. Therefore, the temporal oscillations of the sidebands could be mapped out quite well (Paper VI), with a very high sampling rate.

An alternative to the ESRF set-up is to use a very short X-ray pulse to determine the temporal resolution. This can be done, for example, through Thomson scattering from an electron bunch,[86] or by irradiating a thin foil with a short laser pulse (cf. Section 3.2) generating X-ray pulses of a few hundred femtoseconds, i.e. with ten times better temporal resolution than the ESRF experiment.[69,87,88] The short temporal duration when using a thin foil is explained by the fact that accelerated electrons only generate X-rays when they pass through the foil. However, the higher brightness of the synchrotron source makes the process of acquiring data much less time-consuming as long as the phonon oscillation period is long compared with the temporal resolution in the experiment.

3.5 Summary and Outlook

The experiments associated with laser-generated X-rays have dealt with spectral (Papers II and V) and temporal (Paper I) aspects of the X-ray emission from solid or cluster targets.

Regarding measurements of X-ray emission from solid targets, the hot electron spectrum and its corresponding Bremsstrahlung spectrum have been assessed in Paper V and characteristic X-ray emission was also studied (Paper II). Furthermore, it was found that if a controlled pre-pulse was applied to the target the X-ray yield fluctuations could be reduced, and the average X-ray energy increased at the same time.[89] For this purpose, a device was used to delay the main pulse by a few nanoseconds and to generate a pre-pulse containing $\sim 10\%$ of the main pulse. Furthermore, with the higher repetition-rate of the kilohertz laser the laser-produced X-rays are one step further towards realistic use in diagnostic imaging, as discussed in Papers II and V. The kilohertz laser pulses must be temporally short and tightly focused in order to generate X-rays with solid targets. This is in contrast to measurements with the larger ten-hertz laser system at the Lund High Power Laser Facility, with which it is possible to prolong the laser pulse from its shortest duration up to a picosecond while still generating X-rays. It has been found that the target material changes the features of the X-ray spectrum. More practical issues, such as the generation of debris, were also brought up. Most of the experiments have been performed using tantalum as target material, but it is found that changing to tin lowers the amount and average energy of generated X-rays. Thinking in terms of medical applications, the laser-produced X-rays extend to much higher energies than neces-

sary. However, combining an appropriate target material with a high-repetition-rate, high-*average*-power laser system could prove to be the key to future use. Since the short pulse duration of the laser-produced X-rays is of the order of 10 ps, the absorbed dose during diagnostic imaging can be lowered in the future by employing very fast two-dimensional detectors.[35–38,90] The implications of a lowered dose are difficult to evaluate, but it is clear that today, diagnostic imaging leads to detrimental effects caused by the radiation. Therefore, any new device providing lower dose to the patient is desirable. The laser-based X-ray source, in *combination* with time-gated detectors that are being developed, constitutes such a device. The source has an additional advantage, which is the small size of the X-ray source and, furthermore, differential imaging using contrast agents is feasible with this device.

The results in Section 3.3 and Paper I from the time-resolved X-ray measurements using an argon cluster target show that the duration of the characteristic emission from argon is of the order of a nanosecond, which is much too long for use in the kinds of X-ray diffraction experiments that motivated the experiment. However, certain argon charge states may emit radiation on a much shorter timescale. In the experiment presented, the energy resolution was determined by a set of filters, not nearly sharp enough to separate the emission from different charge states. One way to perform an experiment in which this is achieved, would be to use a diffracting crystal in combination with a streak camera. However, as shown in the time-resolved diffraction experiment at the ESRF, the pulse duration of the X-rays does not necessarily limit the temporal resolution.

Ultra-fast processes in crystalline material using short-wavelength X-ray and short-duration laser pulses, have been discussed in Section 3.4 and Paper VI. For this purpose, the X-ray radiation was generated at the ESRF synchrotron facility in Grenoble. In studying the secrets of crystal structures there is sometimes no need for two-dimensional detectors; and, one-dimensional streak cameras are used. Since present streak cameras have a temporal resolution down to 0.5 ps it is possible to use slower X-ray sources, such as synchrotrons, because the resolution is determined by the detector. Thus, users can turn to large synchrotron facilities to perform ultra-fast crystallography experiments. However, it is often difficult to gain access to these facilities, and there is a considerable need for smaller, less costly, but still very bright X-ray sources, such as the laser-based source.

Chapter 4

Relativistic Channelling and Electron Acceleration

In this chapter theory and experiments regarding relativistic channelling of laser pulses in underdense plasmas is presented. Relativistic channelling is a fascinating interdisciplinary subject in the borderland between laser, plasma and particle acceleration physics. The physical mechanism that results in relativistic self-focusing and channelling of the laser pulses is but one of several truly inspiring phenomena that occupy many research groups throughout the world. Recalling the discussion in Section 2.1, the smaller the focus diameter, the shorter the extension of the focus; i.e. the highest irradiance is available only over a very short distance. In this context, relativistic self-focusing supersedes the normal behaviour, enabling extreme irradiances over distances that are not limited by the focal length or beam diameter. The extended focus can be used, for example, to accelerate electrons to very high energies (> 100 MeV) over relatively short distances (~ 1 mm),[74,91–94] or to generate appropriate conditions for X-ray lasing with large gain-length products.[95,96]

The work on relativistic channelling at the Lund High Power Laser Facility is relatively newly started. It began in 1999 with a directed effort to push the limit of the present laser system and to reach a regime where electrons oscillate with relativistic velocities in the laser field, i.e. irradiances above 10^{18} W/cm^2. However, planning started many years earlier and the ten-hertz laser system was upgraded with the new arm for this type of experiments (Section 1.2.1). The character of this kind of experiment is such that it requires not only extreme irradiance, but also an unprecedented level of control over many aspects of the laser system. In particular, the laser upgrade centred on producing smooth irradiance and phase distributions spatially in the amplified pulse, while in-

creasing the power of the pulses, because the laser focus should be nearly diffraction limited. As a consequence of this, extra care must be taken with the alignment of the laser system, as is discussed in Section 1.2.1. With the experimental set-up presented below, using focusing optics with focal length 15 cm, the peak irradiance reaches about $5 \cdot 10^{19}$ W/cm^2, i.e. far into the so-called relativistic regime of laser-matter interactions.

What really happens when relativistic self-focusing sets in is relatively easy to understand figuratively. The laser pulse is focused into a gas, which it ionizes instantaneously. Recall that the plasma frequency (2.16) is related to the electron density and to the mass of the electrons. Also remember that mass is equivalent to energy, such as $m = \gamma m_e = m_e/\sqrt{1-(|\mathbf{v}|/c)^2}$ (γ is the Lorentz factor). Now, if the laser focus shows a peaked and radially symmetric irradiance profile, the plasma electrons will oscillate with different velocities depending on their radial position. Those in the centre of the beam, oscillate with greater amplitude than those at larger radii. If the irradiance is sufficiently high, the mass of the central electrons increases and a peaked electron mass distribution is obtained. From (2.16), it is obvious that the plasma frequency then changes to a valley-shaped distribution (Fig. 4.1) which, in turn, changes the refractive index experienced by the laser pulse (cf. (2.17)), thus bending the phase front of the laser pulse, effectively focusing it. This is relativistic self-focusing. Several theoretical studies of the relativistic self-focusing mechanism point to the need for a minimum, "critical" laser power,[97,98]

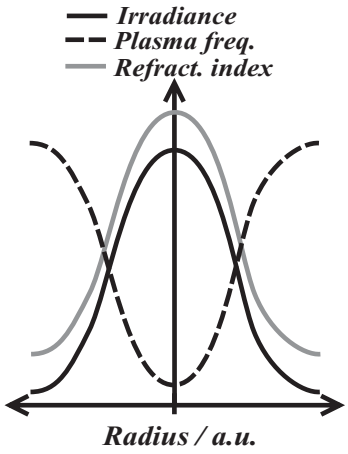

Figure 4.1. *The irradiance changes the plasma frequency, which in turn changes the refractive index, forming a focusing "lens".*

$$P_c\ [\mathrm{GW}] \simeq 17 \left(\frac{\omega}{\omega_{p0}}\right)^2 = \\ = 17\ \frac{n_{c0}}{n_e}, \tag{4.1}$$

required to observe relativistic self-focusing that leads to channelling of the laser pulse. Here, ω_{p0} and ω are the plasma- and laser frequencies ($\langle\gamma\rangle = 1$), and n_e and n_{c0} are the electron density and critical electron density, respectively. There is no mention of high irradiance here, but high irradiance ($\gtrsim 10^{18}$ W/cm^2) is also required to observe strong relativistic effects.[99]

The experiments discussed in this chapter are the first of their kind in this part of Europe, observing and studying the formation of relativistic channels. The chapter first introduces some theory in order to provide a background to the measurement techniques and the results. The experimental set-up is presented in some detail, including the various measurement techniques that were employed. The results of relativistic channelling and electron acceleration studies are then discussed. The chapter ends with a summary and an outlook on future work. The material in this chapter is largely complementary to the contents in Papers III and

IV, and provide a solid background for the relativistic channelling and electron acceleration project at the High Power Laser Facility in Lund.

4.1 Laser Plasma Interactions and Relativistic Channelling: Theory

Several important interactions between a Ti:sapphire laser pulse and an underdense plasma are dealt with here. Apart from relativistic self-focusing and other nonlinear focusing mechanisms, light scattering and relativistic self-phase modulation are introduced. All of these processes are of great importance for the measurements and the results of the research presented later in this chapter and in Papers III and IV.

These are the premises for the following part of this section. A Ti:sapphire laser pulse of peak irradiance I_0, duration $\tau \gg 2\pi/\omega_p$ and wavelength $\lambda = 0.8$ μm is focused into a helium gas jet and there generates, with its leading edge, a plasma of electron density n_e. The initial plasma density does not show a radial variation because the laser pulse is strong enough to completely ionize the helium at an early stage (cf. Section 2.2.1). This means that refraction due to incomplete ionization can be omitted from the analysis.

4.1.1 Relativistic Self-Focusing

Relativistic self-focusing, which may lead to channelling, occurs because the light irradiance forms a radially decreasing refractive index, as illustrated in Figure 4.1. The principle is straightforward, but a closer examination reveals many peculiarities. A self-focusing model is therefore discussed below, taking into account the focusing conditions which are of central importance in real experiments. Thereafter, the critical power is derived through a simplified model. Finally, *filamentation* is presented as an alternative to whole-beam self-focusing.

In a theoretical description of self-focusing, it is found that in addition to the power criteria (4.1), the convergence of the focusing laser pulse as well as the irradiance affect the possibility of forming a light-channel by means of relativistic self-focusing.[100] In this particle-and-potential model the "particle" corresponds to the channel radius and the potential relates to the "forces" that act on the particle due to diffraction (towards larger radii) and relativistic effects (towards smaller radii).[98–103] If the conditions are such that the convergence of the focusing laser pulse is "too large", meaning that the pulse is "over-focused", the pulse focuses and then immediately diverges due to diffraction, as illustrated in Figure 4.2 where the particle rolls into the well and is subse-

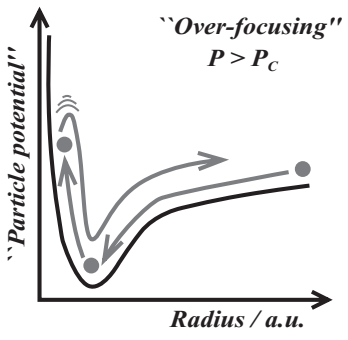

Figure 4.2. *"Over-focusing" the pulse into the gas according to the particle-and-potential analogy by Sprangle et al..*

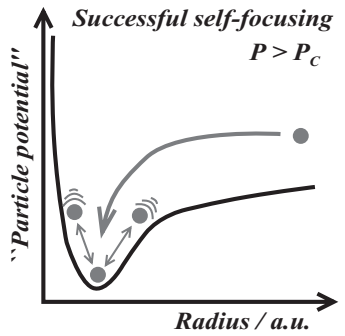

Figure 4.3. *Successful relativistic self-focusing.*

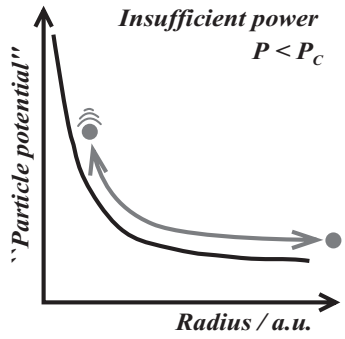

Figure 4.4. *Insufficient power for relativistic self-focusing.*

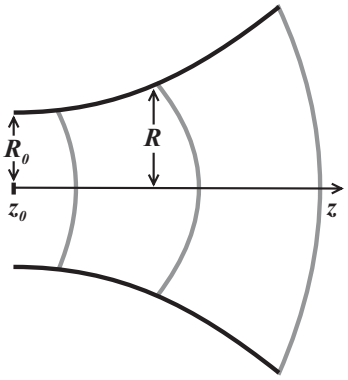

Figure 4.5. *This figure illustrates the situation when diffraction causes the beam to expand.*

quently repelled. However, in the experimental situation for the experiments in this chapter, the laser is focused in vacuum and the light enters the gas or plasma only very close to the point of smallest focus. At this position the convergence is small and overfocusing becomes improbable. In the model there is a "perfect" condition, occurring when a pulse enters the plasma exactly at the bottom of the potential well in Figure 4.2, i.e. with no convergence and with a focus radius determined by the potential minimum. In such a situation diffraction and relativistic self-focusing cancel leading to the formation of a relativistic channel with constant radius. In practice, this is probably not possible. Instead, the pulse, which has a non-optimal radius and convergence enters the plasma and its radius starts to oscillate around the potential minimum as shown in Figure 4.3.[104] This is sometimes referred to as "sausaging", because the channel's longitudinal profile resembles an unevenly stuffed sausage. If the pulse power is lower than the critical power (4.1), there is no potential minimum and the pulse will diverge due to diffraction (Fig. 4.4). Thus, if the power criteria is fulfilled (4.1) the potential exhibits a local minimum (well). The higher the power is, the deeper the well becomes. Furthermore, for higher power, i.e. higher irradiance, the relativistic focusing effect becomes stronger leading to that the bottom of the well moves towards smaller radii. Generally speaking, the size of a relativistic channel is of the order of a few times c/ω_{p0}, i.e. a few micrometres.[105]

It is possible to derive a quite accurate expression for the critical power by considering the situation in the above model for "perfect" conditions, i.e. cancellation of diffraction and relativistic effects. Assume therefore that the laser pulse traverses the plasma in a gaussian channel of constant radius, R_0 $(1/e^2)$. In every point along the axis of propagation, z_0, diffraction tries to increase the radius of the channel according to,

$$R(z) = R_0\sqrt{1+\left(\frac{z-z_0}{Z_R}\right)^2}, \tag{4.2}$$

where $R(z)$ is the local beam radius, R_0 the radius of the channel at $z = z_0$ and $Z_R = R_0^2\omega/2c$ the Rayleigh range (half the confocal parameter in (2.7)). This expression for the evolution of the channel radius due to diffraction is, in other words, the same as the one for the evolution of a gaussian beam.[6] In the point z_0, the diffraction imposes a beam curvature determined by (Fig. 4.5):

$$\frac{d^2R(z=z_0)}{dz^2} \simeq \frac{R_0}{Z_R^2} = \frac{4c^2}{\omega^2 R_0^3}. \tag{4.3}$$

However, at the same time the increasing mass of the electrons causes a "relativistic lens" that counteracts diffraction. The lensing arises from the radially varying phase velocity, which can be

derived from (2.2), (2.14) and (2.17). Making a first-order approximation in irradiance, the expression for the phase velocity becomes,

$$v_p(R) = \frac{c}{n\,(\omega, R)} \simeq c\left[1 + \frac{1}{2}\frac{\omega_{p0}^2}{\omega^2}\frac{1}{\langle\gamma\rangle(R)}\right] \simeq \overset{\langle\gamma\rangle\ll 2}{\simeq} c\left[1 + \frac{1}{2}\frac{\omega_{p0}^2}{\omega^2}\left[1 - (\langle\gamma\rangle(R) - 1)\right]\right], \tag{4.4}$$

where (2.14) can be used to find approximate values of $\langle\gamma\rangle - 1$. The relativistic effects generate a beam curvature, as illustrated in Figure 4.6, which can be estimated by:

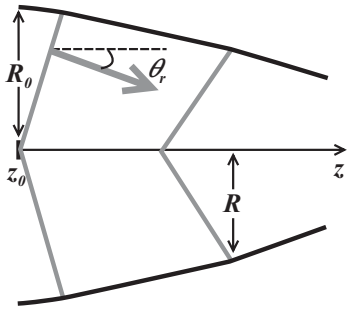

Figure 4.6. *This figure illustrates the situation when relativistic effects pinches the beam.*

$$\frac{d^2R(z=z_0)}{dz^2} \simeq -\frac{d\theta_r}{dz} \simeq \frac{(v_p(R=R_0) - v_p(R=0))}{R_0}\frac{1}{c} \simeq -\frac{1}{2R_0}\frac{\omega_{p0}^2}{\omega^2}\left[\langle\gamma\rangle(R=0) - 1\right] \simeq \overset{(2.14)}{\simeq} -\frac{e^2}{4\varepsilon_0 m_e^2 c^3 \omega^2}\left(\frac{\omega_{p0}}{\omega}\right)\frac{I_0}{R_0} \tag{4.5}$$

because $v_p(R_0) \simeq \lim_{R\to\infty} v_p(R)$ in this approximation when $\langle\gamma\rangle \ll 2$. In the last step above the expression for $\langle\gamma\rangle - 1$ in (2.14) is used as an approximation for the Lorentz factor at the peak irradiance of the laser pulse at $R = 0$. The relativistic effects and diffraction cancel when $d^2R/dz^2\big|_{\text{total}} = 0$. Using the relation $P = I_0\pi R_0^2/2$ for a gaussian beam with $1/e^2$-radius R_0,[6] this equality produces a surprisingly accurate estimate of the critical power:

$$P_C = \frac{8\pi\varepsilon_0 m^2 c^5}{e^2}\left(\frac{\omega}{\omega_{p0}}\right)^2 \simeq 17.4\left(\frac{\omega}{\omega_{p0}}\right)^2 \text{[GW]}. \tag{4.6}$$

Table 4.1 lists the critical power for different plasma densities. With the maximum power produced by the multi-terawatt laser arm at the High Power Laser Facility in Lund, self-focusing can occur in a rather low-density plasma with 10^{18} electrons per cm^3.

Table 4.1. *Critical powers for a 0.8 μm wavelength laser.*

Plasma Density / cm^{-3}	Critical Power / TW
10^{18}	30
10^{19}	3
10^{20}	0.3

It is well known that pulse propagation in the plasma may lead to *filamentation* of the beam into a set of co-propagating filaments of relatively high irradiance. This occurs primarily if the spatial

irradiance distribution of the pulse is structured or if the plasma density varies locally. The mechanisms that govern the propagation of filaments is the same as for whole-beam self-focusing, but since the pulse is split, the peak power of the filaments is lower. The size of the relativistic channel, or individual filaments is very small (a few microns), which means that it is difficult to distinguish between filamentation and whole-beam self-focusing in experiments.

4.1.2 Other Contributions to Self-Focusing

Apparently, in order for self-focusing or filamentation to occur, a focusing refractive index gradient must be induced in the plasma. In other words, the plasma resonance frequency must take on a radial variation; lowest at the centre of the laser beam, or laser beam filament, and increasing outwards. Apart from the relativistic effects described above, the more fundamental ponderomotive pressure pushes electron from the regions of highest irradiance, inducing a radially varying electron density, n_e, and thus producing a focusing effect (cf. (2.17)). Whereas relativistic self-focusing is very rapid, working over only a few optical cycles, the ponderomotive self-focusing force, coming into effect through plasma *cavitation*, requires the electrons to move from the focus radially outwards. Therefore, the longer the duration of the pulse, the more effectively it cavitates the focus. If cavitation is included in the model for self-focusing, the effective critical power decreases.[99] In the experiments on relativistic self-focusing presented in this chapter, the laser pulse duration is often varied in order to study various mechanisms, and with longer pulse durations, it is possible that electron cavitation causes a greater focusing effect for the trailing part of the pulse. Furthermore, as the the electrons leave the channel, the relativistic effects decrease, leading to a growth of the channel radius.

It is also possible for ions to be expelled from the channel by the ponderomotive pressure, but on a significantly longer timescale of a few hundred femtoseconds ($I \geqslant 10^{18}$ W/cm^2).[104,106,107] In the experiments presented in this chapter, the laser pulses are sometimes as long as 0.5 ps and, during this time, the ions have time to move outwards and cavitate the channel further. Figure 2.18 shows that the plasma channel diameter continues to increase at approximately the ion acoustic velocity after the short pulse has passed.[108,109] However, if many electrons have been expelled from the centre of the channel, the resulting positively charged channel makes the ions accelerate radially and shoot out in a Coulomb explosion.

4.1.3 Light Scattering

The relativistic self-focusing experiments in Lund are very dependent upon the *Raman* and *Thomson* light scattering processes. For example, the lengths of the channels, discussed in Section 4.3.1, Papers III and IV, are measured by detecting Thomson-scattered light at 90° to the propagation axis. Raman scattering is a mixing process of the laser light wave with plasma waves that can modulate the laser pulse and increase the amplitude of the plasma waves that co-propagate with the laser pulse causing, for example, electron acceleration in the forward direction. Thomson scattering is the scattering of light from free electrons in the plasma that are accelerated in the light field. Both processes may be phase-matched over long distances and reach high scattering efficiencies. In the experiments presented in this chapter, Thomson scattering is important as a diagnostic tool for the light-plasma interaction. Raman scattered light can also be used to diagnose the plasma, e.g. the electron density, as discussed in Section 4.2.2, but it is primarily important as a process that excites plasma waves, often in an unstable, increasing manner through the *Raman instability*.[8,110,111] The plasma waves in turn generate accelerated electrons. The theory of electron acceleration is discussed in Section 4.1.5 and measurements of such electrons are presented in Section 4.3.2.

Thomson Scattering

Thomson scattering can be divided into two kinds; coherent (phase-matched) and incoherent (non-phase-matched).[112] The basic principle is simple: when a charged particle accelerates it emits electromagnetic radiation. In the polarized laser field the electrons oscillate in mainly one direction, along the polarization axis, and emit light in all directions but this. Thus, in the classical description used here, every oscillating electron generates its own electromagnetic wavelet with the same frequency as the laser, which then interferes with the other wavelets. It is easy to see that the wavelets interfere constructively in the propagation direction of the laser pulse. This is called *coherent Thomson scattering* and the amount of light is proportional to the square of the electron density. The interference becomes more and more destructive at larger angles to the propagation direction, generating *incoherent Thomson scattering*, the strength of which is proportional to the electron density. However, in for example a relativistic channel of very small diameter, it could be possible to observe coherent Thomson radiation at 90° because the destructive interference would occur over such short a distance that it would not completely scramble the coherence.

When Thomson-scattered light is imaged perpendicularly to

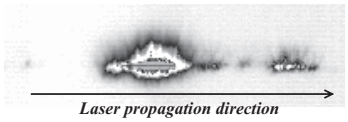

Figure 4.7. *A relativistic channel imaged by recording the Thomson scattered light.*

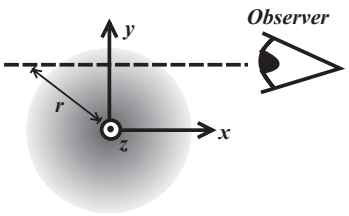

Figure 4.8. *Incoherent Thomson scattering along the dashed trace from a cylindrically symmetric light channel, to the observer.*

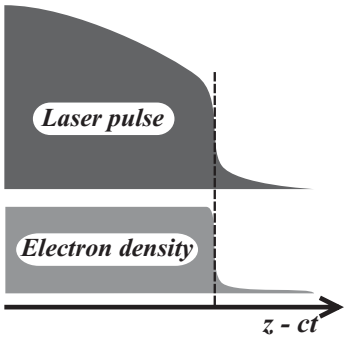

Figure 4.9. *The intense pulse rapidly ionizes the gas and forms a step-like electron density. The pulse envelope steepens as a result of this and relativistically induced GVD.*

the direction of pulse propagation in order to determine the length of the relativistic channel, it is important to be able to interpret the images. Take the image in Figure 4.7 as an example. The scattered light indicates that the laser pulse is confined to a channel, but the Thomson-scattered light is modulated along the direction of the channel. The yield of incoherent Thomson-scattered light from a radially symmetric emitter, i.e. the channel, along a direction x, is,[104,113]

$$\eta_{Thomson}(y,z) \propto \int \frac{n_e(r,z)}{\langle\gamma(r,z)\rangle^2} I(r,z)dx, \tag{4.7}$$

where x, y, z and r are defined in Figure 4.8, $\langle\gamma\rangle$ is the averaged Lorentz factor and I is the irradiance. Thus, the yield of Thomson-scattered light is proportional to the local irradiance, local electron density and the local electron velocity. It is not surprising then that the scattered light exhibits modulation along z caused by electron cavitation (Section 4.1.2) and channel sausaging (Section 4.1.1). If, for some reason, the neutral gas jet exhibits a modulated density, that also appears as a modulation of the Thomson-scattering irradiance.

Raman Scattering

Raman scattering is an essential process in forming behind the laser pulse a trailing electrostatic plasma wave, i.e. the "wake", because it effectively transfers energy from the laser pulse to to plasma wave. For a number of reasons, Raman forward scattering (RFS) often grows in an unstable manner, causing energy transfer from the light pulse to a plasma wave, and modulation of the light pulse that leads to the generation of light "bunches" separated by the wavelength of the plasma wave. A full description of Raman instability is very difficult. Here, the process is described mainly in a one-dimensional perspective, excluding the interactions with competing instabilities such as self-focusing and self-phase modulation.[114–116] This is motivated because the extension of the channel is much longer than its radius (see, e.g. Section 4.3.1, Papers III and IV), which means that the RFS instability is most efficient along the extension of the channel, i.e. in one dimension.

Consider a laser pulse that is focused into a gas jet, quickly ionizing the gas (cf. Section 2.2.1), forming a co-propagating, step-like electron density gradient as the ionization to helium 2+ occurs at a very high rate as soon as the irradiance exceeds $\sim 10^{16}$ W/cm^2. This is illustrated in Figure 4.9. In the process of ionization, the pulse front steepens,[8] because the group velocity is lower in the plasma than in the gas. Furthermore, relativistic effects in the plasma that is continuously generated act to steepen the pulse front. The average quiver velocities of the electrons increase when the pulse envelope overtakes them, causing a steadily increasing group velocity towards the peak of the pulse, thus reinforcing the

steepening. The newly ionized electrons are thus pushed by an enhanced ponderomotive force, because the gradient of the pulse envelope is substantially larger due to steepening. The electrons also gain momentum along the axis of propagation at the instant of ionization,[8] and together these forces initiate a plasma wave propagating with the laser pulse group velocity. This plasma wave acts as a seed for the Raman forward scattering instability. However, before the RFS instability has time to grow *Raman backscattering* (RBS) generates a slow plasma wave that quickly collapses through wave breaking (as discussed in Section 4.1.5) and provides an environment in which the RFS plasma wave can grow.[8] RBS grows very quick because the oscillating magnetic field of the laser pulse moves electrons according to the "$\mathbf{v}\times\mathbf{B}$"-term of the Lorentz force (2.8), and thus immediately seeds the plasma wave needed for RBS before the slower ponderomotive pressure generates a wave leading to RFS instability.

Now that the main mechanisms that seed RFS instability have been presented, the instability itself can be explained. RFS instability is actually very similar to RBS, but it can grow more easily to large proportions because both the scattered optical wave and the plasma wave co-propagate with the laser pulse. The plasma wave also propagates at almost the laser pulse group velocity, which means that the wave can accelerate electrons to very high velocities (see Section 4.1.5). The Stokes frequency component of the RFS light is generally stronger than the anti-Stokes component, because the latter takes energy *from* the plasma wave, thus effectively quenching itself. Only if a major part of the light down-shifts to the Stokes component can the anti-Stokes component grow at the cost of the former.[111,117,118] RFS involves scattering of the light wave (ω, k) from a plasma wave of frequency ω_{ek}, defined in (2.21), and wave vector $k_p = k - k_{\mathrm{S,f}}$ (Fig. 4.10), where $k_{\mathrm{S,f}}$ is the wavevector of the Stokes component;

$$\begin{aligned} \omega_{\mathrm{S,f}} &= \omega - \omega_{ek}, \\ k_{\mathrm{S,f}} &= k - k_p. \end{aligned} \tag{4.8}$$

Thus, Figure 4.10 shows the simultaneous matching in *one dimension* of wave vectors and frequencies as expressed by (4.8). In the simplified model of a plasma with zero thermal temperature ($\omega_{ek} = \omega_p$), these conditions are automatically met because the wave vector of the plasma wave can take any value. However, in some cases the appropriate plasma wave cannot form efficiently, for example, if the channel is depleted of electrons or if the plasma temperature is very high (several keV). In Figure 4.10 a higher plasma temperature manifests itself in a more pronounced parabolic shape of the plasma wave dispersion curve (see Section 2.2 for details), which prevents perfect phase matching. From (4.8) it is clear that the light shifted to lower frequency in the

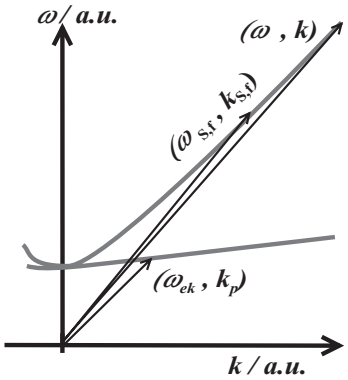

Figure 4.10. *One-dimensional frequency and wave vector matching of the waves involved in RFS instability. The dispersion curves for plasma and light waves are indicated by the grey traces (see also Section 2.2).*

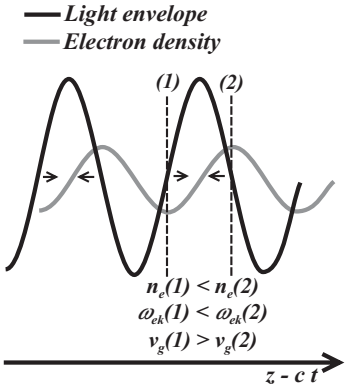

Figure 4.11. *The light pulse is modulated because of RFS and the varying group velocity "bunches" the light further. The arrows indicate relative movement.*

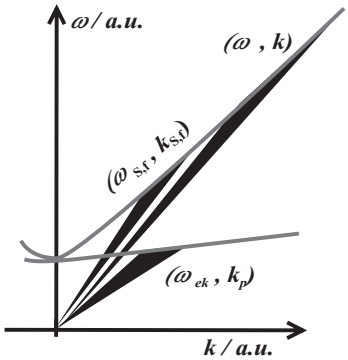

Figure 4.12. *A pulse with large bandwidth can support a spectrum of plasma waves.*

Stokes component contains information about the plasma density and perhaps also the average mass increase of the electrons, because $\omega_{ek} \sim \sqrt{n_e/\langle\gamma\rangle}$. It could also possibly provide insight in the temperature of the electrons in the channel as can be seen in (2.21). In Section 4.2.2 the possibility of estimating n_e (and $\langle\gamma\rangle$) by measuring the Stokes frequency is discussed.

The laser pulse becomes modulated by the Stokes light and an interference beat-wave forms with a frequency that corresponds exactly to the plasma frequency, ω_{ek}. This wave in turn acts with a modulated ponderomotive force on the plasma wave, driving it to higher amplitudes, and the more pronounced the plasma wave becomes, the more light it scatters. This is the RFS instability.

The group velocity of the laser pulse is expressed by (2.4), (2.17) and (2.21),

$$v_g \simeq c\left[1 - \frac{1}{2}\frac{\omega_{ek}^2}{\omega^2}\right], \tag{4.9}$$

which means that the local group velocity is a function of the local electron density ($\omega_{ek} \propto \sqrt{n_e}$). This reinforces the pulse modulation and bunches the light into equidistant "pulses", separated by $\sim \lambda_p$ (Fig. 4.11). However, there is a limit to this.

If the bandwidth of the laser pulse is large,[110] a whole spectrum of plasma waves is generated simultaneously (Fig. 4.12), which makes the RFS instability even more sensitive to high plasma temperatures. Even with a low temperature, the waves may interfere destructively and lower the amplitude of the resulting plasma wave.

The multi-terawatt arm used in the Lund High Power Laser Facility experiments provides pulses as short as 30 fs, which means that the spectrum is roughly 15 THz wide, i.e. about a tenth of the lowest plasma frequency used in the experiments and this might affect the RFS instability negatively. However, the pulse duration is changed by varying the chirp and this probably affects the interaction more because, in contrast to the bandwidth limitation, it is possible to use a broad laser pulse bandwidth to *increase* the Raman efficiency.[119,120] Consider, for example, a laser pulse from the multi-terawatt arm with a positive chirp, i.e. the frequency increases from the front to the tail. Such a pulse transfers its chirp to the plasma wave and generates a progressively *faster* plasma wave (Fig. 4.13), which contracts the wave packet. This effect is perhaps more clearly visible in Figure 4.14, where the group velocity can be seen to contract the whole wave packet for the positively chirped pulse. A pulse with negative chirp works against the RFS instability and if the bandwidth is large enough, the chirp can, to a large extent, remove the RFS instability.[110]

Summarizing so far, RFS instability generates a modulated pulse which resonantly drives the plasma wave that forms the wake of the laser pulse more efficiently.[121,122] Since electrons can "surf" the high amplitude wake (see Section 4.1.5), RFS instability is par-

ticularly important in particle acceleration schemes. Since future experiments at the Lund High Power Laser Facility are aimed at studying the energies as well as the number of accelerated electrons using chirped laser pulses, the impact of RFS instability is important. Note that the efficiency of the instability is expected to decrease dramatically as the pulse duration decreases and approaches the plasma oscillation period, because in this regime, the laser pulse cannot interact efficiently with the plasma wave.[106]

Before leaving the subject of Raman scattering, the reasoning will be extended to three dimensions. Raman scattering from a finite laser focus is different from the one-dimensional approach and it is better suited to the conditions usually encountered in the experiments presented in this chapter. Eq. (4.8) expresses the condition for Raman forward scattering in one dimension. However, since the wave vector of the plasma wave can take *any* value, it is also possible to realize Raman scattering in the geometry indicated in Figure. 4.15, i.e. at an angle θ to the light propagation axis. In the laser focus, Raman scattering occurs at all angles, θ, but as the angle increases the interaction length decreases and the *amount* of Raman-scattered light therefore decreases (Fig. 4.16(a)). Note that the Raman-scattered light is emitted in a larger cone than the laser light, due to the phase matching indicated in Figure 4.15. In the extreme case of a channelled laser pulse, the length of the focus is many times greater than its radius and the irradiance of the Raman-scattered light is therefore much greater in the near-forward direction (Fig. 4.16(b)). However, by collecting the forward-scattered light at relatively large angles, the ratio of Raman-scattered light to fundamental laser light increases, which can be useful when the Raman signal is weak or when the fundamental laser light is very strong. In the Lund experiments, the light in a large cone is collected with a lens and the fundamental light is filtered out from the beam with a dielectric mirror (see Section 4.2.2). In this way a strong Raman signal is achieved.

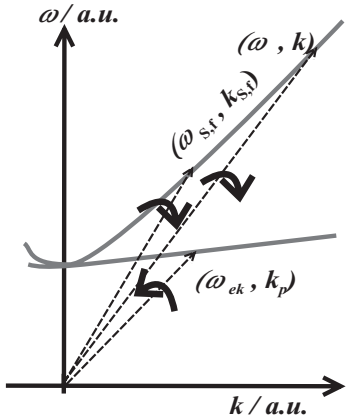

Figure 4.13. *A positively chirped pulse progressively generates a faster plasma wave, i.e. ω_p/k_p increases.*

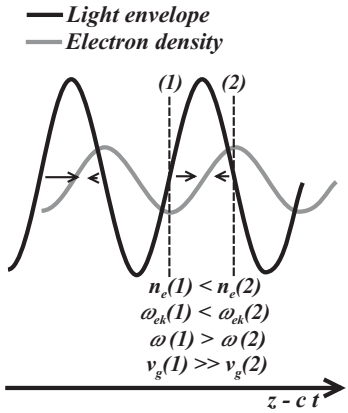

Figure 4.14. *A pulse with large bandwidth with positive chirp can reinforce the light bunching. Note the size of the arrows, indicating not only bunching, but also compression of the whole pulse.*

4.1.4 Relativistically Induced Self-Phase Modulation

Self-phase modulation is in general a nonlinear process that occurs when the refractive index varies with the light irradiance (cf. Section 2.1). In a plasma, the irradiance dependence, at relativistic irradiances, enters through the plasma frequency (2.16).[115] Differentiating the refractive index (2.17) produces a similar expression for the nonlinearity to (2.5). The effect can be stronger than self-phase modulation in for example air, causing a laser pulse to acquire a chirp that is most obvious at the flanks of the pulse where the irradiance gradient is large. In order to see the effect of this self-phase modulation, the chirp from self-phase modulation has been added to unchirped laser pulses in Figure 4.16. Note that

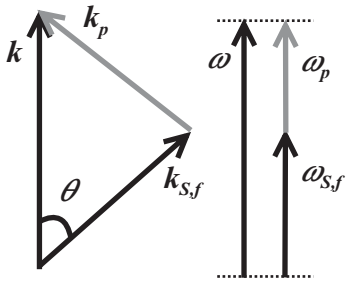

Figure 4.15. *Wave vector matching in three dimensions.*

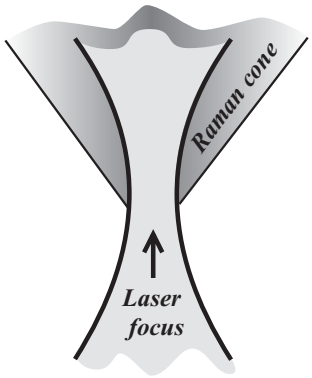

(a) A cone of Raman-scattered light from a focus.

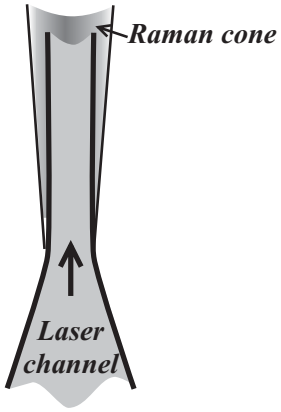

(b) A cone of Raman-scattered light from a narrow channel.

the pulse has not been propagated through the plasma in the true sense of the word, the chirp has merely been added to the pulse without taking into account other effects, such as GVD. The very large wavelength shifts indicate that the effects can be dramatic in a real experiment. Relativistic self-phase modulation (RSPM) can cause severe spectral broadening that makes all kinds of spectroscopy difficult. The Raman-scattered light, for example, has been seen to completely disappear in the high background generated by RSPM when trying to measure the electron density with a high laser power.

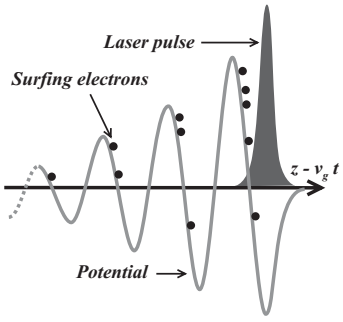

Figure 4.17. *The plasma wake in the short-pulse regime ($\tau \leqslant \pi/\omega_p$).*

4.1.5 Particle Acceleration Mechanisms

In order to accelerate electrons to high energies, the obvious thing to do is to provide as high an amplitude of the plasma waves as possible. If the laser pulse duration is shorter than half the plasma period, the pulse excites a trailing plasma wave ("wake"), which is illustrated in Figure 4.17.

Acceleration by Plasma Waves

The condition for relativistic self-focusing in (4.1) together with the condition that $\tau \leqslant \pi/\omega_p$, makes it difficult to reach this short-pulse regime, because the necessary pulse energy scales as $1/\omega_p^3$. The plasma frequency is determined by the electron density that can be produced, and for a reasonable laser pulse with a duration of 50 fs, the electron density should be lower than $3 \cdot 10^{18}$ cm^{-3} to reach the short-pulse regime, which through (4.1) translates

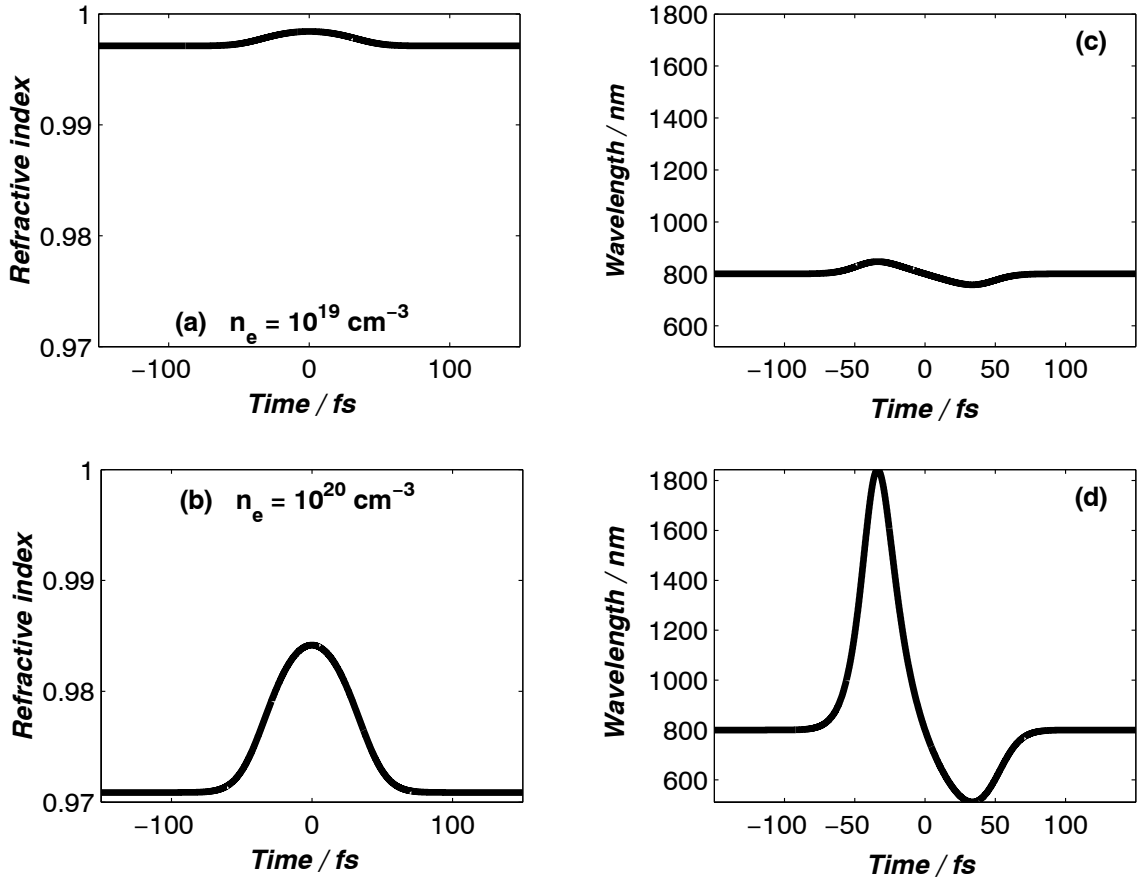

Figure 4.16. *Simple simulations to illustrate the effect of relativistically induced self-phase modulation in a plasma for a Ti:sapphire laser pulse with $\lambda = 0.8$ μm. (a) and (b): the resulting refractive indices in a plasma with electron densities of 10^{19} cm^{-3} and 10^{20} cm^{-3} for a laser pulse with duration 50 fs and peak irradiance 10^{19} W/cm^2. (c) and (d): The final time-dependent wavelength (i.e. chirp) acquired by the laser pulses after travelling through 0.5 mm of the plasma (GVD is omitted).*

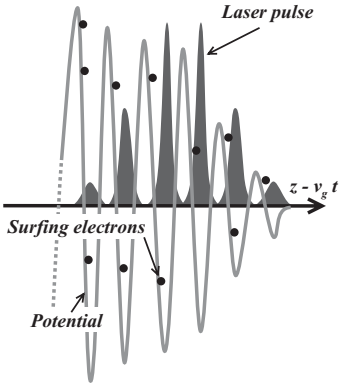

Figure 4.18. *The plasma wake in the long-pulse regime ($\tau \gg \pi/\omega_p$).*

into a minimum pulse energy requirement of 0.6 J, i.e. a power of more than 10 TW. If the laser pulse is longer ($\tau \gg \pi/\omega_p$), it still excites a plasma wave but in a more complicated manner, as illustrated in Figure 4.18. Such a pulse can interact with the plasma wave through Raman forward scattering instability and form light bunches, which repeatedly push the plasma wave, reinforcing it every time. The amplitude of the plasma wave can therefore reach higher values than in the short-pulse regime above.

For the electrons in the plasma, the wake that trails after the laser pulse constitutes a wave to "surf" on, because the plasma wave generates very strong longitudinal electric fields ("waves"). The bulk of the electrons simply oscillates in accordance with the plasma wave which is the wake, but some electrons start to surf the large amplitude electrostatic wave and accelerate up to considerable kinetic energies. Remember that the electrons in the plasma exhibit some kind of thermal energy distribution. Therefore, a few electrons with particularly high velocities can catch the travelling plasma wave, and surf it, gaining even more energy. This is called *wake field acceleration* (WFA) in the short-pulse regime (Fig. 4.17) and in the long-pulse regime *self-modulated wake field acceleration* (SMWFA) (Fig. 4.18) (cf. Landau damping).[18] If the amplitude of the plasma wave increases, it reaches to a point where the oscillatory velocity imposed on the electrons by the wave itself, approaches the phase velocity of the wave. This causes severe damping of the plasma wave, because a large number of electrons are caught by it and are accelerated forward.[18] The situation is referred to as *wave breaking*, because it effectively limits, or breaks, the peak electric field amplitude of the plasma wave. Thus, it also limits the maximum energy that can be acquired by accelerated electrons. Consider the electron oscillations in the longitudinal plasma wave, moving according to:

$$s\left(z,t\right) = s_0 \cdot \sin\left(\omega_p t - k_p z\right). \tag{4.10}$$

The electrons reach the wave phase velocity when the amplitude approaches $s_0 = v_{pp}/\omega_p = \lambda_p/2\pi$, where the phase velocity of the plasma wave equals the group velocity of the driving laser pulse, $v_{pp} = v_g$. Furthermore, at an amplitude of $s_0 = \frac{\lambda_p}{4}$, consecutive oscillation centres begin to overlap.[123] Both these conditions roughly describe wave breaking. Assuming the former condition, the maximum accelerating fields of the electrostatic wave can be derived as follows. The density fluctuation along the z-axis is,

$$\frac{\Delta n_e}{n_e} = \frac{ds\left(z\right)}{dz} \;\Rightarrow\; \Delta n_e = n_e \cdot \cos\left(\omega_{p0} t - k_p z\right). \tag{4.11}$$

From Poisson equation, $\nabla \cdot \mathbf{E} = e\Delta n_e/\varepsilon_0$, and the maximum electric field becomes

$$E_z^{max} \simeq \frac{m_e \omega_{p0} v_g}{e}. \tag{4.12}$$

Table 4.2. *The group velocity for different electron densities and irradiances ($\lambda = 0.8$ μm).*

n_e / cm^{-3}	I / Wcm^{-2}	v_g/c
10^{18}	10^{17}	0.9997
10^{18}	10^{19}	0.9999
10^{19}	10^{17}	0.997
10^{19}	10^{19}	0.999
10^{20}	10^{17}	0.97
10^{20}	10^{19}	0.99

In a relativistic description of the plasma wave it is found that the maximum field can become even higher (in a cold plasma):[23]

$$E_z^{max} \simeq \frac{m_e \omega_{p0} c}{e} \cdot \sqrt{2\,(\gamma_{pp} - 1)}, \tag{4.13}$$

where $\gamma_{pp} = 1/\sqrt{1 - v_{pp}^2/c^2}$ and $v_{pp} = v_g$. Since the group velocity of the laser pulse determines the phase velocity of the wake, an expression is deduced from (2.4), (2.16) and (2.17):

$$v_g \simeq c \left[1 - \frac{1}{2} \left(\frac{\omega_{p0}}{\omega} \right)^2 \frac{1}{\langle \gamma \rangle} \right]. \tag{4.14}$$

Eq. (2.14), derived for an electromagnetic wave acting on a single electron in vacuum, can be used to find approximate values for $\langle \gamma \rangle$. Table 4.2 lists the group velocity for different irradiance and plasma density using (2.14). For a plasma density of 10^{19} cm^{-3} and irradiance 10^{19} W/cm^2, the maximum electric field of the laser pulse wake, found using (4.13), is $E_z^{max} \simeq 2$ TV/m, or 2 GV/mm. However, in a plasma with a high temperature (random motion) the maximum electric field is lower.

The accelerating field can thus become immensely strong, but at some point the electrons attain such high velocities that they outrun the plasma wave. This is possible because the plasma wave propagates at approximately the group velocity of the laser pulse, which is lower than c. Electron *dephasing* is a serious problem for laser-based accelerator schemes.[23,105] Because of the difference in group velocity for different plasma electron densities, as seen in Table 4.2, the magnitude of the problem is seen to quickly increase with the electron density. A rough estimate of the maximum electron energy that can be acquired by the electrons with a certain plasma wave velocity can easily be calculated. For example, with an electron density of 10^{18} cm^{-3} and an irradiance of 10^{19} W/cm^2, the velocity of the plasma wave corresponds to an electron energy of $\sim$ 30 MeV. Remember that the electron actually outruns the plasma wave, so the actual maximum energy is higher.

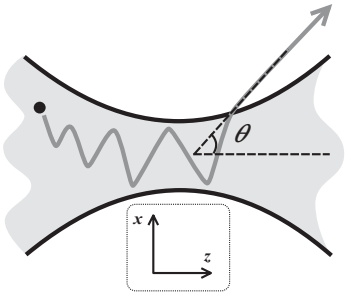

Figure 4.19. *Ejection of an electron from the laser focus.*

Direct Acceleration by the Laser Field

For direct acceleration of electrons by the laser field, other mechanisms can be invoked. Landau damping and wave breaking of the light wave in the plasma cannot occur effectively because the phase velocity of the light is greater than c, preventing resonant heating by the laser field. However, in the absence of these processes, others, which can be very efficient under certain conditions, can take over.

For example, electrons can be directly accelerated by the light field in the focus even in the absence of a plasma (Fig. 4.19). The irradiance is very high over a small radius, and electron ejection comes about because electrons are carried away from the focal volume, either because of their high oscillation amplitude or because of their drift velocity. The latter is determined collectively by the magnetic field component of the light, the time of ionization and the radial ponderomotive force.[11,124–126] If the laser field is strong, $\sim 10^{19}$ W/cm^2, the electron can be ejected with a few MeV of energy in this way. The higher the energy gained by the electrons, the more they propagate in the forward direction (smaller θ in Fig. 4.19), together with the laser pulse. Using the results from Appendix A, where the movement of an electron in a strong field is derived, the approximate direction can be shown to be,[23,125]

$$\tan\theta = \frac{p_x}{p_z} \simeq \sqrt{\frac{\langle\gamma\rangle - 1}{2}}, \tag{4.15}$$

with an expression for $\langle\gamma\rangle - 1$ given in (2.14) and the x and z directions given in Figure 4.19. Also in denser plasmas, such as those produced in the relativistic channelling experiments, this kind of electron ejection readily occur.

The plasma itself can provide quasi-static electric and magnetic fields for electron acceleration. These can force expelled electrons to be re-injected into the focus with an appropriate "phase" relative to the light wave, allowing the light to accelerate them further. Such an acceleration mechanism is called *direct laser acceleration* (DLA), and is based on a betatron resonance of the electrons in static electric and/or magnetic fields.[9,10,127] A static radial electric field is generated when electrons are ponderomotively pushed radially from the channel, and a solenoidal magnetic field is generated by the electrons moving in the forward direction (Fig. 4.20). An electron moving along the direction of the laser pulse will perform betatron oscillations in the static fields. The betatron frequency depends on the strength of the static fields and on the velocity in the forward direction of the electron. In order to understand how DLA works, envision a laser pulse propagating through a channel (Fig. 4.20) and that an electron with forward momentum is first ejected from the light channel by the pulse and then re-injected into the light channel by the static fields. The light wave moves

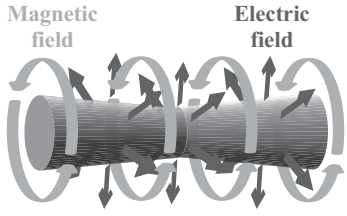

Figure 4.20. *The channel and the static electric and magnetic fields which facilitate direct laser acceleration.*

forwards at the phase velocity which is greater than c. *If* the electron returns at a time at which the the light continues to accelerate the electron, it will gain energy resonantly, oscillating in and out of the light channel. In principle, this means that every time the electron turns back at the perimeter of the light channel, the light field overtakes it by one period. DLA can readily compete with plasma acceleration processes under certain conditions, but it is difficult to determine experimentally which mechanism is responsible for the acceleration. Simulations suggest that DLA is most effective in situations where other acceleration processes such as SMWFA or wave breaking are prevented for some reason, and the laser power threshold is estimated to be about six times the critical power for relativistic self-focusing.[10]

4.2 Experimental Set-up

This section describes the common experimental components required, such as the evacuated experimental chamber, the focusing optics and the gas valve that produces the jets of gas into which the laser is focused. Following this, certain measurement techniques and their corresponding set-ups are also discussed. Measurements of the relativistic channel extension, the plasma electron density and the energies and number of electrons are presented and described.

4.2.1 Prerequisites

A broad outline of a typical set-up used in the experiments discussed in this chapter is shown in Figure 4.21. The laser pulse

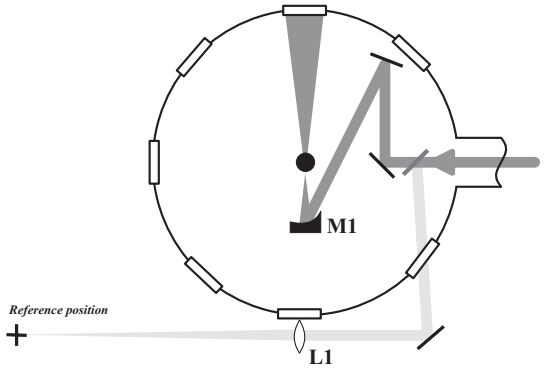

Figure 4.21. *The experimental set-up with alignment check. The horizontally polarized laser beam enters from the right and is focused by an off-axis parabolic mirror, M1, into the gas-jet. About one percent of the pulse is split off and is focused by a lens, L1, onto a remote screen.*

propagates through an evacuated tube from the compressor to the

experimental chamber. Two mirrors steer the pulse to an off-axis parabolic mirror that focuses the light at the centre of the evacuated chamber. In order to certify that the crucial alignment of the parabolic mirror is maintained on a day-to-day basis, a thin beam splitter has been introduced, which reflects a small part of the light ($\sim 1\%$) through a window via an iris to a lens ($f = 4.5$ m) that focuses the light onto a remote screen. The spot on the screen serves as a reference position for the alignment.

The off-axis parabolic mirror is coated with silver, has a diameter of 7.5 cm and a focal length of 15 cm. The quality of the laser focus using this kind of focusing mirror, is exceedingly sensitive to mirror misalignment. Two different methods were used to align the mirror. The more difficult method involved imaging the focus with a 50 mm or 135 mm camera objective, producing a magnified image on a CCD chip. This allowed quantitative analysis of the focal spot-size and its shape. The other method was the one used in the X-ray generation set-up (Section 3.2.3). While steadily decreasing the laser pulse energy, the mirror alignment was adjusted in order to maintain the visible spark that was generated when the mirror focused the laser pulse in air. This method is simpler and allowed a faster adjustment to find the smallest focal spot but it gives no information on size or shape of the focus.

Just above the laser focus, or more accurately 0.2 mm above it, is the orifice of the pulsed gas nozzle that produces the gas jet for the experiment. The gas nozzle must to be able to produce gas jets of varying densities, up to ten times atmospheric pressure and produce a well-defined beam-like gas jet. It must also be possible to open and close the gas flow very quickly. The first demand arises from the relativistic-self focusing mechanism. The lower the gas (electron) density, the higher the power needed to induce a strong relativistic focusing effect (Table 4.1). The second demand arises from the fact that a slowly rising density can cause defocusing of the laser pulse, before it reaches a density at which it can self-focus. Simply put, the leading edge of the laser pulse produces a low-density plasma on the edge of the gas plume, where the pulse cannot be efficiently guided because the density is too low. A slowly rising density gradient also complicates the conditions in the experiment, by allowing the plasma frequency to vary. The third demand is of a more technical character. The vacuum-pumps have a limited capacity, so the longer time the gas nozzle is open the lower the experiment repetition rate. In order to keep the average pressure at a reasonable level of $\sim 10^{-4}$ mbar, the experimental repetition rate is presently limited to one shot every five seconds.

The gas nozzle that was used in the experiments presented in this chapter is mounted on a solenoid-type valve. The nozzle can be replaced to produce gas jets of various sizes (0.8 or 0.5 mm). A larger nozzle orifice means a lower gas density, however. The valve can operate with backing gas pressures up to 85 bar, which

was barely enough to produce an electron density of a few times 10^{20} cm^{-3} with helium gas, using the larger orifice. Helium was used to generate relativistic channels throughout the experiment, because it has only two electrons which are easily removed. A heavier gas would have produced a higher electron density at a given gas density, but the laser pulse might not have been able to remove all electrons. In such a situation, there would be a radial gradient in the electron density which would cause defocusing of the laser pulse, possibly preventing self-focusing.

Role of Pre-pulses and ASE

The ASE and the pre-pulses from the multi-terawatt arm can, if they are strong enough, pre-ionize the gas. The gas valve in the experimental chamber was operated on a millisecond timescale, which means that the gas was present when the pre-pulses reached the focus. Assuming that the pre-pulse to main pulse ratio was 10^{-4}, a reasonable number, the irradiance produced by the strongest pre-pulse in the focus was of the order of 10^{15} W/cm^2. In general, such an irradiance only *partly* ionizes the high-density gas used in the experiments, generating a radially decreasing electron distribution. Recalling that the refractive index of a plasma decreases with increasing electron distribution, it can be concluded that a pre-pulse-generated electron distribution acts as a negative lens for the main pulse. Thus, the focusing conditions of the main pulse change and in the worst case the pre-plasma would prevent relativistic self-focusing. In the experiments in this chapter the effect of the pre-plasma was not explicitly studied, but since relativistic channelling was regularly achieved, the pre-plasma refraction must have been of minor importance.

Safety Issues

Experiments generating relativistic channels can be dangerous from a radiation point of view, unless caution is exercised and the radiation level is monitored in real time. Since electrons are accelerated by the laser up to very high energies of several MeV, Bremsstrahlung can cause a serious problem. Fortunately, the most energetic electrons form a beam of small divergence that co-propagates with the laser pulse. Therefore, in our experiments, the electrons could be made to exit the evacuated experimental chamber through a few centimetres of glass and impinge on a concrete wall on the basement level of the laboratory building. Careful monitoring of the X-ray yield with an ion chamber revealed that the radiation was on the same level as the background in the building a few metres from the experimental chamber, except where the beam of electrons propagated. However, the electron beam itself could easily generate doses of the order of the maximum allowed dose

for radiological personnel (50 mSv) with a *single* laser pulse, motivating extreme caution in the vicinity of the chamber. During our experiments, the ion chamber was placed next to the personnel, integrating the radiation dose. If the dose would have exceeded a pre-determined limit, the ion chamber would have sounded an alarm. For example, if the laser were misaligned and were focused onto the gas nozzle, the situation would be similar to that in the X-ray experiment presented in the previous chapter. With the extreme irradiance produced by the multi-terawatt arm, large amounts of very hard X-ray radiation would then isotropically exit the experimental chamber.

In addition to the real-time radiation monitoring, all personnel wore thermoluminescent detectors (TLDs), which were analysed on a monthly basis, giving a good measure of the integrated dose. Together, the ion chamber and the TLD badges provided a good safety level.

4.2.2 Measurement Techniques

In the relativistic channelling experiment presented in this chapter many detection techniques made use of the scattered laser light following the interaction between the laser pulse and the plasma. For example Raman- and Thomson-scattered light revealed many aspects of relativistic channelling. Furthermore, since accelerated electrons co-propagate with the laser pulse, their energy spectrum and their total number could be determined. The various techniques employed in the experiments on laser-pulse channelling are presented and discussed below.

Side-Scattered Light

In accordance with (4.7), the Thomson-scattered light and the plasma recombination light is imaged at 90° to the propagation direction in order to "see" the relativistic channel form inside the plasma and to measure its extension. An imaging system has been constructed, using a 13.5 cm focal length objective, which focuses the 30 times magnified image onto a CCD chip (8-bit). The set-up is shown in Figure 4.22 and typical images of the channel are shown in Figure 4.23. As the relativistic channel generally has a very small diameter, of the order of a few micrometres, the laser irradiance is very high in the channel. Therefore, a luminous and channel-like structure is expected to be visible in the focus where the channel forms. In the present set-up, the direction of imaging is normally parallel to the (horizontal) polarization direction, which may not seem optimal, but imaging perpendicularly to the polarization direction gives similar images. This is not surprising because the imaging system has a finite acceptance angle (numerical aperture) and some of the Thomson-scattered light is there-

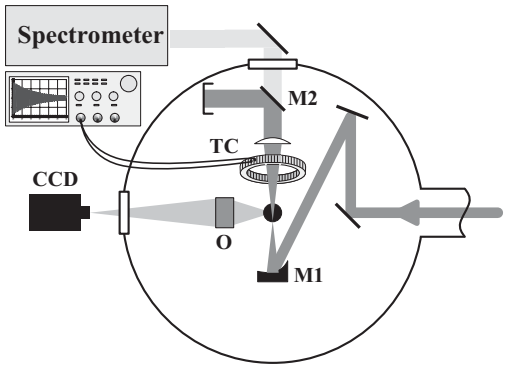

Figure 4.22. *The experimental set-up showing the side-scattering imaging system and the diagnostics for forward Raman-scattered light. The laser pulse enters from the right and is focused by an off-axis parabolic mirror, M1, into the gas jet. The channels formed are imaged onto a CCD chip using an objective, O. After the gas jet, laser radiation at the fundamental laser wavelength is reflected by a dielectric mirror, M2, to a beam dump, while forward Raman-scattered light is transmitted through M2 to a spectrometer outside the evacuated chamber.*

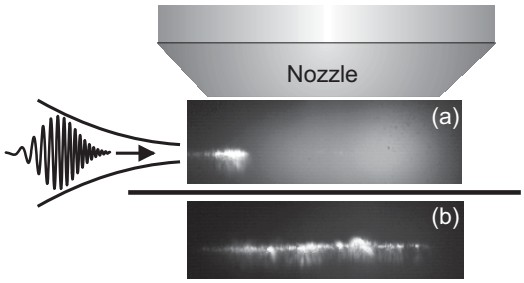

Figure 4.23. *(a) The onset of relativistic channel formation. The pulse duration was 30 fs and the energy was 50 mJ. (b) A relativistic channel that has grown through the gas medium. The length of the channel, 750 μm, equals 21 times the Rayleigh range. The pulse duration was 65 fs and the energy is 120 mJ. The diameter of the gas orifice is in both cases 0.8 mm, and the valve produced an electron density of* $7 \cdot 10^{19}$ *cm*$^{-3}$*. For clarity the chirp of the pulse has been greatly exaggerated.*

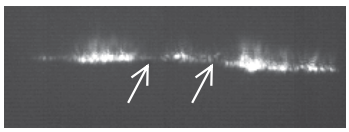

Figure 4.24. *Sometimes the irradiance of the Thomson-scattered light dropped in the channel.*

fore always imaged. The limited resolution of the imaging system did not allow differentiation between laser beam filaments and whole-beam self-focusing. However, the Thomson-scattered light sometimes showed a short initial channel, then nothing was seen for a few hundred micrometres, after which the channel appeared to continue (Fig. 4.24). The reason could be electron cavitation which, according to (4.7), decreases the amount of scattered light, or it could be an effect of sausaging of the relativistic channel (see Section 4.1.1), which causes varying laser irradiance.[104,113] For example, if the electron density inside the channel drops by a factor ten, the irradiance of the Thomson-scattered light will decrease accordingly. This means that the channel becomes "invisible" to the imaging system (the 8-bit CCD chip), because the signal is below the background level. Because of the uncertainty of the origin of the "dark channels", these images were usually discarded from any channel extension analysis.

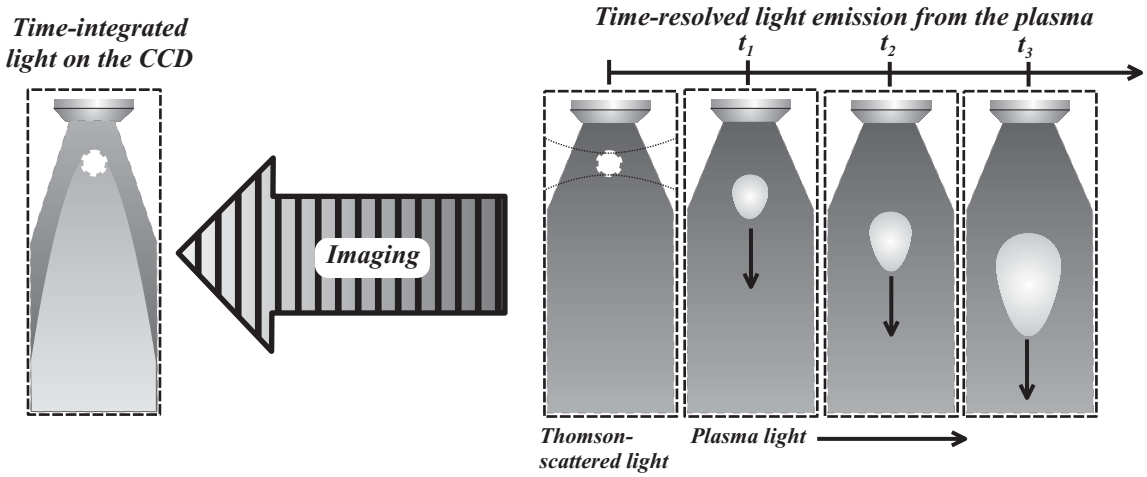

Figure 4.25. *Illustration of how the CCD integrates the course of events in the plasma. In this case, the laser pulse forms a plasma spark at time t_0, leading initially to Thomson scattering. The gas exits the nozzle at almost the speed of sound. When the laser pulse has passed through the gas, the plasma shows an afterglow as the helium gas recombines and emits light that originates from atomic transitions.*

The CCD chip could be replaced by a fibre which transfers light from the magnified image to a spectrometer. The fibre tip was moved perpendicularly to the extension of the channel in small steps, successively recording spectra (Figs 4.25 and 4.26). At the position of the channel ($\sim$ 0.3 mm wide in the image plane), the spectra show a strong peak representing the Thomson-scattered light. Below the channel, the Thomson-scattered light decreases in favour of plasma recombination light. Since the (ionized) helium gas moves at approximately 1 km/s after leaving the orifice, the

series of spectra represent light emitted at different times from the recombining plasma. The fibre is 0.2 mm in diameter and, with 30 times magnification, the temporal resolution is of the order of 10 ns. The two spectra in Figure 4.26 consequently show light emitted at the time of the laser pulse (on the channel) and 0.1 μs later.

The "on-channel" spectra, recorded with different laser pulse durations, 30 fs and 540 fs, but the same pulse energy, have a quite different appearance. The promptly Thomson-scattered light results in a peak of similar strength in both cases, but the spectrally broad background is clearly blue-shifted in the case of the shorter pulse. The red-shifted light in the long-pulse spectrum can either be attributed to Raman scattering at a large angle to the direction of pulse propagation or more likely through Thomson scattering of the Raman Stokes-component. The long pulse duration leaves sufficient time for the Raman forward scattering instability to grow. The shorter pulse, however, exhibits about ten times higher peak irradiance and is therefore subjected to more severe self-phase modulation (Section 4.16), particularly at the sharpened rising edge of the pulse (Section 4.1.4). This causes a large blue shift, which explains this spectral feature. The lack of red-shifted light can be attributed to the short time available for Raman forward scattering instability to grow.

Forward scattered Light

The forward directed light consists of the laser light that remains after the channel and Thomson- and Raman-scattered light. The remnant of the laser pulse was usually at least as strong as the scattered light in our experiments, and in order not to saturate the detectors, this light was reflected by a dielectric mirror (Fig. 4.22). This mirror has a bandwidth of approximately 0.1 μm centred around 0.8 μm. The remaining light is transmitted by the mirror and collected on a pad which diffusely scatters the light into a fibre-coupled spectrometer.

The Stokes-component for different helium backing pressures is shown in Figure 4.27. The spectra were recorded with an modest irradiance of $\lesssim 10^{18}$ W/cm^2. Assuming a constant electron density throughout the relativistic channel and neglecting the dependence on the electron temperature and $\langle\gamma\rangle$, the frequency at the Raman peak determines the plasma electron density through the relation in (4.8). When the irradiance is increased, the Raman peak broadens while the general background quickly increases. The background arises from relativistic self-phase modulation of the laser pulse and the peak broadening can be explained by the cavitation that occurs in the channel. The change in electron density takes place while the pulse propagates through the channel, and therefore Raman scattering occurs with a continuously changing plasma

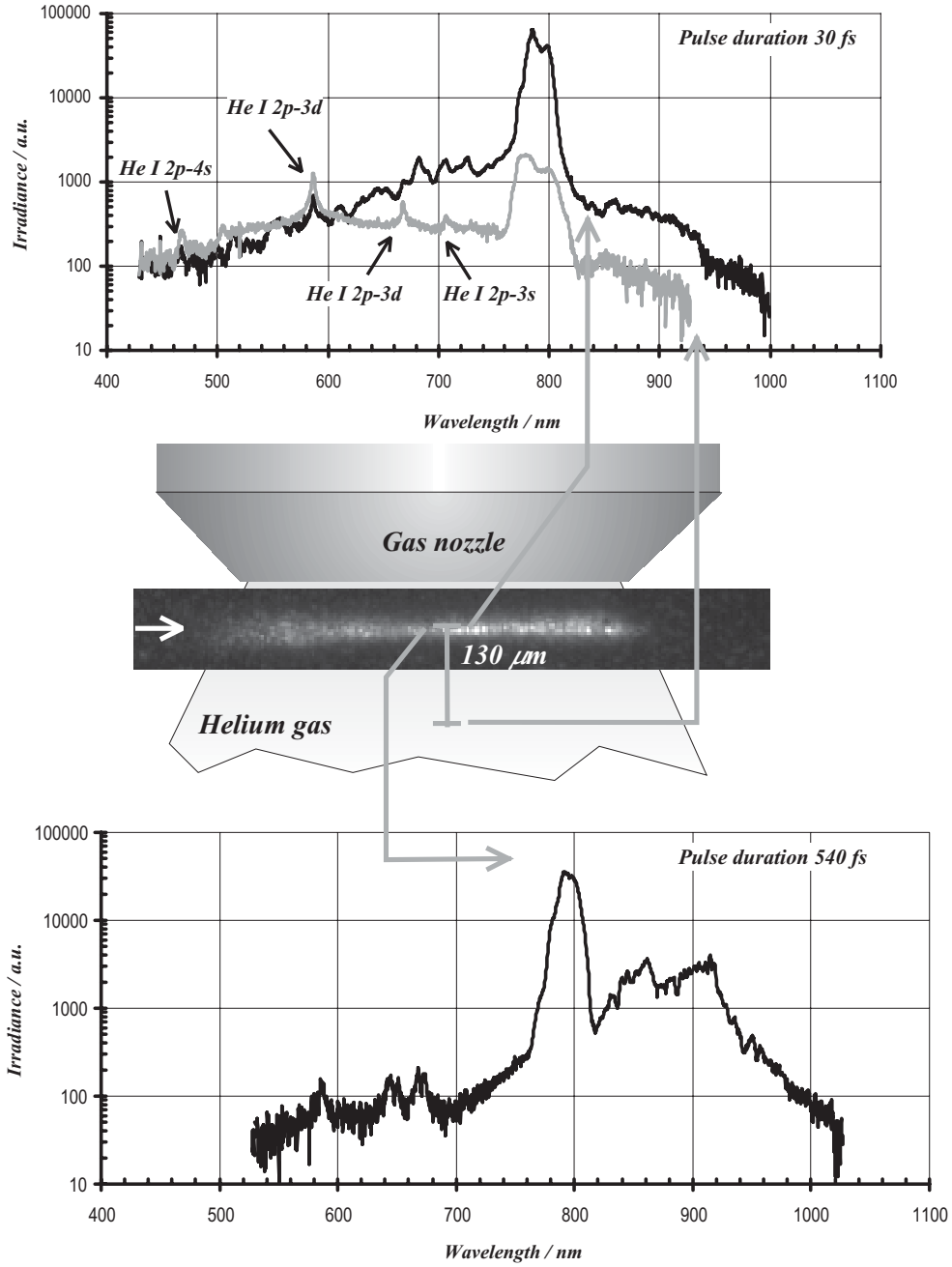

Figure 4.26. *Spectrally resolved side-scattered light from the channel (black traces) and from 130 μ below it (grey trace). The spectra for short (upper) and long (lower) pulse durations are very different, except for the Thomson peak at 0.8 μm. The shorter pulse generates less red-shifted light but more blue-shifted light. The laser pulse energy was 0.3 J and the electron density was $8 \cdot 10^{19}$ cm^{-3}.*

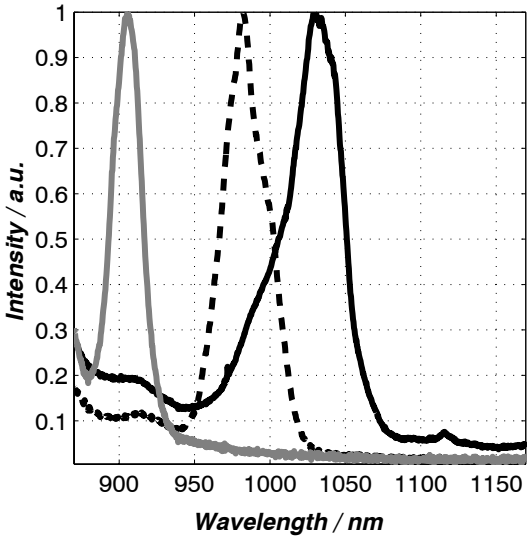

Figure 4.27. *This figure shows the normalized first Stokes Raman peaks generated in the underdense plasma. The light is collected as indicated in Figure 4.22, by first reducing the laser light with a dielectric mirror and then collecting the scattered light to a spectrometer. The resolution is of the order of one nanometre in this spectrum. The three peaks originate from spectra collected at different electron densities in the plasma (2, 6 and 9 times* 10^{19} cm^{-3}*), and the location of the peak is related to the correspondingly different plasma frequencies.*

frequency, effectively broadening the Raman line towards lower frequency shifts (lower plasma density). Higher orders of the Raman scattering process are conceivable but cannot be detected with the present set-up, because the spectrometer is equipped with a CCD camera, which limits the sensitivity to a maximum wavelength of 1.1 μm.

Further information might be included in the location and width of the Stokes (and anti-Stokes) line. For example, the electron average mass and thus the laser irradiance in the channel could possibly be deduced from the γ-dependence of the plasma frequency.

Number of Accelerated Electrons

In initial attempts to count the number of forward accelerated electrons Faraday cups of various designs were used (Fig. 4.28).[128,129] The Faraday cup, which measures the total charge of the absorbed electrons, proved to be exceptionally difficult to handle in the experimental set-up, because it acted as an antenna, picking up a great deal of noise. The idea is that the cup accumulates the charge, which is subsequently measured. Instead, a toroidally

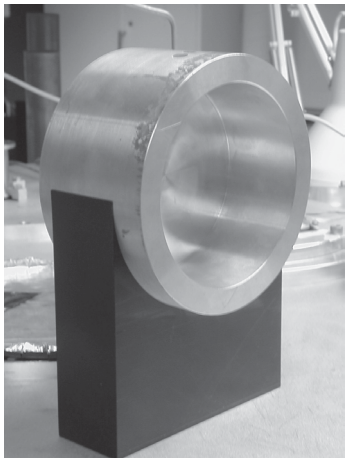

Figure 4.28. *A Faraday cup that can be used to measure the total charge of the particles absorbed in it.*

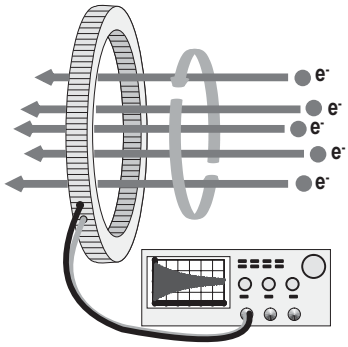

Figure 4.29. *The toroidal coil measures the total charge of the pulse of particles passing through it.*

wound coil with twenty copper-wire turns was used in conjunction with an oscilloscope to measure the total charge of the electrons accelerated in the near-forward direction (Fig. 4.22).Normally, the toroidal coil was placed about 10 cm from the laser focus, measuring all electrons emitted in a 100° cone. From (4.15) and Appendix A, this angle can be shown to include electrons of energies higher than ~ 0.7 MeV that are ponderomotively ejected from the channel. Electrons that are accelerated through other mechanisms such as wake-field acceleration or direct laser acceleration probably exhibit a smaller divergence. The electrons move through the coil and induce a current, which excites a resonant oscillation in the electronic circuit (Fig. 4.29). The duration of the induced current can be assumed to be infinitely short compared with the resonance frequency of the circuit. After some calculation, the response of the current pulse, as seen by the oscilloscope, becomes:

$$u_{\mathrm{osc}}(t) \simeq -\frac{Q_e}{NC} \exp(-at) \cos bt, \tag{4.16}$$

where $a^{-1} \sim 1.2$ μs, $b^{-1} \sim 0.12$ μs and $Q_e = \int i(t)dt$ is the total charge of the electrons passing through the toroidal coil. Eq. (4.16) shows that the charge of the electrons is proportional to the voltage amplitude at time zero, which was easily measured on the oscilloscope. Appendix B gives further details on the toroidal coil and its electric circuit.

Electron Energy Spectrum

The energy spectrum of the electrons was detected with a simple permanent-magnet electron-spectrometer. A fluorescent screen was placed behind a 5 cm thick collimating plastic block. The block has a 1 cm hole, where those electrons coming straight from the relativistic channel could pass through. The electrons generated a luminous imprint on the screen which was imaged by a CCD camera. The laser light was blocked by a few hundred micrometres of aluminium. By simply approaching the electron beam with a relatively weak permanent magnet (~ 3 mT), the electrons bent in the magnetic field, at different angles depending on their energy. A spectrum of the electrons thus formed on the screen. Because of the limited magnetic field of the simple spectrometer it could not be used to measure the electron spectrum above 10 MeV. Much better performance could be achieved with a dedicated permanent-magnet spectrometer, such as the one built by C. Gahn,[130] and with a stronger magnetic field higher electron energies could be measured.

4.3 Experimental Results and Discussion

4.3.1 Relativistic Channelling

In the course of the relativistic self-focusing experiments, the channel length was measured on a shot-to-shot basis. The general explanation for the channel extension is that the plasma continues to guide the pulse either until its power falls below P_C or until the plasma ends (reaching the end of the gas jet). The pulse energy is reduced in the process of self-focusing, through diffraction and electron heating losses, and channelling can therefore only occur up to the point where the power falls below P_C. The loss due to ionization is very small in this context.

Upon increasing the electron density, we found that the channel grew up to a point after which it started to shrink (Fig. 4.30). Increasing the electron density means decreasing the critical power

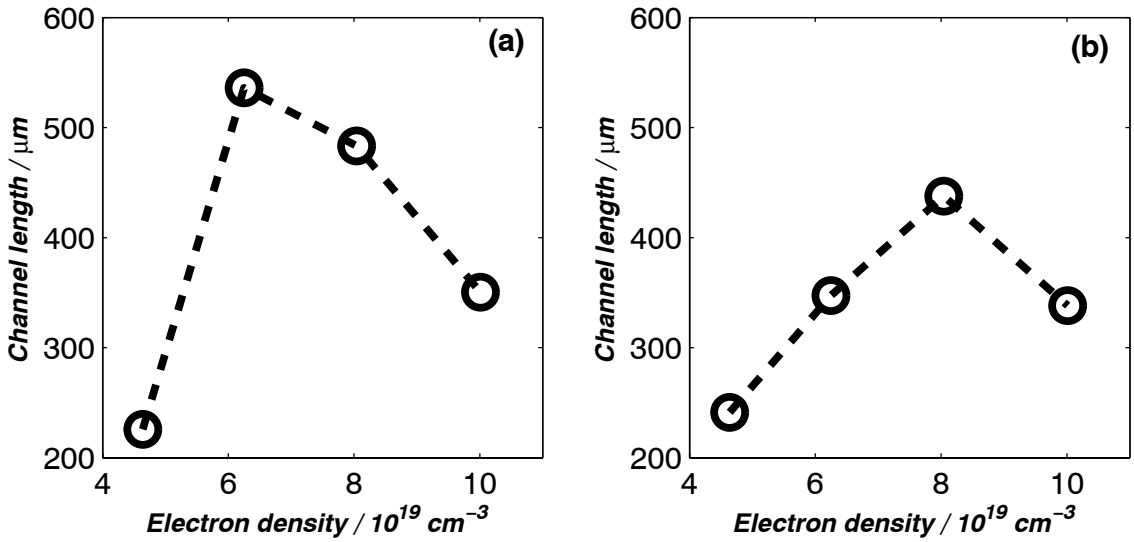

Figure 4.30. *Measurements of the channel extension based on the side-scattered Thomson light, when varying the electron density. (a) Results from an experiment with a pulse duration of 30 fs and energy of 0.17 J. (b) Results from an experiment with a pulse duration of 50 fs and energy of 0.17 J.*

($\propto 1/n_e$), thus increasing the strength of the relativistic focusing effects. Therefore, in a general sense, the part of the pulse that is efficiently coupled into the channel increases with the electron density. However, at higher electron densities, the transfer of energy from the laser pulse to the electrons dominates, and the same pulse energy suffices only for a shorter channel.

By the same argument, the channel is expected to grow as the pulse energy increases, because the pulse can loose more energy be-

fore the power falls below P_C. This was indeed confirmed by the experimental results (Fig. 4.31 and Paper III). However, some-

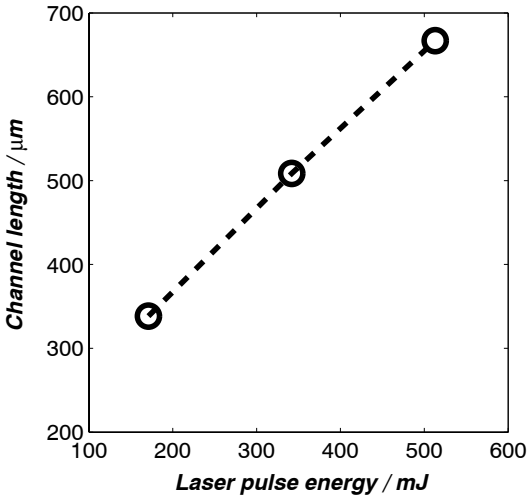

Figure 4.31. *A measurement of the channel extension, based on the side-scattered Thomson light, when varying the laser pulse energy. The pulse duration was 50 fs and the electron density* 10^{20} cm^{-3}.

thing else happens when the laser energy is raised. According to theoretical simulations by A. Pukhov et al., given ultra-relativistic irradiances ($\gamma \gg 1$), in our case corresponding to $I > 10^{18}$ W/cm^2, the energies of electrons expelled from the channel are proportional to the square root of the irradiance. In other words, the losses suffered by the laser pulse per unit distance is also proportional to the square root of the irradiance.[9,10] The origin of the losses has not been determined; it could be one or several of different loss mechanisms, such as Raman forward scattering instability, wave breaking/Landau-damping, direct laser acceleration or ponderomotive expulsion. Under the assumption that the losses follow a $\sqrt{I}$ dependence, a simple model describing the experimental findings, should consequently show a channel growth proportional to $I/\sqrt{I} = \sqrt{I}$ for a constant electron density. This assumption regarding the losses should be tested. For example, a considerable amount of energy is probably lost as the leading edge of the pulse continuously diffracts out of the focus, because it does not experience the strong relativistic lens generated by the following part of the pulse. However, in the present model, the diffraction losses are also assumed to be small as compared to the losses due to electron heating.

In order to test these very simplistic arguments, pulses of different durations but constant energy were used to generate relativistic channels. By moving one of the gratings in the compressor of the

CPA laser, the pulse duration could be altered. To the first order, the longer pulses exhibited only linear chirp but, as the pulses becomes longer (several hundred femtoseconds), the temporal envelope of the pulse generally takes on the shape of the spectrum envelope *and* higher orders of chirp modulate the pulse. The temporal envelope was measured for all grating positions used in the experiments, and it was found that when the pulses was stretched to more than about 250 fs, rather strong modulations appeared. In the context of self-focusing, which requires a certain critical power, it is possible that pulses which seemingly have too low a power, may self-focus if a strong peak exists in the temporal envelope. Figure 4.32 shows how the extension of the channel increases as the pulse duration increases (similar for chirps of both signs). This behaviour cannot be explained by the model described above.

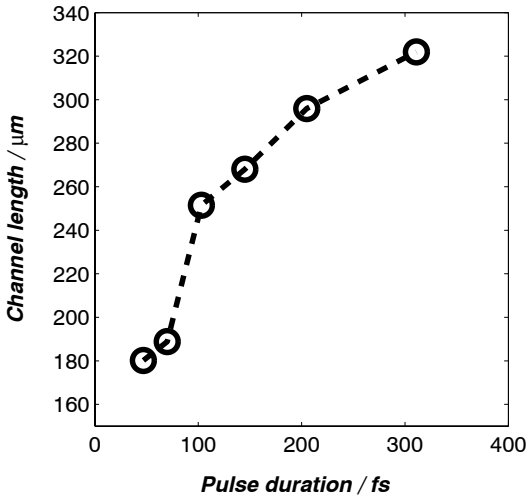

Figure 4.32. *Measurement of the channel extension based on the side-scattered Thomson light, when varying the laser pulse duration. The pulse energy was 0.12 J and the electron density* $\sim 5 \cdot 10^{19}$ cm^{-3}.

In order to understand the results presented in Figure 4.32, the above model is expanded with another logical argument. The transfer of energy from the laser pulse to the electrons can be assumed to occur at the front of the laser pulse, thus eroding it. This is approximately true whether the energy loss is due to cavitation or Raman scattering leading to wave breaking. Thus, the erosion rate can be expressed as:

$$\frac{d\tau}{dz} \propto \frac{\text{loss per unit distance}}{\text{pulse energy per unit time}} \propto \frac{\sqrt{I}}{I} = \frac{1}{\sqrt{I}}, \qquad (4.17)$$

where z is the coordinate along the axis of propagation. The loss per step along the axis of propagation (dz) is proportional $\sqrt{I}$

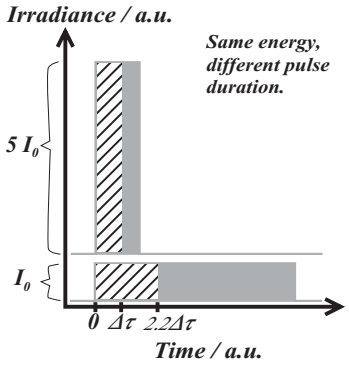

Figure 4.33. *Two pulses with different pulse durations but equal energy suffer from different amounts of erosion ($\Delta\tau$ and $2.2\Delta\tau$, respectively) per unit distance, Δz, along the axis of propagation.*

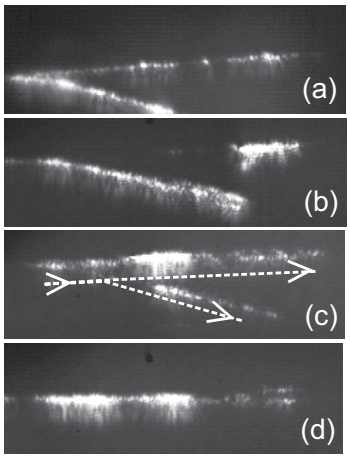

Figure 4.34. *Sometimes the Thomson-scattered light shows that the channel splits.*

because of electron heating, and the duration of the corresponding eroded part decreases as $1/I$ (Fig. 4.33). Erosion continues until the pulse is exhausted of its energy, at which time the guiding of the laser pulse ceases. The model predicts that this happens after a distance, L,

$$\frac{dz}{d\tau} \propto \sqrt{I} \;\Rightarrow$$
$$L \propto \sqrt{I}\,\tau. \tag{4.18}$$

The dependence of the channel length on the electron density can be estimated from the experimental findings in Figure 4.30, and the supporting arguments, to be:

$$L \propto n_e^{\alpha}, \tag{4.19}$$

where $\alpha \simeq 1$ at "low" densities and $\alpha \simeq -1$ at "high" densities (see the discussion above and Fig. 4.30). Eqs (4.18) and (4.19) reveal roughly how the parameters govern the length of the relativistic channel.

In a more detailed model, variations in channel radius and varying critical power should be taken into account. Changes in the radius of the relativistic channel lead to changes in the laser irradiance in the channel and thus affects the electron heating. Effects such as cavitation become more pronounced at the end of the laser pulse, which therefore experiences an effectively lower critical power.

The Raman forward scattering instability is expected to grow differently depending on the sign of the chirp (Section 4.1.3). In our experiments, however, the channel extension was not influenced by the sign of the chirp. If the length is indeed coupled to the energy loss of the pulse, is should also be sensitive to the growth of the Raman instability. This fact suggests that in our experiments on relativistic self-focusing, Raman forward scattering instability is not so important for the laser pulse losses, perhaps because some competing process, such as wave breaking, limits the instability growth.

Channel Splitting

Sometimes during our experiments, the Thomson-scattered images revealed channels that were apparently "split", and the pulse continued in two separate channels (Fig. 4.34). Whether this behaviour was a result of the laser pulse, the plasma, or both, is not clear. It may be that there is some plasma instability which can grow exceedingly fast, changing the density considerably, and that the trailing part of the laser pulse is refracted and travels in another direction. It may also be that accelerated electrons overtake the laser pulse and disrupt the smooth refractive index in front

of the pulse, causing deflection, or *snaking*, of parts of the laser pulse.[131] The plasma density may also be very high at a particular point, causing the first part of the pulse to change direction, while the trailing part is intense enough to penetrate the denser plasma. Whatever the reason, the mere fact that split channels exist inspires new thinking; can relativistic channels be split and reconnected at will? If that is the case, it does indeed improve the prospects of using plasma waves in relativistic channels as particle accelerators, because if channels can be connected and the electrons from one channels seeded into the next, dephasing of the electrons can be circumvented.

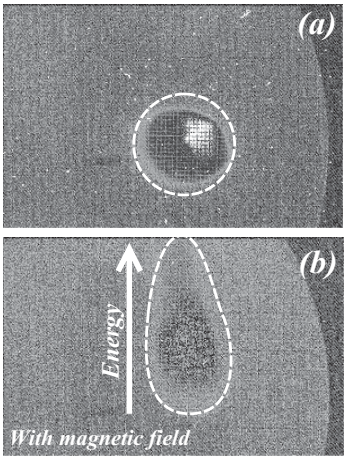

Figure 4.35. *The spot of the electrons on the fluorescent screen with and without the permanent magnet, indicating that electrons of at least 10 MeV are accelerated in the relativistic channel.*

4.3.2 Electron Acceleration

Electron Energies

Using the simple spectrometer described earlier, the energy distribution of the electrons could be assessed by studying the trace of the electron beam on the scintillator. Figure 4.35 shows two images of the scintillator, with and without a static magnetic field. The electron trace with the magnetic field present, indicates that some electrons had been accelerated to energies higher than 10 MeV. Most of the electrons had lower energies, but the presence of the high-energy electrons from a ~ 0.5 mm long channel shows that if the electron were accelerated by an electric field through the channel, similarly to a linear accelerator (LINAC), the field strength must have been greater than 20 GV/m in the relativistic channel. Although this is small compared to the estimated limit in (4.12), it is still an amazing strength; a thousand times the maximum gradient that are generated in LINACs today.

Number of Accelerated Electrons

Several studies on the number of accelerated electrons have been realized in the relativistic self-focusing experiments, utilizing the toroidal coil described above (Fig. 4.29). Up to $\sim 5 \cdot 10^{10}$ electrons were accelerated by a single laser pulse. Due to the large acceptance angle of the toroid, it was not possible to determine which of the different electron acceleration mechanisms that produced the electrons. With "very low" laser irradiance ($\sim 10^{17}$ W/cm^2), some electrons were still detected (~ 1 pC, i.e. $6 \cdot 10^6$ electrons). These were probably ejected by the ponderomotive pressure and by the drift velocity acquired during ionization. This means that they were expelled from the focus at a relatively large angle to the laser pulse propagation axis.

The channel length was monitored simultaneously with the electron measurements, allowing shot-to-shot comparisons of the number of electrons and the channel length. For example, the data

in Figure 4.36 were acquired at the same time as those in Figure 4.30(a). Figure 4.36 illustrates how the number of electrons

1 nC of charge corresponds to $6 \cdot 10^9$ electrons.

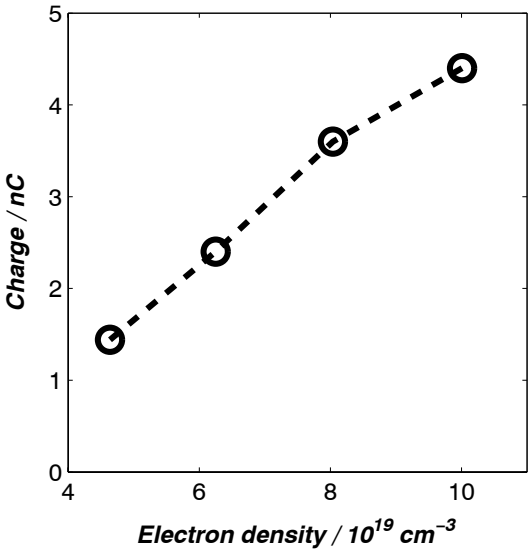

Figure 4.36. *The total charge of accelerated electrons versus the electron density (cf. Fig. 4.30(a)). The laser pulse parameters were 0.17 J, 30 fs.*

increases with the electron density. It does not show the kind of saturation that limits the channel extension. Increasing the energy of the laser pulse also increased the number of electrons (Fig. 4.37), similarly to the growth of the channel.

Finally, when varying the laser pulse duration, the change in the number of electrons is seen to clearly deviate from the channel growth (Fig. 4.38). The number of electrons seems to follow a $\sim 1/\tau$ dependence.

These results together seem to imply that in the experiments, the number of electrons, N, was linearly proportional to the laser pulse irradiance and the electron density,

$$N \propto n_e \, I. \tag{4.20}$$

It is difficult to draw any direct conclusions from this expression, but the general behaviour is rather intuitive.

4.4 Summary and Outlook

The work presented in this chapter has the purpose of initiating a new field of science, i.e. physics of relativistic self-focusing and plasma physics at relativistic irradiances, at the High-Power Laser Facility at the Lund Laser Centre, and to extend the knowledge

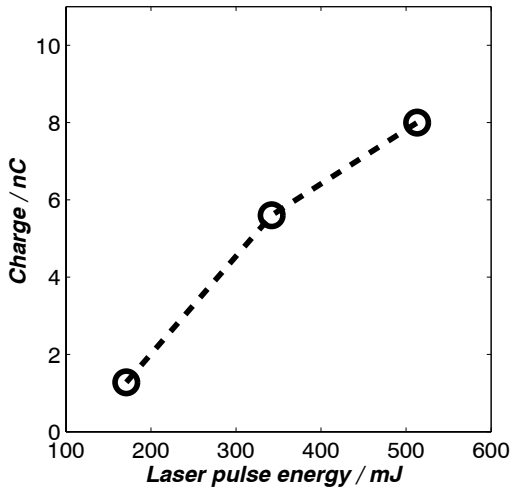

Figure 4.37. *The total charge of accelerated electrons versus the laser pulse energy. The laser pulse duration was 50 fs and the electron density* $5 \cdot 10^{19}$ cm^{-3}.

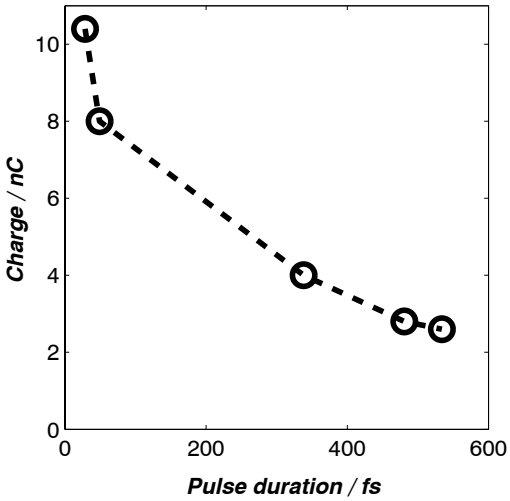

Figure 4.38. *The total charge of accelerated electrons versus the laser pulse duration. The laser pulse energy was 0.5 J and the electron density* $5 \cdot 10^{19}$ cm^{-3}.

on this subject. One of the laser systems at the High-Power Laser Facility has been redesigned for this purpose and a new laser arm has been added that can deliver the fine-tuned laser pulses required in these experiments. Also the experimental equipment, from the vacuum system and the evacuated experimental chamber, to the set-up of the diagnostic parts for the experiment have been implemented and used: Relativistic channels have been generated since the year 2000.

The dependencies of the extension of the relativistic channel on various parameters of the laser pulse and for the plasma, have been subjected to study. As a result of this, and with the co-operation of the research group in Garching, Germany, a theoretical model for the length of the relativistic channel has been proposed (Paper III).

In addition to this, the kinetic energy of the electrons has been estimated using a permanent magnet electron spectrometer. A new, specially designed spectrometer of similar type has been constructed and will be implemented in the coming experiments. It has a much better energy resolution and can be used to measure energies up to about 100 MeV. Furthermore, a device for measuring the charge of electrons accelerated in the forward direction has been developed. Using this device, the variation in the number of electrons has been studied for different laser pulse and plasma parameters (Paper IV).

Looking to the near future, several interesting studies can be carried out. For example, an experiment with the new electron

spectrometer, Raman detection and the toroidal coil could give important information on the behaviour of the acceleration mechanism as a function of the laser pulse chirp (see Section 4.1.3). The laser pulses can now also be altered through the use of a so-called Dazzler™,[132] manufactured by Fastlite, which allows better control over the chirp. A Dazzler is an acousto-optic programmable dispersive filter of sorts, which can be used to tailor the chirp and spectrum of the laser pulse. Placed early in the laser system, before the stretcher, it is normally used to pre-compensate for temporal and spectral distortions that the pulse undergoes through the laser system, but it can also be used to generate exotic pulse shapes, or pulse trains, with variable chirp.

Also the angular distribution of the accelerated electrons should be investigated. In the experiments already carried out, only a small part of the forward accelerated electrons were detected because a collimator blocked electrons ejected at angles larger than a few degrees. It has been reported that collimated beams of electrons are sometimes produced, standing out from the general background of forwardly accelerated electrons. The mechanisms behind such electron beams should be studied, as they could provide more information on the laser-plasma interaction in the relativistic channel.

Possibilities of accelerating electrons to much higher energies than given by the dephasing limit is of large interest and could be investigated in future experiments.[133] Is it possible to seed a second relativistic channel with electrons from a first channel, for example? This could circumvent dephasing and maybe also produce a peaked electron energy-distribution, as opposed to the exponentially decreasing distribution that is generally achieved.

Chapter 5

Summary and Future Research

In the course of the work presented in this thesis, some achievements have been accomplished, contributing small pieces to the grand scientific jigsaw puzzle. The questions that have been answered by the experiments in which I have taken part are sometimes difficult to understand for the uninitiated, but our overall aim was to better understand the interactions between light and matter and to use this knowledge to facilitate new applications. Using the lasers at the High Power Laser Facility at the Lund Laser Centre, hard X-rays have been generated and studied in a research project that started already ten years ago. By taking another step forward and employing a compact laser system with a hundred times higher repetition rate (1 kHz), it has been found that medical imaging can readily be performed with acquisition times that may soon become realistic. The results are encouraging, showing that laser-produced X-rays might have a place in future diagnostic imaging. Furthermore, considerable effort has been devoted to initiating a new field of research, in which the channelling of light by means of relativistic effects has been investigated. This required developing a new, more powerful laser arm, based on the first ten-hertz laser. The new multi-terawatt arm has been equipped with advanced laser pulse diagnostic tools of several kinds, and a designated evacuated experimental chamber has been built and equipped for this new type of experiment. This effort has required all possible resources to be focused on this work for a long period of time, but finally relativistic channelling experiments are now carried out. The Lund High Power Laser Facility has now advanced into this new, fascinating field of science. In the first experiments performed, relativistic channels have been studied by optical measurement techniques and electrons accelerated inside the channels have been detected and characterized.

The same kind of experiments performed at the Lund High Power Laser Facility are being performed by a growing high-field

science community, and I would like to touch upon some of the research performed by this community as a whole. I believe we face a future in which high-field science will be of central importance not only to research, but also in an increasing number of applications. The work of the high-field science community is starting to overlap with existing research in higher energy physics communities, such as nuclear,[134–136] particle and astrophysics. For example, radionuclides that are used in medicine for treatment or diagnosis are presently produced at large accelerator facilities, sometimes far from the hospital. The half-lives of some of these radionuclides can be as short as a few minutes and it would be to great advantage if they could be produced in the vicinity of, or even at, the hospital. Laser-accelerated electrons, which require only a relatively small laser system, could very well be used to activate such radionuclides in the future.[137,138]

A new aspect of intense laser pulses focused onto solid targets has recently become a "hot topic" in our community. It has been found that by focusing onto a thin solid, a beam of energetic protons can be ejected from the back of the target.[139–142] The mechanisms are not yet fully understood, but it is clear that the proton beam is of high quality. Proton beams find uses, for example, in medicine, in the treatment of cancer.[143–145]

Laser-accelerated electrons and protons can be emitted in a beam of high quality, e.g. short pulses and small divergence and they can be applied to many fields of science. A multitude of ideas have spawned experiments and investigations aimed at facilitating the introduction of this new particle source into many fields of science. In particular, the particle acceleration community is showing a growing interest. Laser-accelerated particles could provide a source of ultrashort particle bunches, which can be injected into conventional accelerators. Relativistic channels could perhaps also be used to further accelerate such bunches of particles. Today, accelerator technology has been pressed to its limits. The electric field should be as high as possible to reduce the distance needed for acceleration. However, the required distance sometimes exceeds several kilometres. A plasma, however, can support tremendous electric fields, several thousand times stronger than the upper limit for conventional accelerators; effectively reducing the required acceleration distance by the same amount. It is conceivable that one long or several consecutive plasma channels could replace or at least complement existing accelerators.

Not only can laser-based acceleration improve existing accelerator technology. For example, experiments with high-energy pions in storage rings require rapid acceleration of the particles to relativistic energies on times shorter than the lifetime of the pion of $\sim 10^{-8}$ s. This is not possible using conventional technology but if it could be done, relativistic time dilation would increase the lifetime and experiments could be performed. A laser-based

accelerator could facilitate the required near-instantaneous acceleration of pions to relativistic energies where the particles live much longer.[145] The pions could subsequently be injected into conventional accelerators and be accelerated further.

In several experiments neutrons have been produced by focusing laser pulses onto deuterium targets. In the generated plasma fusion occurs and energetic neutrons with an energy of a few MeV are emitted.[73,75,146,147] The EC is currently planning a large-scale neutron facility, the European Spallation Source (ESS), and it is easy to envisage the impact a compact, laser-based neutron source would have.

Presently, France and the USA are devoting considerable efforts to investigating the use of short-pulse lasers in laboratory inertial fusion experiments in the so-called "fast ignitor scheme".[145,148] The idea is to simultaneously focus about two hundred very powerful, energetic laser pulses onto a pellet made of from deuterium and tritium. The pulses, which are of nanosecond duration, ionize the pellet shell and compress it. Even the pressure of all of these beams can not suffice to raise the temperature to the level required for fusion. However, a very intense, ultrashort laser pulse could be able to penetrate far into the plasma through relativistically induced transparency and direct a beam of energetic electrons, or protons, into the pellet core, thereby starting the fusion process; i.e. "igniting" it.

In the distant future of high-field science it might even be possible to generate electromagnetic fields that can generate electron-positron pairs directly in vacuum (the laser-based production of electron-positron pairs has already been achieved, but in the presence of heavy nuclei[149,150]), however this requires an irradiance of the order of 10^{30} W/cm^2.[12] At an irradiance a few orders of magnitude lower, $> 10^{26}$ W/cm^2, the acceleration of electrons would already be tremendous, allowing the electrons to "sense" their event horizon, similar to how the horizon appears in the vicinity of black holes. The irradiance needed for this is, in principle, possible with the technology available today and would facilitate astrophysical simulation experiments.[12] (Today, the largest laser systems produce up to 10^{21} W/cm^2.)

The Author's Contribution

Here, I will try to define, in broad terms, my contribution to the work presented in Papers I – VI.

Paper I: J. Larsson and A. Sjögren.

"Evaluation of Laser-irradiated Ar Clusters..."

The experiment that led to this paper was performed in the spring of 1998, i.e. a few months after I came to the Division. I took part in the experiment, including the set-up, and helped with data evaluation and the preparation of the manuscript.

Paper II: E. Andersson *et al.*.

"Coronary Angiography Using Laser Plasma Sources..."

This experiment was carried out in the autumn of 1998. M. Grätz and I were responsible for the experimental set-up, as far as the laser and X-ray generation set-up. I also performed calculations for the absolute calibration of the CCD camera and helped to write the manuscript.

Paper III: C. Delfin *et al.*.

"Influence of Laser Pulse Duration on Relativistic..."

These were the first results on relativistic channelling performed at the Lund High Power Laser Facility. A huge amount of work preceded the publication, in which I was considerably involved, including a part of the design and upgrading of the ten-hertz multi-terawatt arm that was used in this experiment. Alignment of the compressor in the evacuated chamber, constructing a part of the vacuum system and adding an optical table with diagnostic equipment for the laser were also major contributions. The experimental set-up was built and tested in various ways, before the experiment was carried out in the autumn of 2000. C. Delfin wrote the first draft of the manuscript, I was very active in the preparation of the final manuscript, including evaluation and interpretation of data.

Paper IV: A. Sjögren *et al.*.

"Relativistic Channel Formation..."

Some of the measurements reported in this paper were planned by me and performed in the summer of 2001, and some results came from earlier measurements. The 0.5 mm orifice of the gas nozzle had been replaced by a larger, 0.8 mm orifice, and longer

channels were measured. A toroidal coil, designed to measure the total charge of the forward accelerated electrons from the relativistic channels, was used for the first time. I designed and tested the coil and performed the analysis of the electron charge measurements and also wrote the manuscript.

PAPER V: A. Sjögren *et al.*.

"High-Repetition-Rate, Hard X-ray Radiation..."

This experiment was planned by me, but M. Harbst helped considerably in carrying it out. The work included some laser re-design. I was responsible for the setting up of laser and X-ray diagnostic tools as well as the X-ray generation device. I performed the data analysis, including simulating the detected spectra. The manuscript was written by me, with various input from the coauthors.

PAPER VI: J. Larsson *et al.*.

"Picosecond X-ray Diffraction Studies..."

Two experiments led by J. Larsson, one in 1999 and another one year later, preceded this paper. I took parts in both experiments. Before the second experiment I spent quite some time before travelling to the ESRF preparing equipment. I was very active in setting up the various laser beams used in the experiments. Furthermore, I contributed to the setting up of the crystal samples and the detection equipment and took an active part in all measurements.

Acknowledgements

I would like to deeply thank my supervisors, Claes-Göran Wahlström and Sune Svanberg, for letting me become part of the Atomic Physics Division in Lund. Being there has changed me in more ways than I can explain. It has been a time of continuous improvement, for me as a person and as a scientist, where "truth" upon "truth" has been overthrown in the light of new knowledge and new insights.

For me, entering science has been a little like stepping into a crank rowing boat, knowing only that I have to end up on the other side of the lake four and a half years later. On the way there, I have caught fish I didn't believe existed and I have opened my luggage only to sometimes realize that the contents were wrong. During storms I have survived thanks to the support of my colleagues, friends and, of course, my beloved wife.

I will always remember with fondness those late nights at the lab, driven by enthusiasm, when suddenly everything worked, the friendly discussions in "Laila's café", and throughout it all: the ten-hertz ticking of the laser's high-voltage units...

Tick for a fantastic time at the Atomic Physics Division

Tack Claes-Göran and Sune, for your inexhaustible enthusiasm and resourcefulness

Tick for my newly found friends

Tack Johan, Christian, Matthias and Vladimir, for becoming dear friends

Tick for invaluable discussions and support

Thanks Ken and Mette, for caring for me in all weathers

Tick for difficult times by the laser

Tack Anders, for never saying no

Tick for a helping hand

Tack Michael, for working with me

Tick for very instructive times at the ESRF

Tack Jörgen, for giving me responsibilities

Tick for all the great times at the Division

Tack Lars, Niklas, Matthias, Tomas, Petter, Robert, Magnus and all the others, for being such great people

Tick for the backbone of the Division

Tack Laila and Marie, for your friendship and support

Tick for helping hands always being there

Tack Åke and Bertil; so helpful, so ready for fun

Tick for great times as a teacher

Tack the whole teaching department, for helping me become a better teacher

Tick for X-rayed rats, chickens, steaks, etc.

Tack Claes Olsson, for great discussions and help with image plates

Tick for people always putting up with me

Tack Bengt Erlandsson and Per Persson, for being ready to help when I needed you

Tick for an old-timer

Tack Carl Tillman, for showing such interest

Tick for friendship and fruitful cooperation

Danke Die fantastische Gruppe in Garching: George Tsakiris, Christoph Gahn, Georg Pretzler und Alexander Pukhov, weil Jeder von Ihnen so freundlich und hilfreich gewesen ist

You are all forever remembered in my heart.

Finally, I would like to thank my wife again, because without her, I don't think I could have successfully carried out this work.

Helen, I owe you everything

Appendix A

Relativistic Electron Motion

The relativistic motion of an electron in a plane wave of linearly polarized laser field is discussed here. First, the vector potential of the electromagnetic field is introduced. This quantity constitutes a joint description of the electric *and* the magnetic field. Thereafter, using relativistic particle dynamics, the vector potential is utilized to derive constants of motion for the electron. These are then used to express the oscillatory (kinetic) energy of an electron in a laser field of a certain irradiance.

Generally, the kinetic energy of an electron is defined as,[23]

$$W_{\text{kin}} = m_e c^2 \left(\gamma - 1\right) \approx \frac{m_e |\mathbf{v}|^2}{2}, \tag{A.1}$$

where the approximation gives the non-relativistic kinetic energy for $v/c \ll 1$. The Lorentz factor can be expressed as,

$$\gamma^{-1} = \sqrt{1 - \frac{|\mathbf{v}|^2}{c^2}}, \tag{A.2}$$

or as,

$$\gamma = \sqrt{1 + \frac{|\mathbf{p}|^2}{m_e^2 c^2}}, \tag{A.3}$$

where $|\mathbf{p}| = m_e \gamma |\mathbf{v}|$.

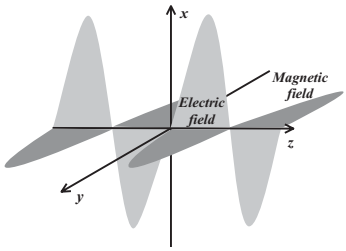

Figure A.1. *Orientation of electric and magnetic fields.*

Consider the situation in Figure A.1, with a linearly polarized laser field propagating along the z direction, $\mathbf{E}(z,t) = \hat{\mathbf{x}} E_0 \cos(\omega t - kz)$ and $\mathbf{B}(z,t) = \hat{\mathbf{y}} \frac{E_0}{c} \cos(\omega t - kz)$. The vector potential is defined as,[151]

$$\nabla \times \mathbf{A} = \mathbf{B}, \tag{A.4}$$

which, in the case of a pure electromagnetic wave in a material without charges, also determines the electric field:[151]

$$\mathbf{E} = -\frac{\partial \mathbf{A}}{\partial t}. \tag{A.5}$$

The motion of an electron in the laser field given above is governed by:[23]

$$\frac{d\mathbf{p}}{dt} = -e\mathbf{E} - e\mathbf{v} \times \mathbf{B}. \tag{A.6}$$

We now multiply (A.6) by $\mathbf{v}$ and simplify to find the equation of (kinetic) energy for the oscillatory motion of the electron:

$$\frac{dW_{\mathrm{osc}}}{dt} = m_e c^2 \frac{d\gamma}{dt} = -e\mathbf{E} \cdot \mathbf{v}. \tag{A.7}$$

Eq. (A.6) can also be expressed in terms of the vector potential by inserting (A.4) and (A.5):

$$\frac{d\mathbf{p}}{dt} = e\,\frac{\partial \mathbf{A}}{\partial t} - e\mathbf{v} \times \nabla \times \mathbf{A}. \tag{A.8}$$

Using the relations $\mathbf{v}\times\nabla\times\mathbf{A} = \nabla\left(\mathbf{v}\cdot\mathbf{A}\right) - \left(\mathbf{v}\cdot\nabla\right)\mathbf{A}$ and $d\mathbf{A}/dt = \partial\mathbf{A}/\partial t + \left(\mathbf{v}\cdot\nabla\right)\mathbf{A}$ and then integrating the x and y parts of (A.8) gives the constants of motion for the x and y direction:[105]

$$\begin{aligned} p_x(z,t) &= eA_x(z,t) + p_{x0} \\ &= -\frac{eE_0}{\omega}\sin(\omega t - kz) + p_{x0} \qquad x \text{ direction}, \end{aligned} \tag{A.9}$$

$$p_y(z,t) = p_{y0} \qquad\qquad y \text{ direction}. \tag{A.10}$$

Here, $p_x = m_e\gamma v_x$ and $p_y = m_e\gamma v_y$. The motion of the electron before being overtaken by the laser field is determined by p_{x0} and p_{y0}. In the following, the electron is assumed to be initially motionless, i.e. $p_{x0} = p_{x0} = 0$.

To obtain the constant of motion for the z direction, we combine the z parts of (A.6) and (A.7) to yield:[105]

$$\frac{p_z(z,t)}{m_e c} = \gamma(z,t) - \gamma_0 \qquad z \text{ direction} \tag{A.11}$$

Introducing this equation (with $\gamma_0 = 1$, i.e. no initial movement) into the equation for kinetic energy, (A.1), gives,

$$W_{\mathrm{osc}}(z,t) = m_e c^2\left(\gamma(z,t) - 1\right) = cp_z(z,t), \tag{A.12}$$

or, by using the relation in (A.2) in conjunction with (A.11) yielding

$$p_z(z,t) = \frac{p_x^2(z,t)}{2m_e c}, \tag{A.13}$$

it can be found that:

$$W_{\mathrm{osc}}(z,t) = \frac{p_x^2(z,t)}{2m_e}. \tag{A.14}$$

From (A.14), using (A.9), the electron's maximum oscillation energy can now be expressed as a function of the irradiance, $I = \frac{1}{2}\varepsilon_0 c E_0^2$:

$$W_{\text{osc}}\big|_{\text{max}} = \frac{e^2}{4\pi^2\varepsilon_0 m_e c^3}\, I\, \lambda^2. \tag{A.15}$$

The *average* energy is often more applicable, but it is difficult to calculate exactly. However, neglecting the variation in z in (A.9), (A.15) can be used to find the approximate oscillatory energy over one oscillation period of the light wave:

$$\langle W_{\text{osc}} \rangle \simeq \frac{e^2}{8\pi^2\varepsilon_0 m_e c^3}\, I\, \lambda^2. \tag{A.16}$$

It can expressed in a more useful form, $\langle W_{\text{osc}} \rangle = 93\, I_{18}\, \lambda_{\mu\text{m}}^2$ keV, with the irradiance, I_{18}, in units of 10^{18} W/cm^2 and the wavelength, $\lambda_{\mu\text{m}}$, in units of μm. Furthermore, $\langle \gamma \rangle$ can be calculated as

$$\langle \gamma \rangle - 1 = \frac{\langle W_{\text{osc}} \rangle}{m_e c^2} \simeq \frac{e^2}{8\pi^2\varepsilon_0 m_e c^3}\, I\, \lambda^2. \tag{A.17}$$

This can also be expressed in more useful forms: $\langle \gamma \rangle - 1 = 0.18\, I_{18}\, \lambda_{\mu\text{m}}^2$ or $\langle \gamma \rangle - 1 = \langle W_{\text{osc}} \rangle$ [keV]/512, with similar notation as above.

The expression in (A.16) turns out to be equal to that of the well-known ponderomotive potential for non-relativistic electron movement, often denoted U_p. The non-relativistic derivation excludes the action of the magnetic field and concentrates on the transverse movement of the electrons, but in the derivation above, the magnetic field is included. This means that the electron moves along the pulse axis of propagation and the average energy in (A.16) includes contributions from both longitudinal and transverse electron movement. Calculating the equivalence of the ponderomotive potential in the relativistic regime for a laser pulse focusing into a dense plasma is *utterly* complicated.[11,152–154] Considering this, the expression in (A.16), derived under quite limiting conditions, should be used with caution.

Appendix B

The Toroidal Coil Circuit

The toroidal coil was used in the experiments dealing with relativistic channelling. The idea behind the circuit design is to allow accelerated electrons to pass through the coil, which is illustrated in Figure 4.29. By studying the oscillating response of the toroidal coil circuit to the passage of the electrons the total charge of the electrons can be estimated.

The coil is connected to a circuit as shown in Figure B.1; L_T is the inductance of the toroid, and R_c and C_c represent the resistance and capacitance of the cables, and $C_{\rm osc}$ and $R_{\rm osc}$ the capacitance and resistance of the oscilloscope (Table B.1). The electrons induce a resonant oscillation in the circuit, the voltage of which, $u_{\rm osc}$, is viewed on the screen of the oscilloscope.

The toroid diameter is $\Phi = 14.5$ cm and the wound coil has a diameter of $\varphi = 17$ mm. Twenty turns of copper wire are wound around a hollow plastic tube that supports the device. The inductance of the toroidal coil can now be estimated according to:

$$L_T = \frac{\mu_r \mu_0}{\pi \Phi} \cdot N^2 \cdot \pi \left(\frac{\varphi}{2}\right)^2 \approx \frac{\mu_0 \varphi^2}{4\Phi} \cdot N^2 = 0.25\ \mu\text{H}, \qquad \text{(B.1)}$$

The measured inductance was found to be 1.1 μH. Considering the crudeness of the coil, this is quite close to the theoretical value. The inductance should be compared with the typical inductance of a doubly screened coaxial cable, which is about 250 μH per metre of the cable that is used.

By employing the Laplace transform, the complete expression for the response of $u_{\rm osc}$ to an "infinitely short" electron pulse with total charge Q_e can be calculated. Furthermore, it can be shown that with the parameters listed in Table B.1, the calculated response can be approximated by:

$$u_{osc}(t) \simeq -\frac{Q_e}{NC_{\rm tot}} \exp\left(-R_c t / L_T\right) \cos\left[t\sqrt{L_T C_{\rm tot}}\right] \qquad \text{(B.2)}$$

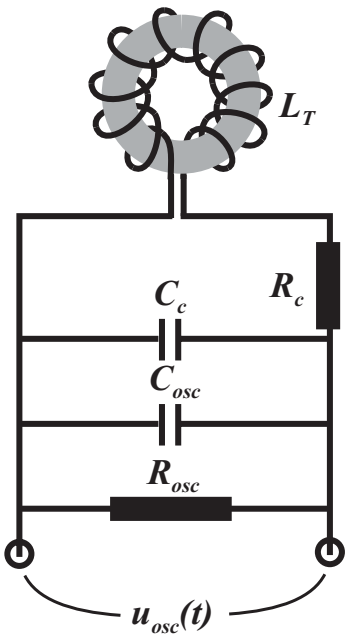

Figure B.1. *The electronic circuit to which the toroidal coil is connected. $u_{\rm osc}$ represents the voltage seen on the oscilloscope screen.*

Table B.1. *The circuit parameters.*

L_T	1.1 μH
R_c	2 Ω
C_c	35 pF
$C_{\rm osc}$	280 pF
$R_{\rm osc}$	1 MΩ

This is a damped oscillation where the amplitude is proportional to Q_e, i.e. the total charge of the electron pulse. Since the oscillation period, ~ 0.12 μs, is much shorter than the decay, ~ 1.2 μs, the oscilloscope can be used to measure the amplitude of the oscillation at time zero, and determine the total charge of the electrons.

Bibliography

1. P. M. W. French. Ultrafast solid-state lasers. *Contemporary Physics*, 37:283–301, 1996.
2. M. D. Perry and G. Mourou. Terawatt to petawatt subpicosecond lasers. *Science*, 264:917–924, 1994.
3. D. Hulin. OECD global science forum. Scope of the workshop., 2001. URL `http://www.oecd.org/ppt/M00020000/M00020063.ppt`.
4. G. Pretzler, A. Kasper, and K. J. Witte. Angular chirp and tilted light pulses in CPA lasers. *Appl. Phys. B*, 70:1–9, 2000.
5. F. Eggenstein, F. Senf, T. Zeschke, and W. Gudat. Cleaning of contaminated XUV-optics at BESSY II. *Nucl. Instrum. and Meth. A*, 467-468: 325–328, 2001.
6. A. E. Siegman. *Lasers*. University Science Books, 55D Gate Five Road, Sausalito, CA 94965, 1986.
7. S. Augst, D. Strickland, D. D. Meyerhofer, S. L. Chin, and J. H. Eberly. Tunneling ionization of noble gases in a high-intensity laser field. *Phys. Rev. Lett.*, 63:2212–2215, 1989.
8. D. F. Gordon, B. Hafizi, P. Sprangle, R. F. Hubbard, J. R. Peñano, , and W. B. Mori. Seeding of the forward Raman instability by ionization fronts and Raman backscatter. *Phys. Rev. E*, 64:046404, 2001.
9. A. Pukhov and J. Meyer-Ter-Vehn. Relativistic laser-plasma interaction by multi-dimensional particle-in-cell simulations. *Phys. Plasmas*, 5: 1880–1886, 1998.
10. A. Pukhov, Z.-M. Sheng, and J. Meyer-Ter-Vehn. Particle acceleration in relativistic laser channels. *Phys. Plasmas*, 6:2847–2854, 1999.
11. F. V. Hartemann, S. N. Fochs, G. P. Le Sage, Jr. N. C. Luhmann, J. G. Woodworth, M. D. Perry, and Y. J. Chen. Nonlinear ponderomotive scattering of relativistic electrons by an intense laser field at focus. *Phys. Rev. E*, 51:4833–4843, 1995.
12. T. Tajima and G. Mourou. Superstrong field science. In M. Lontano, G. Mourou, O. Svelto, and T. Tajima, editors, *Superstrong fields in plasmas: Second Int'l. Conf.*, volume 611, pages 423–436, New York, USA, 2002. American Institute of Physics.
13. D. F. Price, R. M. More, R. S. Walling, G. Guethlein, R. L. Shepherd, R. E. Stewart, and W. E. White. Absorption of ultrashort laser pulses by solid targets heated rapidly to temperatures 1-1000 eV. *Phys. Rev. Lett.*, 75:252–255, 1995.
14. A. Ng, P. Celliers, A. Forsman, R. M. More, Y. T. Lee, F. Perrot, M. W. C. Dharma-Wardana, and G. A. Rinker. Reflectivity of intense femtosecond laser pulses from a simple metal. *Phys. Rev. Lett.*, 72:3351–3354, 1994.
15. J. D. Kmetec, C. L. Gordon, J. J. Macklin, B. E. Lemoff, G. S. Brown, and S. E. Harris. MeV x-ray generation with a femtosecond laser. *Phys. Rev. Lett.*, 68:1527–1530, 1992.
16. E. Hecht. *Optics*. Addison-Wesley Publishing Company, Reading, USA, 1987.

17. F. L. S. J. Pedrotti and L. S. Pedtrotti. *Introduction to optics*. Prentice-Hall, Inc., NJ 07632, USA, 1993.
18. W. L. Kruer. *The Physics of Laser Plasma Interactions*. Addison-Wesley, New York, 1988.
19. P. Gibbon and E. Förster. Short-pulse laser-plasma interactions. *Plasma Phys. Control. Fusion*, 38:769–793, 1996.
20. D. W. Forslund, J. M. Kindel, and K. Lee. Theory of hot-electron spectra at high laser intensity. *Phys. Rev. Lett.*, 39:284–288, 1977.
21. U. Teubner, J. Bergmann, B. Van Wonterghem, F. P. Schäfer, and R. Sauerbrey. Angle-dependent x-ray emission and resonance absorption in a laser-produced plasma generated by a high intensity ultrashort pulse. *Phys. Rev. Lett.*, 70:794–797, 1993.
22. F. F. Chen. *Introduction to Plasma Physics and Controlled Fusion*, volume 1: Plasma Physics. Plenum Press, New York, USA, 2:nd edition, 1984.
23. J. Meyer-Ter-Vehn, A. Pukhov, and Zh.-M. Sheng. Relativistic laser plasma interaction. In D. Batani, C. J. Joachain, S. Martellucci, and A. N. Chester, editors, *Atoms, Solids, and Plasmas in Super-Intense Laser Fields*, pages 167–192. Kluwer Academic/Plenum Publishers, New York, USA, 2001.
24. G. H. McCall. Calculation of x-ray Bremsstrahlung and characteristic line emission produced by a Maxwellian electron distribution. *J. Phys. D*, 15:823–831, 1982.
25. M. J. Berger, J. H. Hubbell, S. M. Seltzer, J. S. Coursey, and D. S. Zucker. Physical reference data, x-ray and gamma-ray data (version 1.2), [online]. Technical report, National Institute of Standards and Technology, 1999. URL `http://physics.nist.gov/xcom`.
26. R. D. Evans. *The Atomic Nucleus*. McGraw-Hill Book Company, New York, USA, 1955.
27. M. Grätz. *Characterisation and Application of a Laser-Based Hard X-Ray Source*. PhD thesis, Lund Institute of Technology, LRAP-236, 1998.
28. K. Herrlin, G. Svahn, C. Olsson, H. Petterson, C. Tillman, A. Persson, C.-G. Wahlström, and S. Svanberg. The generation of X-rays for medical imaging by high-power lasers - present and future applications - preliminary results. *Radiology*, 189:65, 1993.
29. C. Tillman, A. Persson, C.-G. Wahlström, S. Svanberg, and K. Herrlin. Imaging using hard X-rays from a laser-produced plasma. *Appl. Phys. B*, 61:333–338, 1995.
30. K. O. Herrlin, C. Tillman, C. Olsson, H. T. Pettersson, G. Svahn, and S. Svanberg. Contrast-enhanced radiography with differetial absoprtion by using a laser-produced x-ray source. *Radiology*, 197:357–357 Suppl. S, 1995.
31. C. Tillman. *Development and Characterisation of a Laser-Based Hard X-Ray Source*. PhD thesis, Lund Institute of Technology, LRAP-204, 1996.
32. S. Svanberg, S. Andersson-Engels, R. Cubeddu, E. Förster, M. Grätz, K. Herrlin, G. Hölzer, L. Kiernan, C. Af Klinteberg, A. Persson, A. Pifferi, A. Sjögren, and C.-G. Wahlström. Generation, characterization, and medical utilization of laser-produced emission continua. *Laser Part. Beams*, 18:563–570, 2000.
33. C. Tillman, I. Mercer, S. Svanberg, and K. Herrlin. Elemental biological imaging by differential absorption with a laser-produced x-ray source. *J. Opt. Soc. Am. B*, 13:209–215, 1996.
34. K. Herrlin, C. Tillman, M. Grätz, C. Olsson, H. Pettersson, G. Svahn, C.-G. Wahlström, and S. Svanberg. Contrast-enhanced radiography by differential absorption, using a laser-produced x-ray source. *Inv. Rad.*, 32:306–310, 1997.
35. M. Grätz, A. Pifferi, C.-G. Wahlström, and S. Svanberg. Time-gated imaging in radiology: Theoretical and experimental studies. *IEEE J. Sel. Top. Quant. El.*, 2:1041–1048, 1996.

36. M. Grätz, A. Pifferi, C. Tillman, C.-G. Wahlström, and S. Svanberg. Propagation of laser-produced short x-ray pulses through scattering media: Application to scatter-reduced medical imaging. *X-ray Lasers 1996 Inst. of Phys. Conf. Ser.*, 151:539–541, 1996.
37. M. Grätz, L. Kiernan, C.-G. Wahlström, S. Svanberg, and K. Herrlin. Time-gated x-ray tomography. *Appl. Phys. Lett.*, 73:2899–2901, 1998.
38. M. Grätz, L. Kiernan, and K. Herrlin. Time-gated imaging in planar and tomographic x-ray imaging. *Med. Phys.*, 26:438–446, 1999.
39. C. Tillman, G. Grafström, A. C. Jonsson, B. A. Jonsson, I. Mercer, S. Mattsson, S. E. Strand, and S. Svanberg. Survival of mammalian cells exposed to ultrahigh dose rates from a laser-produced plasma x-ray source. *Radiology*, 213:860–865, 1999.
40. G. Hölzer, E. Förster, M. Grätz, C. Tillman, and S. Svanberg. X-ray crystal spectroscopy of sub-picosecond laser-produced plasmas beyond 50 keV. *J. X-ray Sci. Technol.*, 7:50–70, 1997.
41. C. Tillman, S. A. Johansson, B. Erlandsson, M. Grätz, B. Hemdal, A. Almén, S. Mattsson, and S. Svanberg. High-resolution spectroscopy of laser-produced plasmas in the photon energy range above 10 keV. *Nucl. Instrum. Meth. Phys. Res. A*, 394:387–396, 1997.
42. G. Svahn. *Diagnostic X-Ray Spectra*. PhD thesis, Lund University, 1977.
43. G. Pretzler, T. Schlegel, E. Fill, and D. Eder. Hot-electron generation in copper and photopumping of cobalt. *Phys. Rev. E*, 62:5618–5623, 2000.
44. G. Pretzler, T. Schlegel, and E. Fill. Characterization of electron beam propagation through foils by innershell x-ray spectroscopy. *Laser Part. Beams*, 19:91–97, 2001.
45. K. Estabrook and W. L. Kruer. Properties of resonantly heated electron distributions. *Phys. Rev. Lett.*, 40:42–45, 1978.
46. P. Gibbon. Efficient production of fast electrons from femtosecond laser interaction with solid targets. *Phys. Rev. Lett.*, 73:664–667, 1994.
47. G. Ferrante, M. Zarcone, and S. A. Uryupin. Inverse Bremsstrahlung in a plasma with electron temperature anisotropy. *Phys. Plasmas*, 8: 4745–4752, 2001.
48. F. N. Beg, A. R. Bell, A. E. Dangor, C. N. Danson, A. P. Fews, M. E. Glinsky, B. A. Hammel, P. Lee, P. A. Norreys, and M. Tatarakis. A study of picosecond laser-solid interactions up to 10^{19} Wcm^{-2}. *Phys. Plasmas*, 4:447–457, 1996.
49. M. Lamoureux, P. Waller, P. Charles, and N. B. Avdonina. Bremsstrahlung from thick targets and a diagnostic for electron energy distributions. *Phys. Rev. E*, 62:4091–4095, 2000.
50. S. Bastiani, P. Audebert, J. P. Geindre, T. Schlegel, J. C. Gauthier, C. Quoix, G. Hamoniaux, G. Grillon, and A. Antonetti. Hot-electron distribution functions in a subpicosecond laser interaction with solid targets of varying initial gradient scale lengths. *Phys. Rev. E*, 60:3439–3442, 1999.
51. L. M. Chen, J. Zhang, Q. L. Dong, H. Teng, T. J. Liang, L. Z. Zhao, and Z. Y. Wei. Hot electron generation via vacuum heating process in femtosecond laser-solid interactions. *Phys. Plasmas*, 8:2925–2929, 2001.
52. A. B. Langdon. Nonlinear inverse Bremsstrahlung and heated-electron distributions. *Phys. Rev. Lett.*, 44:575, 1980.
53. W. Rozmus and V. T. Tikhonchuk. Skin effect and interaction of short laser pulses with dense plasmas. *Phys. Rev. A*, 42:7401–7412, 1990.
54. G. J. Pert. Inverse Bremsstrahlung in strong radiation fields at low temperatures. *Phys. Rev. E*, 51:4778–4789, 1995.
55. P. Gibbon and A. R. Bell. Collisionless absorption in sharp-edged plasmas. *Phys. Rev. Lett.*, 68:1535–1538, 1992.
56. F. Brunel. Not-so-resonant, resonant absorption. *Phys. Rev. Lett.*, 59: 52–55, 1987.
57. P. B. Corkum. Plasma perspective on strong-field multiphoton ionization. *Phys. Rev. Lett.*, 71:1994–1197, 1993.
58. K. S. Budil, P. Salières, A. L'Huillier, T. Ditmire, and M. D. Perry.

Influence of ellipticity on harmonic generation. *Phys. Rev. A*, 48:R–3437–R3440, 1993.

59. J. J. Macklin, J. D. Kmetec, and C. L. Gordon III. High-order harmonic generation using intense femtosecond pulses. *Phys. Rev. Lett.*, 70:766–769, 1993.
60. C.-G. Wahlström, J. Larsson, A. Persson, T. Starczewski, S. Svanberg, P. Salières, Ph. Balcou, and A. L'Huillier. High-oder harmonic generation in rare gases with an intense short-pulse laser. *Phys. Rev. A*, 48:4709–4720, 1993.
61. A. B. Langdon, B. F. Lasinski, and W. L. Kruer. Nonlinear saturation and recurrence of the two-plasmon decay instability. *Phys. Rev. Lett.*, 43:133, 1979.
62. R. E. Turner, D. W. Phillion, B. F. Lasinski, and E. M. Campbell. Half and three-halves harmonic measurements from laser-produced plasmas. *Phys. Fluids*, 27:511, 1984.
63. P. D. Carter, S. M. L. Sim, H. C. Barr, and R. G. Evans. Time-resolved measurements of the three-halves harmonic spectrum from laser-produced plasmas. *Phys. Rev. Lett.*, 44:1407, 1980.
64. R. L. Keck, R. L. McCrory, W. Seka, and J. M. Soures. Absorption physics at 351 nm in spherical geometry. *Phys. Rev. Lett.*, 54:1656, 1985.
65. Q. L. Dong, J. Zhang, and H. Teng. Absorption of femtosecond laser pulses in interaction with solid targets. *Phys. Rev. E*, 64:026411, 2001.
66. E. G. Gamaliy and R. Dragila. Interaction of ultrashort laser pulses at relativistic intensities with solid targets: Relativistic skin effect. *Phys. Rev. A*, 42:929–935, 1990.
67. P. P. Rajeev, S. Banerjee, A. S. Sandhu, R. C. Issac, L. C. Tribedi, and G. R. Kumar. Role of surface roughness in hard-x-ray emission from femtosecond-laser-produced copper plasmas. *Phys. Rev. A*, 65:052903, 2002.
68. R. Fedosejevs, R. Ottmann, R. Sigel, G. Kühnle, S. Szatmari, and F. P. Schäfer. Absorption of femtosecond laser pulses in high-density plasma. *Phys. Rev. Lett.*, 64:1250–1253, 1990.
69. C. Rose-Petruck, R. Jimenez, T. Guo, A. Cavalleri, C. W. Siders, F. Rksi, J. A. Squier, B. C. Walker, K. R. Wilson, and C. P. J. Barty. Picosecond-milliångström lattice dynamics measured by ultrafast x-ray diffraction. *Nature*, 398:310 – 312, 1999.
70. G. Korn, A. Thoss, H. Stiel, U. Vogt, M. Richardson, T. Elsaesser, and M. Faubel. Ultrashort 1-kHz laser plasma hard x-ray source. *Opt. Lett.*, 27:866–868, 2002.
71. D. von der Linde, K. Sokolowski-Tinten, Ch. Blome, C. Dietrich, A. Tarasevitch, A. Cavalleri, and J. A. Squier. Femtosecond time resolution in x-ray spectroscopy. *Superstrong Fields in Plasmas, AIP Conference Proc.*, 611:63–74, 2002.
72. M. Grätz, C. Tillman, I. Mercer, and S. Svanberg. X-ray generation for medical applications from a laser-produced plasma. *Appl. Surf. Sci.*, 96: 443–447, 1996.
73. G. Pretzler, A. Saemann, A. Pukhov, D. Rudolph, T. Schätz, U. Schramm, P. Thirolf, D. Habs, K. Eidmann, G. D. Tsakiris, J. Meyer-Ter-Vehn, and K. J. Witte. Neutron production by 200 mJ ultrashort laser pulses. *Phys. Rev. E*, 58:1165–1168, 1998.
74. G. Malka, J. Fuchs, F. Amarinoff, S. D. Baton, R. Gaillard, J. L. Miquel, H. Pépin, C. Rousseaux, G. Bonnaud, M. Busquet, and L. Lours. Suprathermal electron generation and channel formation by an ultrarelativistic laser pulse in an underdense preformed plasma. *Phys. Rev. Lett.*, 79:2053–2056, 1997.
75. H. Schwoerer, P. Gibbon, S. Dusterer, R. Behrens, C. Ziener, C. Reich, and R. Sauerbrey. MeV x rays and photoneutrons from femtosecond laser-produced plasmas. *Phys. Rev. Lett.*, 86:2317–2320, 2001.
76. H. L. Andersson, R. B. Lindsay, L. W. Fredrick, C. F. Barnett, W. L.

Wiese, G. A. Martin, H. Frauenfelder, M. C. Marden, R. J. Donnelly, G. A. Jeffrey, R. L. Kelly, A. H. Rosenfeld, A. K. Meier, H. A. Bethe, R. K. Eby, T. N. Padikal, M. D. Harmony, J. K. Tuli, S. Pearlstein, J. N. Howard, D. L. Book, H. Markovitz, H. P. R. Frederikse, H. D. Hagstrum, and Y. S. Touloukian, editors. *AIP 50th Anniversary, Physics Vade Mecum*. American Institute of Physics, NY 10017, USA, 1981.

77. T. Wilhein. *Charakterisierung und Anwendungen im Bereich Weicher Röntgenstrahlung*. PhD thesis, Georg-August-Universität, Göttingen, 1994.
78. J. Kirz, D. T. Attwood, B. L. Henke, M. R. Howells, K. D. Kennedy, K.-J. Kim, J. B. Kortright, R. C. Perera, P. Pianetta, J. C. Riordan, J. H. Scofield, G. L. Stradling, A. C. Thompson, J. H. Underwood, G. P. Williams, and H. Winick. X-ray data booklet, 1986.
79. J. Larsson, P. A. Heimann, A. M. Lindenberg, P. J. Schuck, P. H. Bucksbaum, R. W. Lee, H. A. Padmore, J. S. Wark, and R. W. Falcone. Ultrafast structural changes measured by time-resolved x-ray diffraction. *Appl. Phys. A*, 66:587–591, 1998.
80. A. M. Lindenberg, I. Kang, S. L. Johnson, T. Missalla, P. A. Heimann, Z. Chang, J. Larsson, P. H. Bucksbaum, H. C. Kapteyn, H. A. Padmore, R. W. Lee, J. S. Wark, and R. W. Falcone. Time-resolved x-ray diffraction from coherent phonons during a laser-induced phase transition. *Phys. Rev. Lett.*, 84:111–114, 2000.
81. T. Ditmire, T. Donnelly, A. M. Rubenchik, R. W. Falcone, and M. D. Perry. Interaction of intense laser pulses with atomic clusters. *Phys. Rev. A*, 53:3379–3402, 1996.
82. R. Neutze and J. Hajdu. Femtosecond time resolution in x-ray diffraction experiments. *Proc. Natl. Acad. Sci. USA*, 94:5651–5655, 1997.
83. R. Neutze, R. Wouts, D. Van der Spoel, E. Weckert, and J. Hajdu. Potential for biomolecular imaging with femtosecond x-ray pulses. *Nature*, 406:752–757, 2000.
84. J. Hajdu. Single-molecule x-ray diffraction. *Cur. Opinion Struct. Biology*, 10:569–573, 2000.
85. C. Thomsen, H. T. Grahn, H. J. Maris, and J. Tauc. Surface generation and detection of honons by picosecond light pulses. *Phys. Rev. B*, 34: 4129–4138, 1986.
86. R. W. Shoenlein, W. P. Leemans, A. H. Chin, P. Volfbeyn, T. E. Glover, P. Balling, M. Zolotorev, K.-J. Kim, S. Chattopadhyay, and C. V. Shank. Femtosecond x-ray pulses at 0.4 á generated by 90° thomson scattering: A tool for probing the structural dynamics of materials. *Science*, 274: 236–238, 1996.
87. C. Rischel, A. Rousse, I. Uschmann, P.-A. Albouy, J.-P. Geindre, P. Audebert, J.-C. Gauthier, J.-L. Martin E. Förster, and A. Antonetti. Femtosecond time-resolved x-ray diffraction from laser-heated organic films. *Nature*, 390:490 – 492, 1997.
88. A. Rousse, C. Rischel, S. Fourmaux, I. Uschmann, S. Sebban, G. Grillon, Ph. Balcou, E. Förster, J.P. Geindre, P. Audebert, J.C. Gauthier, and D. Hulin. Non-thermal melting in semiconductors measured at femtosecond resolution. *Nature*, 410:65 – 68, 2001.
89. F. Albert, A. Sjögren, C.-G. Wahlstrom, S. Svanberg, C. Olsson, and H. Merdji. Laser produced x-ray source in the 10-60 keV range at 1 kHz. modified irradiation schemes in order to reach medical imaging quality. *J. DE PHYSIQUE IV*, 11:429–432, 2001.
90. C. L. Gordon III, G. Y. Yin, B. E. Lemoff, P. M. Bell, and C. P. J. Barty. Time-gated imaging with an ultrashort-pulse, laser-produced-plasma x-ray source. *Opt. Lett.*, 20:1056–1058, 1995.
91. C. Gahn, G. D. Tsakiris, A. Pukhov, J. Meyer-Ter-Vehn, G. Pretzler, P. Thirolf, D. Habs, and K. J. Witte. Multi-MeV Electron Beam Generation by Direct Laser Acceleration in High-Density Plasma Channels. *Phys. Rev. Lett.*, 83:4772–4775, 1999.
92. M. I. K. Santala, Z. Najmudin, E. L. Clark, M. Tatarakis, K. Krushel-

nick, A. E. Dangor, V. Malka, J. Faure, R. Allott, , and R. J. Clarke. Observation of a hot high-current electron beam from a self-modulated laser wakefield accelerator. *Phys. Rev. Lett.*, 86:1227–1230, 2001.
93. V. Malka, J. Faure, J. R. Marques, F. Amiranoff, J. P. Rousseau, S. Ranc, J. P. Chambaret, Z. Najmudin, B. Walton, P. Mora, and A. Solodov. Characterization of electron beams produced by ultrashort (30 fs) laser pulses. *Phys. Plasmas*, 8:2605–2608, 2001.
94. D. Giulietti, M. Galimberti, A. Giulietti, L. A. Gizzi, R. Numico, P. Tomassini, M. Borghesi, V. Malka, S. Fritzler, M. Pittman, K. Ta Phouc, and A. Pukhov. Production of ultracollimated bunches of multi-MeV electrons by 35 fs laser pulses propagating in exploding-foil plasmas. *Phys. Plasmas*, 9:3655–3658, 2002.
95. N. H. Burnett and P. B. Corkum. Cold plasma production for recombination extreme-ultraviolet lasers by optical field induced ionization. *J. Opt. Soc. Am. B*, 6:1195–1199, 1989.
96. P. Amendt, D. C. Eder, and S. C. Wilks. X-ray lasing by optical-field-induced ionization. *Phys. Rev. Lett.*, 66:2589–2592, 1991.
97. G.-Z. Sun, E. Ott, Y. C. Lee, and P. Guzdar. Self-focusing of short intense pulses in plasmas. *Phys. Fluids*, 30:526–532, 1987.
98. P. Sprangle, E. Esarey, and A. Ting. Nonlinear interaction of intense laser pulses in plasmas. *Phys. Rev. A*, 41:4463–4469, 1990.
99. E. Esarey, P. Sprangle, J. Krall, and A. Ting. Self-focusing and guiding of short laser pulses in ionizing gases and plasmas. *IEEE J. Quantum Elect.*, 33:1879–1914, 1997.
100. P. Sprangle, C.-M. Tang, and E. Esarey. Relativistic self-focusing of short pulse radiation beams in plasmas. *IEEE Trans. Plasma Sci.*, PS-15:145–153, 1987.
101. P. Sprangle, E. Esarey, and A. Ting. Nonlinear theory of intense laser-plasma interactions. *Phys. Rev. Lett.*, 64:2011–2014, 1990.
102. E. Esarey, S. K. Ride, and P. Sprangle. Nonlinear Thomson scattering of intense laser pulses from beams and plasmas. *Phys. Rev. E*, 48:3003–3021, 1993.
103. R. Fedosejevs, X. F. Wang, and G. D. Tsakiris. Onset of relativistic self-focusing in high density gas jet targets. *Phys. Rev. E*, 56:4615–4639, 1997.
104. P. Monot, T. Auguste, P. Gibbon, F. Jakober, G. Mainfray, A. Dulieu, M. Louis-Jacquet, and G. Malka Annd J. L. Miquel. Experimental demonstration of relativistic self-channeling of a multiterawatt laser pulse in and underdense plasma. *Phys. Rev. Lett.*, 74:2953–2956, 1995.
105. C. Gahn. *Erzeugung Relativistischer Elektronen Durch Propagation Hochintensiver Laserpulse in Einem Plasma.* PhD thesis, Max-Planck-Institut, 2000.
106. J. Faure, V. Malka, J.-R. Marquès, P.-G. David, F. Amarinoff, K. Ta Phuoc, and A. Rousse. Effects of pulse duration on self-focusing of ultrashort lasers in underdense plasmas. *Phys. Plasmas*, 9:756–759, 2002.
107. W. B. Mori, C. Joshi, J. M. Dawson, D. W. Forslund, and J. M. Kindel. Evolution of self-focusing of intense electromagnetic waves in plasma. *Phys. Rev. Lett.*, 60:1298–1301, 1988.
108. S.-Y. Chen, G. S. Sarkisov, A. Maksimchuk, R. Wagner, and D. Umstadter. Evolution of a plasma waveguide created during relativistic-ponderomotive self-channeling of an intense laser pulse. *Phys. Rev. Lett.*, 80:2610–2613, 1998.
109. G. S. Sarkisov, V. Yu. Bychenkov, V. T. Tikhonchuk, A. Maksimchuk, S.-Y. Chen, R. Wagner, G. Mourou, and D. Umstadter. Observation of the plasma channel dynamics and Coulomb explosion in the interaction of a high-intensity laser pulse with a He gas jet. *JETP Lett.*, 66:828–834, 1997.
110. E. S. Dodd and D. Umstadter. Coherent control of stimulated Raman scattering using chirped laser pulses. *Phys. Plasmas*, 8:3531–3534, 2001.
111. S. P. Le Blanc, M. C. Downer, R. Wagner, S.Y. Chen, A. Maksim-

chuk AndG. Mourou, and D. Umstadter. Temporal characterization of a self-modulated laser wakefield. *Phys. Rev. Lett.*, 77:5381–5384, 1996.
112. J. D. Jackson. *Classical Electrodynamics*. John Wiley and Sons, New York, USA, 1975.
113. A. Chiron, G. Bonnaud, A. Dulieu, J. L. Miquel, G. Malka, M. Louis-Jacquet, and G. Mainfray. Experimental observations and simulations on relativistic self-guiding of an ultra-intense laser pulse in underdense plasmas. *Phys. Plasmas*, 3:1373–1401, 1996.
114. D. F. Gordon, B. Hafizi, R. F. Hubbard, and P. Sprangle. Raman sidescatter in numerical models of short pulse laser plasma interactions. *Phys. Plasmas*, 9:1157–1163, 2002.
115. W. B. Mori. The physics of the nonlinear optics of plasmas at relativistic intensities for short-pulse lasers. *IEEE J. Quantum Elect.*, 33:1942–1953, 1997.
116. A. V. Borovsky, A. L. Galkin, V. V. Korobkin, and O. B. Shiryaev. Raman scattering and excitation of the harmonics of intense laser radiation in cold plasmas. *Phys. Rev. E*, 59:2253–2262, 1999.
117. X. F. Wang, R. Fedosejevs, and G. D. Tsakiris. Observation of Raman scattering and hard X-rays in short pulse interaction with high density hydrogen gas. *Opt. Comm.*, 146:363–370, 1998.
118. A. Ting, K. Krushelnick, H. R. Burris, A. Fisher, C. Manka, and C. I. Moore. Backscattered supercontinuum emission from high-intensity laser-plasma interactions. *Opt. Lett.*, 21:1096–1098, 1996.
119. T.-W. Yau, C.-J. Hsu, H.-H. Chu, Y.-H. Chen, J. Wang, and S.-Y. Chen. Dependence of relativistic self-guiding and Raman forward scattering on duration and chirp of an intense laser pulse propagating in a plasma. In M. Lontano, G. Mourou, O. Svelto, and T. Tajima, editors, *Superstrong fields in plasmas: Second Int'l. Conf.*, volume 611, pages 185–190, New York, USA, 2002. American Institute of Physics.
120. T.-W. Yau, C.-J. Hsu, H.-H. Chu, Y.-H. Chen, C.-H. Lee, J. Wang, and S.-Y. Chen. Dependence of relativistic self-guiding and Raman forward scattering on duration and chirp of an intense laser pulse propagating in a plasma. *Phys. Plasmas*, 9:391–394, 2002.
121. R. A. Cairns, D. Johnson, and R. Bingham. Laser wakefield and beat-wave generation by multiple and chirped laser pulses. *Laser Part. Beams*, 13:451–458, 1995.
122. D. A. Johnson, R. A. Cairns, R. Bingham, and U. de Angelis. Plasma wakefield generation by multiple short pulses. *Phys. Scripta*, T52:77–81, 1994.
123. J. M. Dawson. Plasma particle accelerators. *Sci. Amer.*, pages 34–41, March 1989.
124. C. H. Keitel. Ultra-energetic electron ejection in relativistic atom-laser field interaction. *J. Phys. B*, 29:L873–L880, 1996.
125. C. I. Moore, A. Ting, S. J. McNaught, J. Qiu, H. R. Burris, and P. Sprangle. A laser-accelerator injector based on laser ionization and ponderomotive acceleration of electrons. *Phys. Rev. Lett.*, 82:1688–1691, 1999.
126. C. I. Moore, J. P. Knauer, and D. D. Meyerhofer. Observation of the transition from Thomson to Compton scattering in multiphoton interactions with low-energy electrons. *Phys. Rev. Lett.*, 74:2439–2442, 1995.
127. G. D. Tsakiris, C. Gahn, and V. K. Tripathi. Laser induced electron acceleration in the presence of static electric and magnetic fields in a plasma. *Phys. Plasmas*, 7:3017–3030, 2000.
128. S. Y. Chen, M. Krishnan, A. Maksimchuk, R. Wagner, and D. Umstadter. Detailed dynamics of electron beams self-trapped and accelerated in a self-modulated laser wakefield. *Phys. Plasmas*, 6(12):4739–4749, 1999.
129. R. Wagner, S.-Y. Chen, A. Maksimchuk, and D. Umstadter. Electron acceleration by a laser wakefield in a relativistically self-guided channel. *Phys. Rev. Lett.*, 78:3125–3128, 1997.
130. C. Gahn, G. D. Tsakiris, K. J. Witte, P. Thirolf, and D. Habs. A novel 45-

channel electron spectrometer for high intensity laser-plasma interaction studies. *Rev. Sci. Instrum.*, 71:1642–1645, 2000.
131. N. M. Naumova, J. Koga, K. Nakajima, T. Tajima, T. Zh. Esirkepov, S. V. Bulanov, and F. Pegoraro. Polarization, hosing and long time evolution of relativistic laser pulses. *Phys. Plasmas*, 8:4149–4155, 2001.
132. F. Verluise, V. Laude, Z. Cheng, C. Spielmann, and P. Tournois. Amplitude and phase control of ultrashort pulses by use of an acousto-optic programmable dispersive filter: Pulse compression and shaping. *Opt. Lett.*, 25:575–577, 2000.
133. P. Sprangle, J. R. Peñano, B. Hafizi, R. F. Hubbard, A. Ting, D. F. Gordon, A. Zigler, and Jr. T. M. Antonsen. GeV acceleration in tapered plasma channels. *Phys. Plasmas*, 9:2364–2370, 2002.
134. K. W. D. Ledingham and P. A. Norreys. Nuclear physics merely using a light source. *Contemp. Phys.*, 40:367–383, 1999.
135. K. W. D. Ledingham, I. Spencer, T. McCanny, R. P. Singhal, M. I. K. Santala, E. Clark, I. Watts, F. N. Beg, M. Zepf, K. Krushelnick, M. Tatarakis, A. E. Dangor, P. A. Norreys, R. Allott, D. Neely, R. J. Clark, A. C. Machacek, J. S. Wark, A. J. Cresswell, D. C. W. Sanderson, and J. Magill. Photonuclear physics when a multiterawatt laser pulse interacts with solid targets. *Phys. Rev. Lett.*, 84:899–902, 2000.
136. D. Umstadter. Laser light splits atom. *Nature*, 404:239, 2000.
137. I. Spencer, K. W. D. Ledingham, R. P. Singhal, T. McCanny, P. McKenna, E. L. Clark, K. Krushelnick, M. Zepf, F. N. Beg, M. Tatarakis, A. E. Dangor, P. A. Norreys, R. J. Clarke, R. M. Allott, and I. N. Ross. Laser generation of proton beams for the production of short-lived positron emitting radioisotopes. *Nucl. Instrum. Methods B*, 183:449–458, 2001.
138. K. W. D. Ledingham, R. P. Singhal, P. McKenna, and I. Spencer. Laser-induced nuclear physics and applications. *Europhys. News*, 33:120–124, 2002.
139. A. Maksimchuk, S. Gu, K. Flippo, and D. Umstadter. Forward ion acceleration in thin films driven by a high-intensity laser. *Phys. Rev. Lett.*, 84:4108–4111, 2000.
140. R. A. Snavely, M. H. Key, S. P. Hatchett, T. E. Cowan, M. Roth, T. W. Phillips, M. A. Stoyer, E. A. Henry, T. C. Sangster, M. S. Singh, S. C. Wilks, A. MacKinnon, A. Offenberger, D. M. Pennington, K. Yasuike, A. B. Langdon, B. F. Lasinski, J. Johnson, M. D. Perry, and E. M. Campbell. Intense high energy proton beams from petawatt laser irradiation of solids. *Phys. Rev. Lett.*, 85:2945–2948, 2000.
141. M. Zepf, E. L. Clark, K. Krushelnick, F. N. Beg, C. Escoda, A. E. Dangor, M. I. K. Santala, M. Tatarakis, I. F. Watts, P. A. Norreys, R. J. Clarke, J. R. Davies, M. A. Sinclair, R. D. Edwards, T. J. Goldsack, I. Spencer, and K. W. D. Ledingham. Fast particle generation and energy transport in laser-solid interactions. *Phys. Plasmas*, 8:2323–2330, 2001.
142. D. Habs, G. Pretzler, A. Pukhov, and J. Meyer-Ter-Vehn. Laser acceleration of electrons and ions and intense secondary particle generation. *Progress in particle and nuclear physics*, 46:375–377, 2001.
143. V. S. Khoroshkov and E. I. Minakova. Proton beams in radiotherapy. *Eur. J. Phys.*, 19:523–536, 1998.
144. U. Amaldi. Cancer therapy with particle accelerators. *Nucl. Phys.*, A654: 375c–399c, 1999.
145. G. Mourou and D. Umstadter. Extreme light. *Sci. Am.*, 5:63–68, 2002.
146. L. Disdier, J.-P. Garçonnet, G. Malka, and J.-L. Miquel. Fast neutron emission from a high-energy ion beam produced by a high-intensity subpicosecond laser pulse. *Phys. Rev. Lett.*, 82:1454–1457, 1999.
147. G. Grillon, Ph. Balcou, J.-P. Chambaret, D. Hulin, J. Martino, S. Moustaizis, L. Notebaert, M. Pittman, Th. Pussieux, A. Rousse, J.-Ph. Rousseau, S. Sebban, O. Sublemontier, and M. Schmidt. Deuterium-deuterium fusion dynamics in low-density molecular-cluster jets irradiated by intense ultrafast laser pulses. *Phys. Rev. Lett.*, 89:065005, 2002.

148. M. Tabak, J. Hammer, M. E. Glinsky, W. L. Kruer, S. C. Wilks, J. Woodworth, E. M. Campbell, M. D. Perry, and R. J. Mason. Ignition and high gain with ultrapowerful lasers. *Phys. Plasmas*, 1:1626–1634, 1994.
149. C. Gahn, G. D. Tsakiris, G. Pretzler, K. J. Witte, C. Delfin, C.-G. Wahlström, and D. Habs. Generating positrons with femtosecond-laser pulses. *Appl. Phys. Lett.*, 77:2662–2664, 2000.
150. C. Gahn, G. D. Tsakiris, G. Pretzler, K. J. Witte, P. Thiroff, D. Habs, C. Delfin, and C.-G. Wahlström. Generation of MeV electrons and positrons with femtosecond pulses from a table-top laser system. *Physics of plasmas*, 9, 2002.
151. D. K. Cheng. *Field and Wave Electromagnetics*. Addison-Wesley, New York, 2nd edition, 1989.
152. D. Bauer, P. Mulser, and W.-H. Steeb. Relativistic ponderomotive force, uphill acceleration, and transition to chaos. *Phys. Rev. Lett.*, 75:4622–4625, 1995.
153. P. Mora and Jr. T. M. Antonsen. Kinetic modeling of intense, short laser pulses propagating in tenuous plasmas. *Phys. Plasmas*, 4:217–229, 1997.
154. B. Quesnel and P. Mora. Theory and simulation of the interaction of ultraintense laser pulses with electrons in vacuum. *Phys. Rev. E*, 58: 3719–3732, 1998.

Part II